EFFECT OF CYCLIC HIGH LOADING RATES ON THE FATIGUE STRENGTH OF ALUMINUM-BASED COMPOSITES

By

Hermes Eskander Calderón Arteaga

Dissertation submitted in partial fulfillment of the requirements for the degree of

DOCTOR OF PHILOSOPHY
in
CIVIL ENGINEERING

UNIVERSITY OF PUERTO RICO
MAYAGÜEZ CAMPUS
2009

Approved by:

O. Marcelo Suárez, Ph.D. President, Graduate Committee	Date
Luis A. Godoy, Ph.D. Member, Graduate Committee	Date
Ricardo R. López, Ph.D. Member, Graduate Committee	Date
Luis E. Suárez, Ph.D. Member, Graduate Committee	Date
Basir Shafiq, Ph.D. Member, Graduate Committee	Date
Carlos U. Pabón, Ph.D. Representative of Graduate Studies	Date
Ismael Pagán Trinidad, Prof. Chairperson of the Department	Date

Abstract

The study of fatigue under high loading rates is of great interest in the complete characterization of a new series of composites with Al-Cu-Mg matrix reinforced with AlB_2 dispersoids. Homogeneous and functionally graded composites were prepared via gravity and centrifugal casting, respectively. Through centrifugal casting a gradual variation of the volume fraction of reinforcing particles along the cross section was obtained. In specific fabrication conditions, even complete segregation of the reinforcement particles was achieved. Charpy impact tests as well as hardness tests were conducted to assess the composite strength as a function of the weight percent of boron. The tensile properties of gravity cast samples were obtained. Then for both casting conditions, simple edge-notched bend SE(B) specimens were tested under fatigue conditions (three-point bending). The results from impact and hardness tests allowed identifying an interaction between the Mg dissolved in the matrix and the diborides. This interaction, which has never been reported before, was responsible for the strength reduction observed. It was assumed that a substitutional diffusion of Al by Mg atoms in the hp3 structure of diboride was causing the strength reduction, and three approaches were developed to estimate the amount of Mg depleted from the matrix by the diborides during the composite processing. Gravity cast samples were more sensitive to monotonic damage due to fatigue loads where compared with functionally-graded composites. Contrary to the centrifugal cast samples, gravity samples were also affected by the loading rate. The Mg-AlB_2 interaction was also responsible for the reduction in the fatigue resistance as the weight percent of boron increased in both types of composites; regression models were obtained to predict the crack growth curve slope change as function of the boron level. The particle distribution showed to affect the crack growth behavior of the FGMs, decreasing the fatigue resistance when the crack tip traveled through higher particle density zones. The fracture surface of these composites exhibited quasi-cleavage and the roughness was associated with the microstructure phases. Finally, the effect of the Mg-AlB_2 interaction could be corrected if it is taken into account in the mass balance prior to the casting process.

Resumen

El estudio de la fatiga cuando las cargas son aplicadas a alta velocidad es de gran interés en la caracterización completa de una nueva serie de compuestos con matriz Al-Cu-Mg reforzada con AlB_2. Compuestos con distribución homogénea de partículas y de gradiente funcional fueron fabricados mediante fundición normal y fundición centrífuga, respectivamente. Usando fundición centrífuga se obtuvo una variación gradual de la fracción volumétrica de partículas a lo largo de la sección transversal de la muestra. Bajo condiciones particulares, también se obtuvo una completa segregación de las partículas de refuerzo. Pruebas de impacto tipo Charpy, así como pruebas de dureza, fueron realizadas para determinar la resistencia de los compuestos en función del porcentaje en peso de boro (*wt.% B*). Se obtuvieron las propiedades en tensión de muestras obtenidas por fundición normal. Ambos tipos de fundición fueron ensayados en fatiga. En ambos casos se prepararon especímenes de flexión con muesca central SE(B). Los resultados de las pruebas de impacto y dureza permitieron identificar una interacción entre el Mg disuelto en la matriz y las partículas de refuerzo. Esta interacción, nunca reportada antes, fue responsable de la caída en resistencia observada en dichas pruebas. Se asumió que la difusión sustitucional de átomos de Al por átomos de Mg en la estructura hp3 de los diboruros causó dicha caída en resistencia; tres métodos se desarrollaron para estimar la cantidad de Mg tomada por las partículas de la matriz durante la fabricación del compuesto. Las muestras obtenidas por fundición normal fueron más sensibles a daño monotónico que los compuestos obtenidos por centrifugado, a las cargas de fatiga ensayadas. Contrario a los resultados observados en muestras obtenidas por centrifugado, las muestras obtenidas por fundición normal también fueron afectadas por la velocidad de carga. La interacción Mg-AlB_2 también fue responsable de la reducción en la resistencia a fatiga cuando se aumentó el *wt.% B* en ambos tipos de compuestos. Modelos de regresión fueron ajustados para predecir el cambio en la pendiente de la curva da/dN vs ΔK^* en función del *wt.% B*. La distribución de partículas afectó el crecimiento de grieta en compuestos de gradiente funcional, disminuyendo la resistencia a fatiga cuando la grieta atravesó las zonas con mayor densidad de partículas. La superficie de fractura exhibió una mezcla entre regiones de fractura frágil y dúctil, mientras la rugosidad fue asociada a las fases presentes en la microestructura. Para concluir, el efecto de la interacción Mg-AlB_2 podría ser corregido si tal interacción es tomada en cuenta en el balance de masa, antes del proceso de fundición.

To my parents and wife

Acknowledgments

In first place, I want to thank my parents, Hermes and Alicia, and my wife, Diana, by their continuous support; they have given me the tools for my continuous professional growth. This acknowledgement is also extended to the University of Puerto Rico, institution that has given me the opportunity to achieve my graduate degree. In this order, it is also important to recognize the role of the Civil Engineering and Surveying Department as well as the Department of Engineering Science and Materials, Departments that have welcomed me during my stay.

I want to express a special thanks to my advisor, Dr. O. Marcelo Suárez for his guidance during the development of this dissertation, for offering me his friendship and support. Also, it is important to recognize the collaboration of Dr. Basir Shafiq for kindly permitting to use the hydraulic testing equipment.

I would like to thank my partners: Humberto Melgarejo for his help with the EDS studies, Samuel Charca for his cooperation with the fatigue test equipment, Lilia Olaya and Boris Rentería for their collaboration in the use of X-Ray Diffractometer; I also want to express my gratitude to Alexis Torres, Victor Estrella, Maxuel Cruz, Giovanni Sandoval, Edwin Olán, Carlos Cosme and Carla Príncipe, all UPRM undergraduate students that in some way collaborated with this project.

I want to also thank to my friends Norberto, John Jairo, Ruth, Glorimar, Orlando, Tunde and Carlos as well as the gentlemen Luis Macias and José Luis Ruano by their motivation and support.

The Al-B master alloys were kindly donated by KB alloys Inc. Robesonia, PA, USA. This material is based upon work supported by the National Science Foundation under grants Nº DMR 0351449 (PREM Program) and HRD 0833112 (CREST Program). Additional funding for instrumentation was provided by the US Department of Defense under grant award W911NF-07-1-0611 (HBCU/MI ISP program). Support was also received from the ONR and AGEP programs.

Table of Contents

Table List

Figure List

1 INTRODUCTION

The development of metal matrix composites (MMCs) has been one of the major innovations in the past 25 years. In automotive, aerospace and other industries that require lightweight structures, aluminum matrix composites (AMCs) are used as structural elements [1]. In some applications these structures are submitted to cyclic loads and if a sufficiently high number of stress cycles are applied to a given component, even at small stress levels, it will fracture as a result of fatigue. When the loads are applied at high rates, a similar situation exists. If the minimum energy required to fracture a part, with a single impact, can be established (critical case of high loading rate), a load cycle at a lower energy level will not cause failure; however, a sufficient number of load cycles at the lower level will cause it to fracture. This phenomenon should be considered when materials are selected for engineering applications. Despite its importance, fatigue under high loading rates has not been analyzed intensively in aluminum matrix composites. Therefore, the study of this phenomenon is of great interest in the full characterization of a new series of AMCs.

1.1 Literature review

Aluminum composites containing a maximum of 5 wt.% Cu in the matrix and reinforced with ceramic particles of aluminum diboride (AlB_2) were studied by Suárez in 2001 [2]. He found that the hardness of these composites can be adjusted by aging treatments. In addition, the effect of AlB_2 particles, on the aging time, was also analyzed by this author, who concluded that the particles reduced the aging time necessary to obtain the overall maximum hardness peak [3]. In 2004 Calderón confirmed the feasibility of using a combination of heat treatments and cold work to adjust the hardness of the composites [4]. He also performed tensile tests to determine that the yield strength increased with the volume fraction of reinforcement. In addition the author studied the composite fracture morphology, identifying a mixture of ductile and brittle fractures of those composites. In 2006, Melgarejo studied the wear resistance of functionally graded composites containing magnesium instead of copper in the matrix [5]. In this case the samples were obtained by centrifugal casting and the distribution of particles due to the centrifugal acceleration was also studied. It was proven that the wear resistance also increased with the particle volume fraction.

Moreover, an increasing number of MMCs reinforced with ceramic particles are used in applications where the structures are subject to fatigue (one of the main causes of failure). In the past, some disasters in engineering such as the Versailles train crash (1842), De Havilland Comet (1954), the Liberty Ships during World War II and the Eschede train disaster (1998) were attributed to fatigue failures. The first study on the fatigue phenomenon was published in 1837 by Wilhelm Albert. A few years later, Poncelet described “tiring” on metals in 1839 [6]. In 1842 the importance of stress concentrations was recognized by William J. Macquorn Rankine [7]. Joseph Glynn identified the keyway as the crack origin. In 1870 Wöhler introduced the concept of endurance limit. By 1903 James Alfred Ewing related the origin of fatigue failure with microscopic cracks. In 1954 Coffin and Manson explained fatigue crack-growth in terms of plastic strain at the crack tip and Paris in 1961 developed relationships for crack growth in terms of the stress intensity factor K [6].

Another way to describe the material behavior during cyclic loading is the hysteresis loop, which allows the quantification of the plastic strain per cycle. Such plastic deformation is affected by the presence of dislocations, which are involved in the mechanism of fatigue damage initiation and accumulation [8]. The theory of fracture mechanics states that the phenomenon can be divided in four stages: crack nucleation, crack growth stage I, crack propagation stage II, and ultimate ductile failure [9]. In particular, homogeneous materials manifest differences in the number of cycles to failure for a given level of stress. For this reason, a probabilistic analysis is commonly used to define the fatigue life of a material. This is represented as a plot of stress (S) vs the number of cycles to failure (N), known as the S-N curve.

In real applications, structural components are exposed to a range of complex fatigue loads, which can be described as an often random sequence of loads, both large and small. This is commonly represented during testing studies by a series of simple cyclic loads to facilitate the calculation of cumulative damage for each stress level [10].

Another kind of load frequently reported to cause fatigue failure is repeated impact loading. The impact fatigue loads can be divided into two types: periodically applied impact load and randomly repeated impact load. Studies on metallic materials reveal that the impact fatigue strength is lower than the non-impact fatigue strength [11, 12]. The critical case of high loading rate is the impact load, which produces elastic and plastic strains in the specimen [13]. At a certain stress level, a crack can grow even if the initial dimension is smaller than a critical crack size. The crack growth can allow a plastic state near the crack tip [14]. This plastic state at the crack tip can result in one of three conditions: a) small scale yielding, b) elastic-plastic condition, and c) large scale yielding. These criteria are useful in damage tolerant design to estimate the acceptable initial defect size [15, 16].

One relevant work found in the literature is that of Tanaka et al. in 1985 [12], who studied the propagation behavior of cracks under impact fatigue load on high-strength HT-60 low alloy steel. They found no significant difference on the crack growth rates under impact and non-impact loads. Nevertheless, for other materials studied previously by those authors, it was observed that the crack growth rate with impact fatigue was in most cases higher than with non-impact fatigue.

Yu et al. in 1999 is a literature review on the impact fatigue of metallic materials [11]. They indicated that such phenomenon on metallic materials remains less investigated. This is mainly due to experimental difficulties and the complexity of impact fatigue test results. Nevertheless, they found that the crack tip plastic deformation zone in impact fatigue is smaller than for non-impact fatigue at the same K_{max} level. With impact fatigue fracture strength the results are usually expressed by impact energy (A) and impact fatigue life (N_f) curve (A-N_f curve), or with impact maximum stress (S) and impact fatigue life curve (S-N_f curve), and by the strain range ($\Delta\varepsilon_p$) versus cycle life (N_f) curve. Stress concentration causes the impact fatigue life of materials to decrease significantly. Moreover, the impact fatigue crack initiation life was related to fatigue crack initiation mechanisms and impact fatigue crack propagation followed the

Paris law. The area fractions of brittle fracture are larger than in non-impact fatigue. Finally, they concluded that more attention should be paid by scientists in the research field regarding the impact fatigue of materials.

The impact fatigue phenomenon has also been studied in polymer matrix composites. For example, Sinmazçelik et al. in 2006 worked on unidirectional fiber reinforced polymer composites over 10^4 impact cycles [17]. They identified debonding, fiber breakage and pull-out on the fracture surface of the composites [17-19]. Cohen and Yalvac studied the role of a particulate reinforcement on the impact tolerance of thermoplastic materials [20]. They pointed out the possibility of improving damage tolerance through the introduction of particle reinforcement.

Yang and Liu worked in impact fatigue of SiC_w/7475 aluminum matrix composites [21]. They found that in low cycle impact fatigue the cracks often initiated within or near SiC particles. Hancock and Shaw studied the effects of plastic interface zone on axial fatigue resistance and on the Charpy impact behavior of 6061 aluminum composites reinforced with boron fibers [22]. They concluded that a plastic and soft interface zone will only be effective in improving fatigue resistance in composites with a high strength metal matrix having poor toughness.

Other interesting results were obtained by Sebbanie and Allaire in 2001 [23]. They presented a new theoretical approach for the impact fatigue damage of refractories. Their results of impact testing were linked especially to a new parameter ($\sigma_o^2/E\gamma$), where σ_o is the modulus of rupture; E is Young's modulus; and γ, the surface energy. Therefore, increasing the modulus of rupture or decreasing both the Young's modulus and work of fracture will result in an increase of the impact fatigue resistance.

Although there are several studies of the fatigue phenomena under impact loads, the effect of high loading rates with loading times higher than 1 ms on the fatigue of particle reinforced aluminum matrix composites have not been extensively studied.

Furthermore, fracture surface analysis is the common practice to understand the mechanisms of the fatigue process. Scanning Electron Microscopy (SEM) is a tool extensively used to study the fracture surface morphology in materials, because it offers information about striation widths and detailed images of different fracture patterns [24]. However, optical microscope techniques are complementary to perform the complete fracture surface analysis.

1.2 Objectives

Characterize and model the fatigue lifetime behavior of aluminum matrix composites (AMCs) subject to cyclic high loading rates. The composites are constituted by a matrix containing 2.5wt.% Cu and 1wt.% Mg and reinforced with different amounts of AlB_2 particles. Additionally, the response of the composites as a functionally graded material is analyzed.

Since these composites are not commercially available, the development of a methodology for the material fabrication and some mechanical tests are a fundamental part of the specific objectives, which are listed below:

- Fabricate samples for impact tests and flexural tests via gravity casting.
- Establish a procedure to fabricate and produce samples for flexural tests of functionally graded composites using centrifugal casting.
- Carry out microstructural analysis to identify the phases in the matrix and study the particle distribution.
- Perform impact tests and determine the effect of particle concentration on the fracture absorbed energy of the composites.
- Develop flexural tests to establish the load capacity and flexural properties under monotonic loading of bending specimens obtained by gravity casting and centrifugal casting.
- Design and carry out load control fatigue tests to study the lifetime of aluminum based composites under high loading rates.
- Study the fracture surface via SEM to reveal the microstructural details associated to the life time of the material.

- Obtain a semi empirical model to predict the fatigue lifetime for this type of composites, as a function of the weight percentage of Boron and of the loading rate.

2 THEORETICAL BACKGROUND

2.1 Al-Cu-Mg-B Composite System

The composite is fabricated with three master alloys (Al-Cu, Al-Mg and Al-B) to obtain an Al-Cu-Mg matrix with aluminum diboride as the dispersed phase. At melting temperatures under 900ºC Al, containing Cu and Mg in solution (phase), melts forming a liquid solution while the borides remain solid [4].

With small amounts of Cu and Mg (2.5 and 1 wt. % respectively), after solidification the matrix composites fall in the aluminum rich corner of a ternary phase diagram. The matrix is then constituted by an Al α-phase with Cu and Mg in solid solution, with some binary phases of Al-Cu, which can form during solidification and which will be detailed in the next sections.

Boron in the Al-B master alloy appears forming boride particles, which reminds solid during the fabrication process. The borides can be AlB_2 or AlB_{12} and the selection of the commercial master alloy depends on the type of boride necessary in the composite design.

2.1.1 Al-Cu System

One of the most important alloying elements for aluminum is copper, which produces considerable hardening by solid solution, and allows strengthening by precipitation hardening (aging treatment) at levels lower than the maximum solubility in Al (5.65 wt.%Cu). Since the level of copper in the composites treated in this work is 2.5 wt.%Cu (red line in the phase diagram of Fig. 2.1), the material could be hardened by precipitation. This process has been studied before in similar composite systems [4].

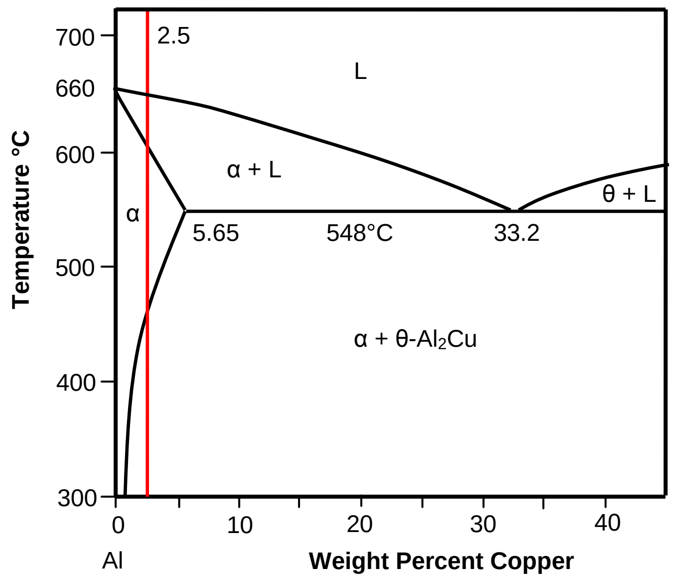

Fig. 2.1 Aluminum-cooper phase diagram

After cooling, the aluminum solid solution or α-phase containing copper start precipitating Cu as the stable phase θ or Al_2Cu. This phase is known to precipitate in the α-Al grain boundaries, as shown in Fig. 2.2. It is incoherent with the matrix and has a body center tetragonal (BCT) structure with cell parameters c=4.87 Å and a=6.06 Å [25].

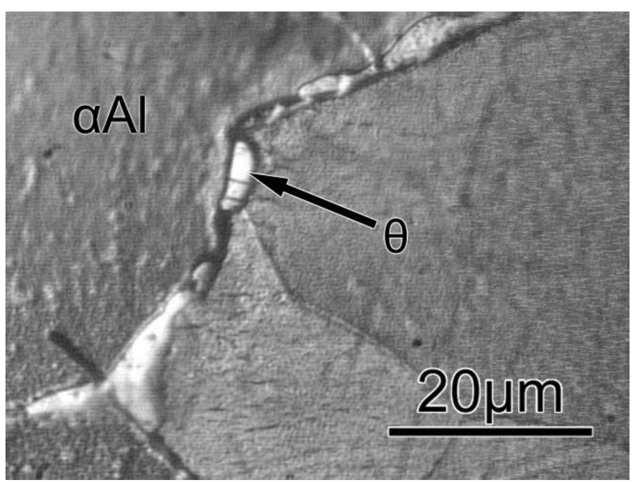

Fig. 2.2 Precipitation of incoherent phase θ in an Al-5wt.% Cu matrix

2.1.2 Al-Mg System

Magnesium is an important alloying element, particularly used in high strength aluminum alloys like AA6061 and AA7075 (employed in aerospace applications). Mg improves the strength of aluminum alloys and reduces their density linearly, around 0.5% by each 1 wt.%Mg [26]. In aluminum alloys with Mg concentration below 5%, substitutional Mg solute appears randomly distributed in the α-Al solid solution matrix. However, at room temperature, for higher concentrations, Mg tends to precipitate forming an intermetallic compound, Al_3Mg_2, but the kinetics of the phase formation is very slow.

In aluminum alloys with Mg over 7%, the precipitation of the phase Al_3Mg_2 is evident and the material could be heat treated by aging. However, the precipitation of the soft intermetallic phase does not affect the mechanical properties and strengthening is only reached by plastic deformation.

The red line in Fig. 2.3 indicates the Mg proportion (1 wt.%) in the composites studied in this work. At low temperatures, aluminum alloys with such proportion of Mg do not show precipitates of Al_3Mg_2.

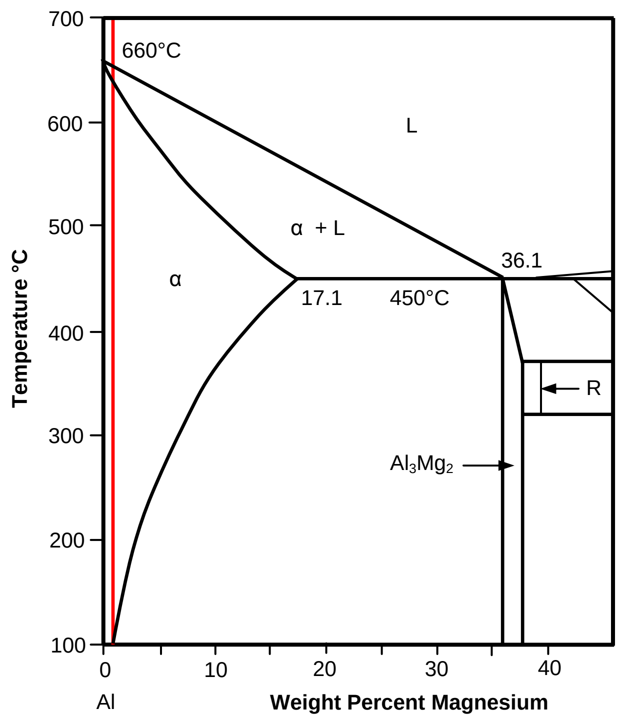

Fig. 2.3 Aluminum-magnesium phase diagram

2.1.3 Al-B System

Aluminum diboride (AlB_2) is a hard phase with a hexagonal crystal structure (Fig. 2.4). For weight percents of Boron less than 40%, at the Aluminum melting temperature (660°C), the AlB_2 phase remains solid. It only transforms into AlB_{12} at 972°C. The AlB_{12} is another hard phase with a complex tetragonal crystal structure. In some Al-B alloys this phase can also be observed at low temperatures.

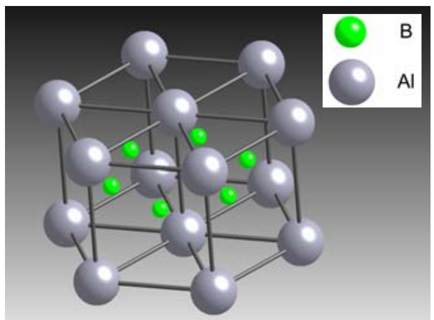

Fig. 2.4 AlB_2 crystal structure

The red area in Fig. 2.5 denotes the boron range studied in this work. These amounts of Boron permit the formation of AlB_2 particles in the master alloy selected. The particle has an average size around 20 µm of diameter [4].

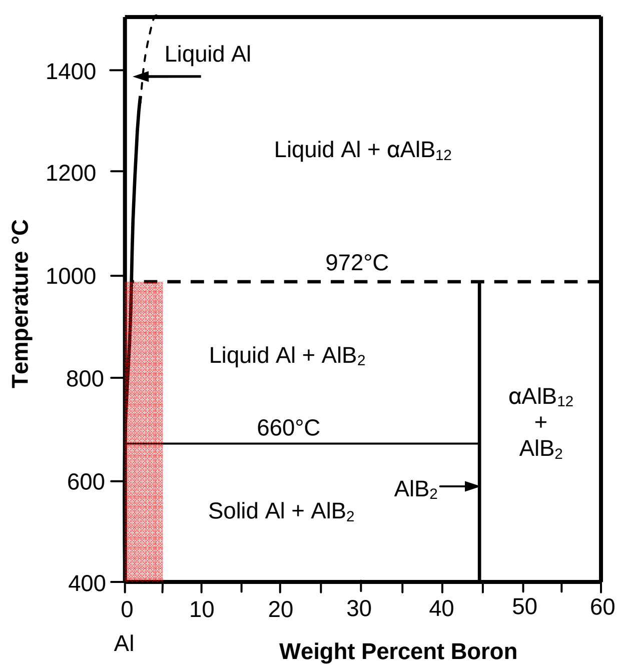

Fig. 2.5 Aluminum-boron phase diagram

2.2 Functionally Graded Materials (FGMs)

These materials are advanced multifunctional composites where the reinforcement volume fraction varies smoothly. The microstructural variation causes changes in the thermal and mechanical properties of the composite [5, 27]. For the fabrication of FGMs various processes such as centrifugal casting, chemical vapor deposition, plasma spray technique and some powder metallurgy techniques have been utilized.

2.2.1 Centrifugal Casting

This casting process can be employed to fabricate FGMs by casting the semiliquid composite and applying a centrifugal acceleration on the material. Then, a compositional gradient is obtained due to the density difference between the dispersoids and the molten metal. This technique permits the production of relatively large components at low fabrication costs.

This centrifugal casting method can be classified in two categories according to the melting point of the dispersoids. The solid particle technique is used when the melting point is higher than the process temperature, while the *in-situ* technique is employed when the melting point of the dispersoids phase is lower than the process temperature. In the last case the solidification is similar to the productions of *in-situ* composites using the crystallization phenomena. Nevertheless, the particle distribution phenomena in FGMs, fabricated using centrifugal casting, have not been completely explained. Several variables affect the process and complicate the whole analysis: dispersoid/molten metal density ratio, the solidification rate and the centrifugal acceleration and viscosity changes during the cooling process.

Once the type of dispersoids has been selected, the density ratio is a constant and the other two variables are controlled by adjusting different parameters. The centrifugal acceleration can be set by adjusting the rotational speed and radius of the mold containing the semiliquid composite. The solidification rate can be controlled by adjusting: pouring, scoop and mold temperatures, as well as the thermal gradient across the mold. The thermal gradient also depends on the mold shape and its thermal conductivity. Each one of these parameters can affect several phenomena during the solidification of the semiliquid composites with solid dispersoids; for instance: the interaction between the solidification front and dispersoid, variation rate of melt viscosity, interaction liquid/dispersoid and maximum displacement of the solid particle.

Some theoretical models have been developed to estimate the apparent viscosity of the semisolid material, as well as the position of a particle as a function of the time and rotational speed. Nevertheless, there are limitations due to the number of variables involved in the centrifugal casting process. Fig. 2.6 illustrates the centrifugal process setup schematically.

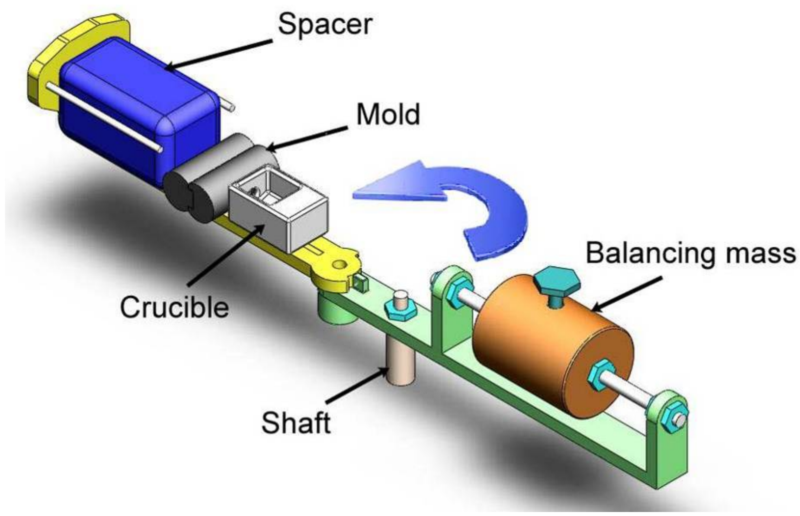

Fig. 2.6 Schematic illustration of the centrifugal casting device

2.3 Impact Testing

The Charpy and Izod tests are typical impact tests for metallic materials and based on a pendulum hammer swinging around a hub. The hammer impacts on a simple supported notch sample, while in an Izod test an end of the notch sample is fixed, as shown in Fig. 2.7. Some systems can record load, time and deformation for the entire period of the test by using electronic sensing instrumentation.

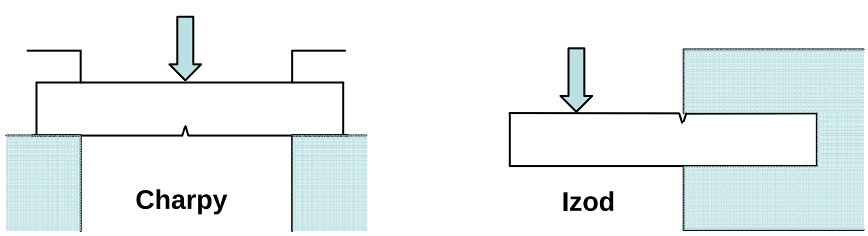

Fig. 2.7 Schematic representations of Pendulum Standardized tests

2.3.1 Charpy Impact test

This high strain-rate test permits the determination of the amount of energy absorbed by a material fractured by an impact load. This fracture energy is a measure of the material toughness and is used for comparison purposes [28]. Normally, this comparative test is used to study the effect of temperature on the fracture energy of metals [29]. The ASTM E23 standard provides the required dimensions of the specimens [29].

2.4 Fatigue of Particle Reinforced Al-Based Composites

Fatigue resistance is an important design criterion in these materials. The study of this phenomenon has been focused to the effect of heterogeneities on the crack initiation and crack growth stages. Therefore, the strengthening mechanism, of particle reinforced materials, is briefly discussed in this section. The strengthening in AMCs may be direct and/or indirect. Direct strengthening is meant when there is load transfer from the matrix to the reinforcement and indirect, due to the influence of the reinforcement on matrix microstructure or deformation mode. For example, the thermal mismatch between the reinforcement and the matrix induce tensile strains near the particles, which is accommodated by an increased dislocation density. Such inhomogeneous dislocation distribution affects the plastic flow, yield strength and work hardening, which indirectly strengthen the material [30]. In some composites, such dislocations serve as nucleating sites for precipitate formation. During aging the increment in dislocation density accelerates the aging in the matrix, which directly influences the fatigue life of the component. [31].

Various models have been developed to predict the variation in the yield strength by an increase of the volume fraction of particles; however there are limitations in the number of factors that are taken into account. Some of those models are:

$$\sigma_{cy} = \sigma_{my}\left(\frac{V_p\left(S+4\right)}{4} + V_m\right) \qquad \text{Direct strengthening model} \qquad \textbf{(2-1)}$$

$$\Delta\sigma = \alpha \cdot \mu \cdot b \cdot \rho^{1/2} \qquad \text{Indirect strengthening model} \qquad \textbf{(2-2)}$$

and, $$\rho = \frac{BV_p(\alpha_p - \alpha_m)\Delta T}{b(1-V_p)} \cdot \frac{S}{D} \qquad \textbf{(2-3)}$$

where, σ_{cy} and σ_{my} are the composite yield strength and matrix yield strength respectively, α is a geometric constant, α_p and α_m thermal expansion coefficient of particles and matrix respectively, $\Delta\sigma$ is the yield strength variation, V_p and V_m are the volume fraction of particles and matrix respectively, ΔT is the temperature variation, *b* is the magnitude of the Burger's vector, *S* is the particles aspect ratio, *D* is the particles diameter and *B* is a geometric constant [30].

In general, these models do not describe completely the strengthening scenario. The first does not take into consideration the size of reinforcing particles; while, the second assumes rectangular particles. In reality, the particle effect in fatigue is more complex. Other models have been proposed to explain the crack initiation and propagation processes in the presence of precipitates and large inclusions.

In Fig. 2.8(a), micro-inclusions are found between the crack tip and a large inclusion. Initially a void nucleates from the large inclusion and grows accompanied by plastic deformation. Right before the crack extension, micro-voids nucleate and coalesce under mechanical interaction between the crack and the large void. High strength aluminum alloys seem to correspond to this model. In the second, Fig. 2.8(b) model a micro-void nucleates from a micro-inclusion (precipitate) ahead of the crack tip and grows and coalesces with the crack. This model also can correspond to a high strength aluminum alloy [32].

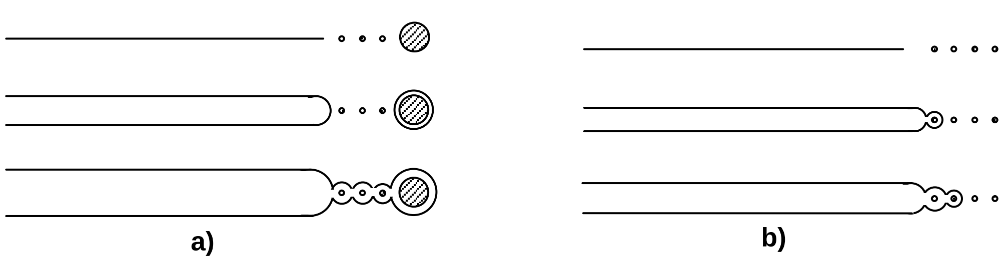

Fig. 2.8 Models of crack initiation and propagation processes

Similar models represent the deformation behavior at the particle interface subject to a stress field. When the applied stress is higher than the maximum stress capacity of the particle/matrix interface, separation occurs between the two phases. It can be represented by the crack path in Fig. 2.9, where the presence of particles, with a given size d and spacing λ, impeding a crack advance, inducing crack roughness. In this case the driving force for a fatigue crack to bypass the particulates occur either by an Orowan mechanism (crack meandering or deflection) or cutting the particles (intersection) is related to the harmonic mean of the size and spacing of the particulates: (1/λ + 1/d). Thus, for λ>>d, the driving force is mostly a function of the size of particulate and for d >> λ, the spacing between particles essentially controls the driving force. To determine the harmonic mean of particle reinforced composites some authors have used the following equation [33]:

$$\lambda = 0.67D\left(\frac{1}{V_p} - 1\right) \qquad \text{Particulate spacing} \qquad \textbf{(2-4)}$$

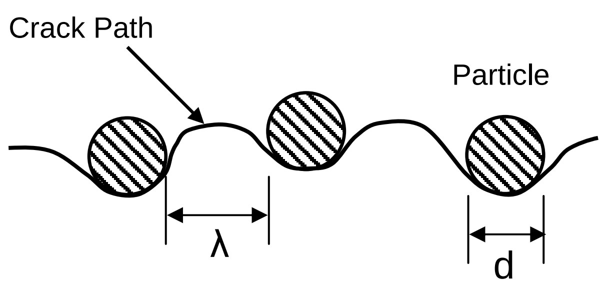

Fig. 2.9 Illustration of particles impeding a crack advance

In addition, Lange, in 1970, developed a model for the fracture energy of a composite material using a similar analysis when the growth of a crack is impeded by particles. In this case, the percentage increment of crack length depends on the spacing between particles. In other words, two energy components are required. The first term, in equation 2.5 is the energy needed to create a new fracture surface and the second is the energy required to increase the crack length.

$$G_{IC} = G_{0m} + \left(\frac{\gamma_r}{\lambda}\right) \qquad \text{Fracture energy} \qquad \textbf{(2-5)}$$

where G_{0m} is the fracture energy of the matrix, γ_r is the crack front interfacial energy by length unit and λ is the particle spacing in equation 2.4 [34].

At a microscopic level, micro-cracking and voids between particles occur due to strain localization in the vicinity of these microstructural features. The stress state at the crack-tip induces plasticity, and results in crack-tip dislocation emission. Dislocations travel into the material away from the crack-tip and when the slip path is blocked by a particle, dislocations pile up behind the particle, increasing the stress at the head of the pile up. When the stress is large enough, particle shearing, particle fracture, cross slipping, or dislocation looping around the particle may occur [16].

In practical terms, a dependence of particle cracking with increasing size has been observed in fatigue [31, 35] and some studies have concluded that increasing volume fraction and decreasing particle size improve fatigue resistance. However, the mechanisms for these improvements remain unclear [31, 36]. In comparison with homogeneous materials, characteristics like porosity, intermetallic inclusions, precipitates and particle reinforcement are potential environments for crack initiation [37]. In addition, fatigue damage-induced degradation has been observed as matrix cracking triggered by microstructural factors, like the presence of large intermetallic phases, reinforcement defects, particle clusters, or large particles with sharp edges surrounded by large reinforcement free areas. This localized damage leads to the initiation and to the extension of short cracks [31].

The presence of the aforementioned microstructural defects can also generate crack growth retardation due to crack deflections. For example, branching and bridging due to particle debonding result in crack deflection and has been attributed to an enhancement of the fatigue resistance of cast aluminum alloys [38, 39].

Most of the defects are introduced during the material processing. For example, in cast aluminum alloys, porosity and inclusions are the defects with most influence on fatigue resistance, porosity being the most detrimental. In addition to porosity, pore distribution, size and morphology of pores are important factors. In particular, when the pore size exceeds a threshold value, the fatigue life of a component is dramatically affected. Since porosity has a dominant effect on the fatigue resistance, the effect of other factors can only be revealed when porosity is controlled. For instance, reducing pore size to about 25 μm in an A356 type alloy, the fatigue strength was similar to pore-free specimens, suggesting that ~25 μm was the critical pore size on this alloy [40]. Although some authors have related the presence of particles with a decrease in fatigue resistance of composite materials [33], in general, the addition of hard ceramic particulate reinforcements to aluminum alloys can result in an increase in fatigue resistance at a reasonable cost [31, 35].

2.5 High Loading Rates

The ASTM standards have defined rapid loading on metallic materials when the loading rate exceeds those for conventional (static) testing (2.75 MPa·m$^{1/2}$/s (150.000 psi·in.$^{1/2}$/min)). and limit the validity of equations for calculation of stress intensity factor to load times longer than one millisecond [41, 42]. In addition for J-integral determination under rapid loading (including drop weight conditions) a minimum test time is also defined and as a function of the stiffness and the mass of the specimen, as shown in equation 2.6 [41].

$$t_w = \frac{2\pi}{\sqrt{k_s / M_{eff}}} \qquad \text{Minimum test time} \qquad \textbf{(2-6)}$$

Where k_s is the specimen load stiffness (N/m) and M_{eff}, the effective mass of the specimen, taken to be half of the specimen mass (kg).

In other words, the test time should be no less than the period of the first natural frequency of the element tested. The natural period is also used to define the impact conditions. In the case of instantaneous loading or impact testing (either Free-falling or swinging masses) the duration usually is shorter than the natural frequency period [43, 44].

2.6 Fatigue Crack Growth (FCG)

In fatigue studies two philosophies are utilized, safe life (or damage intolerant) and damage tolerant, that are used for material selection under certain stress conditions. In the first method fatigue data is presented by using S-N curves, i.e. stress (S) vs number of cycles to failure (N). Typical S-N curves are represented schematically in Fig. 2.10.

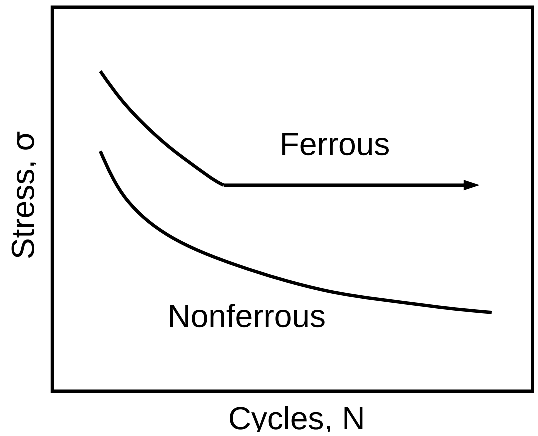

Fig. 2.10 Typical fatigue S-N curves

The second method examines fatigue crack growth rate (da/dN) as a function of stress intensity factor range (ΔK) [40], both of which are experimental parameters. The fatigue crack growth rate (FCGR) is defined as the crack extension per cycle of loading, while $\Delta K = K_{max} - K_{min}$, where K_{max} is the test maximum stress intensity factor (SIF) while K_{min} is the corresponding minimum, which is assumed to be zero if the minimum SIF is negative.

The test is realized by loading cyclically notch and fatigue precracked specimens. Different specimen configurations as well as different test procedures can be employed. Constant force amplitude, K-decreasing and alternative K-control are the recommended test procedures [45]. The results of these tests are commonly represented in a log-log graphic of da/dN vs ΔK where three stages of crack growth are usually defined, as shown in Fig. 2.11.

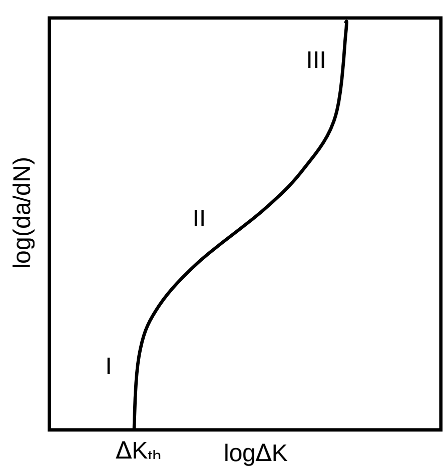

Fig. 2.11 Typical fatigue crack growth curve

The first stage or threshold corresponds to an asymptotic value of ΔK at which da/dN approaches cero or is almost neglected. In other words, this is the maximum value of ΔK that the material supports without crack progress. The standard ASTM E647 establishes an operational value for the fatigue crack growth threshold. Thus, ΔK_{th} is defined as the ΔK value, which corresponds to a fatigue crack growth rate of 10^{-10} m/cycle [45].

Stage II is referred to the linear part of the curve and corresponds to stable crack growth. This stage is also known as the Paris regimen, because P. Paris presented one of the first models to describe the behavior of the materials under stable crack growth or subcritical crack growth. The model of equation 2.7, also known as the Paris law, permits obtaining the FCGR and provides a quantitative prediction of residual life for a crack of a certain size [46, 47].

$$\frac{da}{dN} = C\Delta K^{m} \qquad \text{Paris law} \qquad \textbf{(2-7)}$$

where, *a* is the crack length, *N* is the number of load cycles, *C* and *m* are material constants that are obtained from the fatigue crack growth curve. The residual life could be assessed integrating equation 2.7 for a given fatigue life N_f, knowing the actual and critical crack length as in equation 2.8.

$$\int_{0}^{N_f} dN = \int_{a_i}^{a_f} \frac{da}{C\Delta K^{m}} \qquad \textbf{(2-8)}$$

Finally, stage III in the curve corresponds to high FCGR, also defined as unstable crack growth stage. In this regime the maximum stress intensity accelerates the crack growth adding static modes of fracture (cleavage, intergranular) to the fatigue induced growth rates.

In general, the stress intensity factor range, ΔK, is widely accepted as a crack driving force for a crack growth analysis. However, the effectiveness of ΔK is affected by the load ratio $R = P_{\min} / P_{\max}$. Such effect can be observed in Fig. 2.12, where typical results from constant amplitude loading are presented schematically.

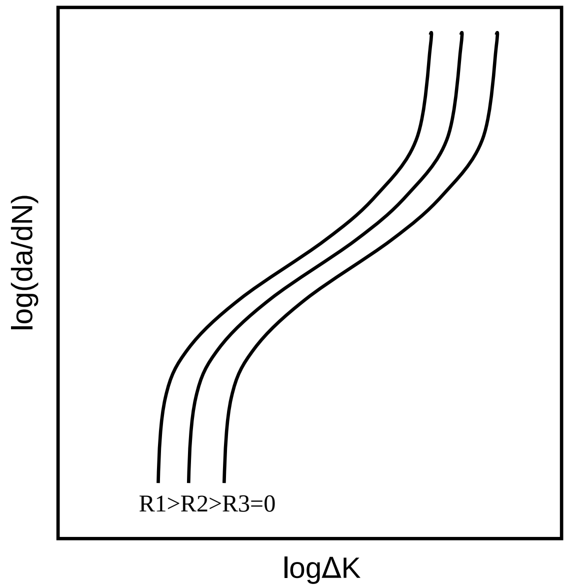

Fig. 2.12 Representation of R-ratio effect on fatigue crack growth

Based on experimental observations, for lower load ratios, during the unloading sequence premature contact between the crack faces occurs while some load is still applied, which affects the fatigue life of the element. This phenomena is know as fatigue crack closure and several concepts have been adopted to account for this R-ratio effect: namely, crack closure, residual compressive stress, environmental influence, the ΔK and K_{max} driving force approach and the partial crack closure model. Most of those concepts result in modifications to the Paris law.

The modified Paris rule includes the concept of effective stress intensity factor ΔK_{eff} instead of ΔK. Elber was the first who introduced the effective stress intensity factor ΔK_{eff} [48]. This concept employs the minimum stress intensity factor necessary to open the crack (K_{op}) if the applied K_{min} is lower than K_{op} [36, 49].

$$\frac{da}{dN} = D\Delta K_{eff}^{n} \qquad \text{Modified Paris law} \qquad \textbf{(2-9)}$$

where:

$$\Delta \mathrm{K}_{\mathrm{eff}} = K_{\max} - K_{\min} \qquad \text{if } K_{\min} > K_{op} \qquad \textbf{(2-10)}$$

$$\Delta \mathrm{K}_{\mathrm{eff}} = K_{\max} - K_{op} \qquad \text{if } K_{\min} < K_{op}$$

Many experimental techniques have been used to determine the opening force. However, due mainly to its experimental simplicity, the compliance technique is the most widely used approach. The ASTM E647 presents a methodology to determine the opening force and corresponding K_{op} [45]. However, other approaches have been used, i.e. in the case of near-threshold; the effective ΔK can be obtained from a load-compliance plot by using the adjusted compliance ratio (ACR approach). Then, the effective ΔK is defined as [50, 51].

$$\Delta \mathrm{K}_{\mathrm{eff}} = \Delta K \cdot ACR \tag{2-11}$$

where $ACR = (C_s - C_i)/(C_0 - C_i)$, C_i is the specimen compliance before crack initiation, and C_s and C_0 are obtained from the load vs compliance plot as indicated in Fig. 2.13.

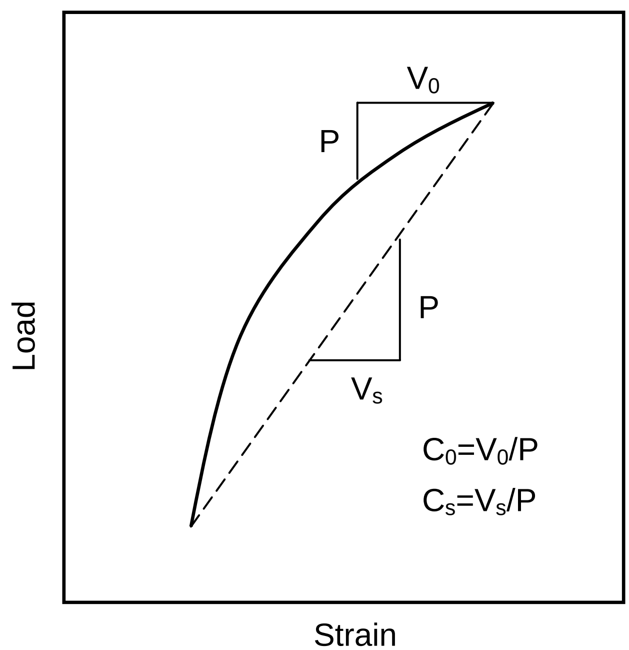

Fig. 2.13 ACR method from load vs compliance plot

In addition, Paris presented a model of partial crack closure that estimates the effective stress intensity factor [52]. This theory also addresses near threshold growth rates in Al-alloys and is based on the fact that low R-ratios and near threshold conditions favor the development of roughness-induced crack closure (RICC) and oxide induced crack closure (OICC) [52].

$$\Delta K_{eff} = K_{max} - (2/\pi)K_{op} \quad \textbf{(2-12)}$$

However, non-unique measurement of the effective threshold stress intensity factor range ($\Delta K_{th,eff}$) for different load ratios has led to a recurring debate over its significance on fatigue crack growth. Thus, another approach has been presented by Kujawski for the driving force parameter for crack growth in aluminum alloys [48]. The model does not utilize disputable crack closure data. In this model the mechanical driving force, ΔK^*, is defined solely based on the positive part of applied stress intensity factor range, ΔK^+, and K_{max} and is calculated as.

$$\Delta K^* = (\Delta K^+ K_{max})^{0.5} \quad \textbf{(2-13)}$$

ΔK^* is calculated as a geometric mean of ΔK^+ and K_{max}. This method shows a fairly good correlation between R-ratio effects and crack propagation rates and threshold condition for various aluminum alloys. A similar model has been presented by Walker, where an affective stress intensity factor is calculated according to equation 2.14 [53]. He demonstrates that it could be used to consolidate the crack growth data for positive R-ratios. However, for negative R-ratios it would be necessary to assume $m=0$.

$$\bar{K} = (K_{max}^{(1-m)} \Delta K^m) \qquad \textbf{with} \qquad m > 0 \quad \textbf{(2-14)}$$

On the other hand, at high ΔK values the crack growth rates increases with increasing R. However, the Paris law does not take into account these characteristics at high levels of ΔK. For this reason, Forman et al. presented the following relationship for crack growth rates at high ΔK values [54].

$$\frac{da}{dN} = C\Delta K^n / \left[(1-R)K_c - \Delta K\right] \quad \textbf{(2-15)}$$

where K_c is the critical stress intensity factor. This equation highlights that da/dN decreases with decreasing stress ratio [55].

Moreover, when ductility plays an important role in the fracture, elastic-plastic fracture mechanics (EPFM) is more accurate to evaluate the dynamic properties of the material than linear elastic fracture mechanics (LEFM). For example, in longer crack lengths, plasticity in front of the crack becomes more significant. In other words, the elastic analysis using ΔK underestimates the behavior of the material at the upper regions II and III, as shown schematically in Fig. 2.14. Thus, analytical tools of EPFM like J-integral or crack tip opening displacement (CTOD) needs to be considered for a more accurate approach of both, crack growth and fracture toughness [40].

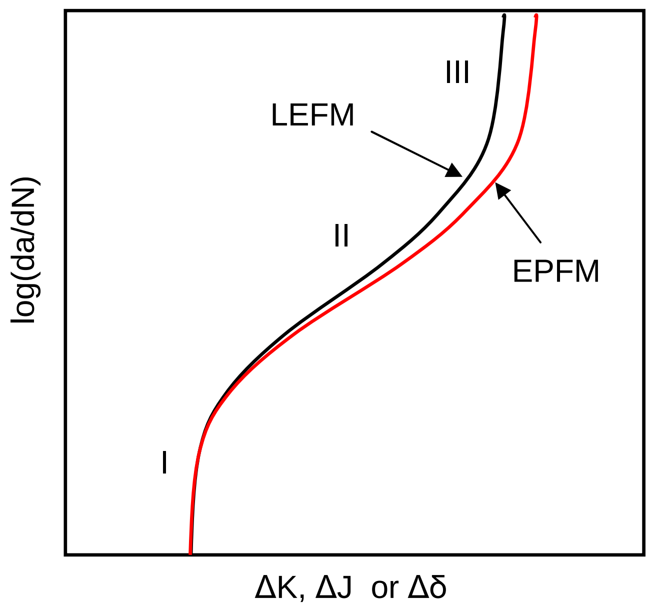

Fig. 2.14 Effect of high plasticity conditions

The ASTM E647 and E1820 standard provide a methodology to determine the parameters ΔK, J *and* CTOD (δ) for the determination of the crack growth rate and fracture toughness respectively. These calculations for some specimen configurations are based in the testing load vs displacement curve.

One of the main factors dominating crack propagation is the CTOD. For this reason relationships between the crack growth rate, da/dN, and CTOD also have been presented, as in equation 2.16 [36].

$$\frac{da}{dN} = D'(CTOD)^{n'} \tag{2-16}$$

2.7 Fatigue Life Prediction Models

Many efforts have been made to describe and model the fatigue and crack propagation processes and then predict fatigue life for cast aluminum alloys. In those models the defects are treated as short cracks. Some of them have been simplified using LEFM; one example is the model proposed by Couper et al. for very short cracks and at stresses near the yield stress.

$$a_i \cdot N_p = \left(C\left(Y(a_i)\sqrt{\pi}\right)^4 \cdot \left(U_R(a_i)\right)^4 \cdot \left(\Delta\sigma\right)^4 \right)^{-1} \tag{2-17}$$

where, $N_p = N_f - N_i$, $Y(a_i)$ is the compliance factor, U_R is a closure factor, $\Delta\sigma$ is the stress range and C, a constant. This model has a good agreement with the experimental results. In addition, the authors identified that cracks initiated not only from casting defects but also by other mechanisms [56].

Using other assumptions Wang et al. obtained the model of equation 2.18 based on fracture mechanics. For cast aluminum alloys with defects such as porosity and oxide films, they conclude that crack propagation comprised most of the total fatigue life. Then the number of cycles to initiate a crack from defects could be neglected [57].

$$a_i \cdot N_p = \left(\left((m-2)/2\right) \cdot C\left(Y(a_i)\right)^m \cdot \left(U_R(a_i)\right)^m \cdot \pi^{m/2}\right)^{-1} \tag{2-18}$$

Other models take into account the shape of a defect. For example, a simple model using Vickers hardness (Hv) and a geometrical parameter ($\sqrt{A}$), is used to estimate the fatigue limit (σ_w) of a specimen containing defects [58].

$$\sigma_w = 1.43 \cdot (Hv + 120) / \left(\sqrt{A}\right)^{1/6} \cdot \left(\left(1 - R\right)/2\right)^{\alpha} \quad \textbf{(2-19)}$$

Where, $$\alpha = 0.226 + Hv \times 10^{-4} \quad \textbf{(2-20)}$$

In general the fatigue life of a component is influenced by numerous factors that are not related to the alloy itself. These factors include loading and surface conditions, and geometry amount others, which can be employed to obtain an approach to predict the fatigue life.

3 EXPERIMENTAL PROCEDURE

Aluminum composite materials manufactured by two different processes were studied. Preliminary impact experimentation was used to determine the effect of particle reinforcements on the impact strength of the composites under study. The measured impact fracture energy was useful to identify the effect of the ceramic reinforcements on the material. Then, monotonic bending tests were developed to obtain the maximum load capacity of samples. Thus, fractions of the loading capacity were used to design the fatigue loading cycles. Fatigue tests with high loading rates were conducted and the crack growth of the different composites was studied to determine the effects of different reinforcement volume fractions.

3.1 Material Fabrication

The specimens were obtained by casting of masters alloys (Al - 33.2 wt.% Cu, Al – 10 wt.% Mg and Al – 5 wt.% B) using a mass balance to obtain the necessary compositions. The melting process was performed under 750 °C to avoid the transformation from AlB_2 to AlB_{12} phase [2-4]. During the whole process, the AlB_2 reinforcements remain in solid state. The casting process was the main difference between the two fabrication methods: A set of samples was prepared by normal casting (gravity), while another set was obtained by centrifugal casting. After each casting process the samples where annealed at 200 ºC for 2 hours, to avoid the influences of the stress concentrations due to uneven cooling rates in the castings.

3.1.1 Normal (Gravity) Casting

This is the most common and economic casting process used in the metallurgical industry. It is used to manufacture at low cost parts with specific and sometimes complicated shapes. In this process an adequate volume of molten metal is poured into a mold, and allowed to solidify within that mold. For this research, the molds were prepared using a silica-based compound. An important variable in the casting process is the cooling rate, which depend of the molten metal/

mold temperature gradient. The material was melted at 750°C using an electrical furnace and placed into the mold at laboratory temperature. The composites obtained by normal (gravity) casting permits to obtain an apparent homogeneous distribution of particles. This allows the composite to present a behavior close to an isotropic material. A typical microstructure of a composite containing 4 wt.% B obtained by normal casting is shown in Fig. 3.1, where small clusters of dispersed particles can be observed.

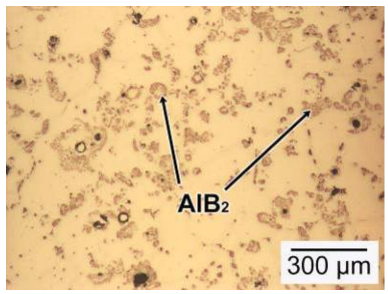

Fig. 3.1 Microstructure of composite (Al-4 wt.% B, 1 wt.% Mg and 2.5 wt.% Cu)

3.1.2 Centrifugal Casting

In this process, the samples are produced using a centrifugal casting machine (see Fig. 3.2). The molten metal from mixing master alloys is placed under centrifugal force action. Due to the density difference between solid denser particles and molten metal, the particles are displaced towards the end of the casting [5].

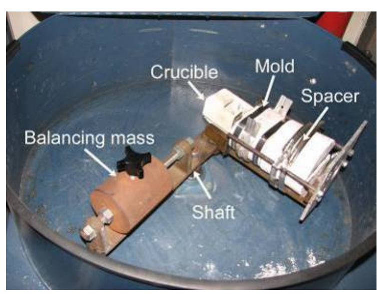

Fig. 3.2 Centrifugal casting set-up

The particle displacements towards the outer casting region lead to a variation of particle volume fraction along the centrifugal force direction (CF direction). In this case, the interest was centered in producing samples with a gradual variation of particles volume fraction along the cross section of the specimen. Fig. 3.3 shows a schematic diagram of the particle distribution in a prismatic sample.

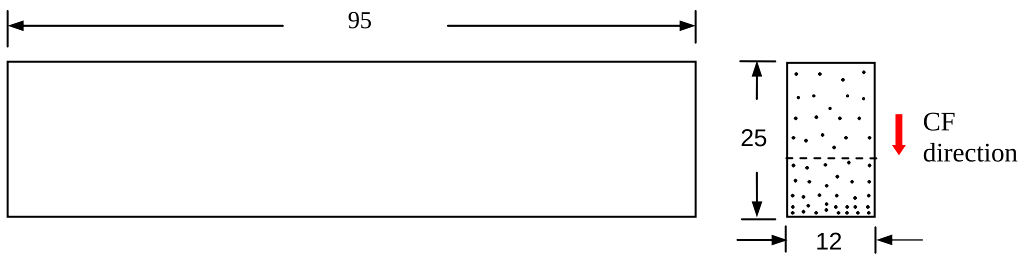

Fig. 3.3 Particles distribution due to particle acceleration after centrifugal casting

The process was carried out systematically via trial and error. The first step was to modify the centrifugal casting machine to support the mold size and geometry.

The parameters that can be adjusted in the process when using the centrifugal caster are: melting temperature, mold material, mold temperature, rotational time, angular velocity and radius of rotation. These parameters control the variables involved in this casting procedure as illustrated in Fig. 3.4

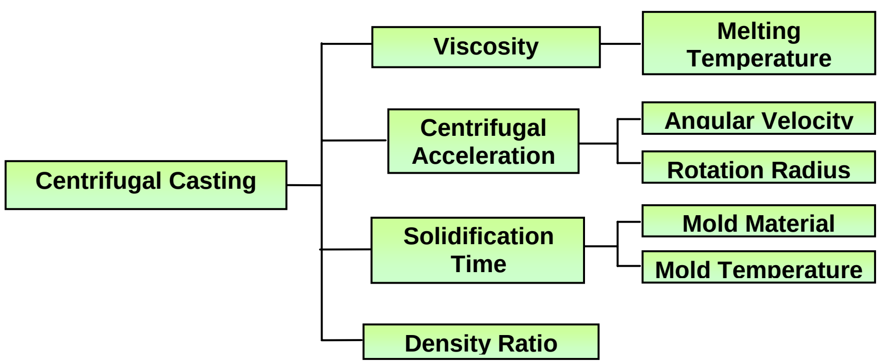

Fig. 3.4 Schematic representation of variable-parameters dependency

The density ratio between the (AlB_2) particle (3.17 g/cm^3) [59] and the liquid aluminum matrix density (approximately 2.4 g/cm^3) [60] at the semisolid composite casting temperatures (>700 ºC) was 1.32.

For each parameter a range of values was tested. For example, two mold materials were utilized. Initially, the same silica compound (SiO_2) employed for gravity casting was used by their durability and thermal shock resistance. Due to its low thermal conductivity (1.4 W/(m·K)) the molten metal remains in semisolid state enough time to permit a complete segregation of particles on the composite.

Graphite has a high thermal conductivity (80-140 W/(m·K)), supports thermal shocks, has a good durability and can be readily machined. With graphite molds, the solidification time was reduced and it was possible to obtain a proper gradual variation of the particle volume fraction.

In both cases it is important to include a beading air system in the mold design to avoid air entrapment in the composite (Fig. 3.5). The air entrapment would cause defects in the functionally graded casting.

a) Silica mold

b) graphite mold

Fig. 3.5 Mold design

The temperature of the molten metal is another critical parameter, as this affects the viscosity of the semisolid material. To select the proper processing temperature a differential thermal analysis (DTA) was used and allowed collecting the thermograms in Fig. 3.6, where a melting signal of 650ºC was recorded. Thus, 700ºC and 750ºC were selected to allow an adequate superheat to increase the fluidity of the molten metal.

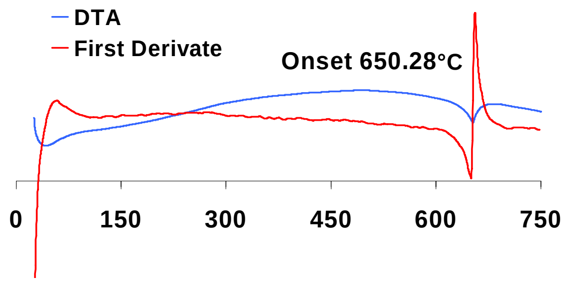

Fig. 3.6 DTA thermogram of the Al-matrix

Low mold temperatures also affect the solidification time by enhancing the cooling rate. Low mold temperatures can generate surface defects on the samples (Fig. 3.7) or lack of appropriated mold filling. In samples obtained using silica compound this surface defects can be controlled preheating the mold at 400ºC. With graphite molds, the samples did not show major surface defects inclusive at room temperatures.

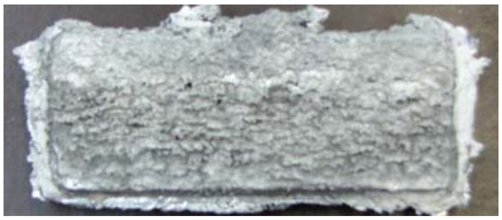

a) Sample from mold at room temperature (25°C)

b) Sample from mold preheated at 400°C

Fig. 3.7 Surface defects due to mold temperature

The hold time at constant angular velocity, called rotational time, was adjusted so as to be larger than the solidification time to ensure that the particle distribution was affected mostly by the centrifugal acceleration only. As a result, values from 3 s to 10 min were tested. The centrifugal acceleration was adjusted by controlling the angular velocity and the radius of rotation of the sample. As shown Table 3.1 different accelerations were tested by combining the angular velocities with the selected radius: 300, 350 and 400 rpm with 25 and 35 mm radii.

Table 3.1 Parameters and values tested

Mold Material	Melting Temp	Mold Temp	Rot. Time	RPM	Radius
Silica Graphite	700ºC 750ºC	30ºC 100ºC 200ºC 300ºC 400ºC	3s 15s 30s 60s 10min	300 350 400	0.25 m 0.35 m

3.2 Microstructure Analysis

The microstructure analysis, critical in the study of this series of composites, required careful sample preparation consisting of grinding with SiC paper up to 1200 grade, followed by polishing using two steps of diamond suspensions as recommended by Struers® [61].

A metallographic microscope was used to characterize the microstructure and to obtain the micrographs used in the quantitative metallography of reinforcement particle size and distribution. Special attention was given to the composites obtained by centrifugal casting, where an accurate quantification of reinforcement volume fraction was required. The measurement of volume fraction of particles was done using the image J® image analysis software. Moreover, the phases present on the composite were studied via SEM using backscattering electron imaging, which allowed identifying the phases by difference in the atomic numbers. Also, energy dispersion spectroscopy (EDS) was employed to obtain mapping of the alloying elements and determine possible interactions between composite phases.

3.3 Impact Testing (Charpy)

The impact tests were carried out using a GALDAVINI Charpy pendulum type IMPACT 450 series V678 with a pendulum hammer of 150J and digital output. In this comparative test, the analysis was performed by taking a sample as reference. The aluminum matrix containing 2.5 wt.% Cu and 1 wt.% Mg was the base material. For this research the Charpy test was useful to study the effect of particle reinforcements on the absorbed energy to fracture of this new series of composites.

3.3.1 Specimen Geometry

Standard Charpy V-notch specimens of each composition were developed as recommended by ASTM E23-07ae1 [29]. Specimens with dimensions of 10x10x55 mm (Fig. 3.8) were developed to carry out the impact testing.

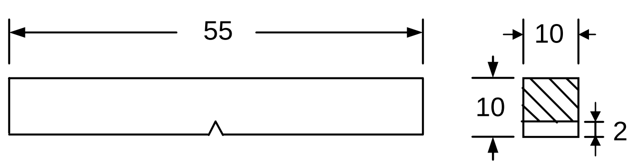

Fig. 3.8 Charpy V notch sample

3.4 Tensile Testing

A set of samples obtained by gravity casting were prepared for tensile test in a universal servo-hydraulic machine MTS model 810 with INSTRON data acquisition and capacity of 100 KN. Without a prior reference of the tensile behavior of these composites, it was decided to employ a load rate of 500 N/min. The standard ASTM D3552 suggests that the samples should be loaded in tension at constant load rate until the failure occurs [62].

3.4.1 Specimen Preparation

Due to material limitations it was decided to use specimens with dimensions smaller than those specified by the ASTM D3552 standard. Also known as sub-size specimens, these are commonly used on materials research, but are considered nonstandard specimens [62]. The ASTM E8/E8M standard for tensile test of metallic materials also was reviewed. This suggests a gauge length of 25 mm for specimens with 6 mm of square section [63]. The specimens were machined and ground to obtain the required dimensions, as shown in Fig. 3.9. Additional tensile tests were carry out to determine the 0.2% offset tensile yield strength σ_{YS} under rapid loading conditions as specified by ASTM E1820 [42]. This standard define rapid loading for metallic materials under conditions where the loading rates exceeds those for conventional (static) testing and the test time is restricted to be no less than one millisecond or the specimen period t_w.

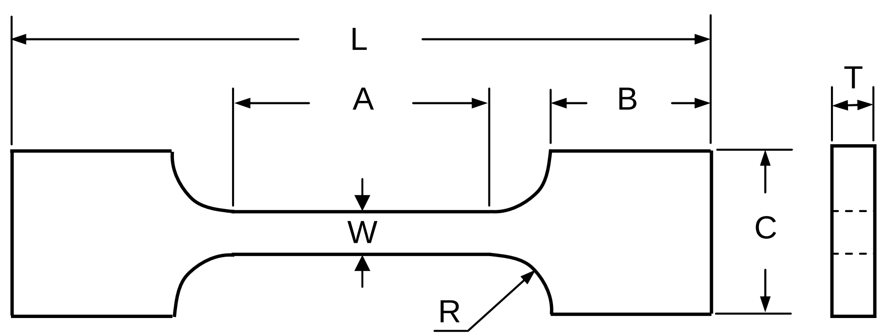

L = 100 **T = 6** **R = 12.7**
A = 32 **W= 6** **Dimensions in mm**
B = 28 **C = 20** **Tolerance: ± 0.05 mm**

Fig. 3.9 Sub-size specimen

3.5 Fatigue Testing (Three Point Bending)

Fatigue tests were conducted to determine the fatigue lifetime under high loading rates. For this purpose a three point bending setup was used in a 25 kN capacity MTS uniaxial testing unit retrofitted with INSTRON electronics. The three-point bending arrangement was selected (Fig. 3.10) for its simplicity and the minimal machining/milling of the ad hoc specimens. Simple bending and high loading rates were utilized by implementing a loading profile with a 0.1s to achieve fatigue maximum load (Fig. 3.11). The maximum load was selected to reach 50%, 60%, 70% and 80% of the failure load, which was measured via a static bending experiment (monotonic loading).

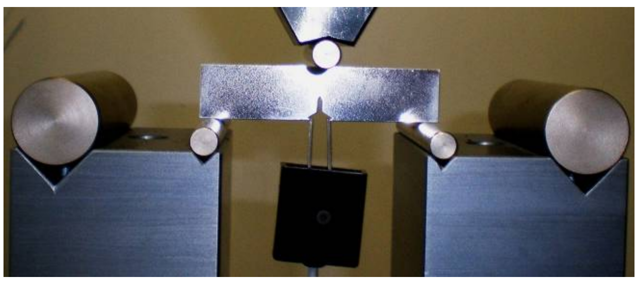

Fig. 3.10 Experimental three-point bending setup

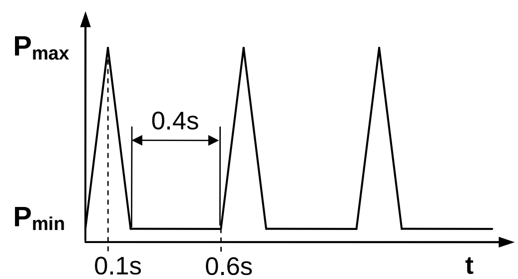

Fig. 3.11 Load profile

3.5.1 Specimen preparation

In this case, the sample geometry and dimensions have been selected so as to perform crack length measurements using the compliance technique. Single edge bend SE(B) specimens with width-to-thickness ratio W/B=2 (Fig. 3.12) was used as the recommended by the ASTM E1820 standard. The notch was specially milled to accommodate the crack-opening device that senses the mouth opening of the notch when the crack is propagating [42].

In most samples the notch was milled to have the crack growing opposite to the centrifugal force direction (CCF direction), i.e. through low particle density area. However, to study the effect of the particle distribution in the crack growth of these composites a group of specimens was prepared so as to have the crack grow in the CF direction.

Each specimen was ground and then polished with diamond suspension and a silica suspension up 0.05 µm following the same procedure used in the microstructure analysis. The finished allows observing the microstructure directly in the microscope.

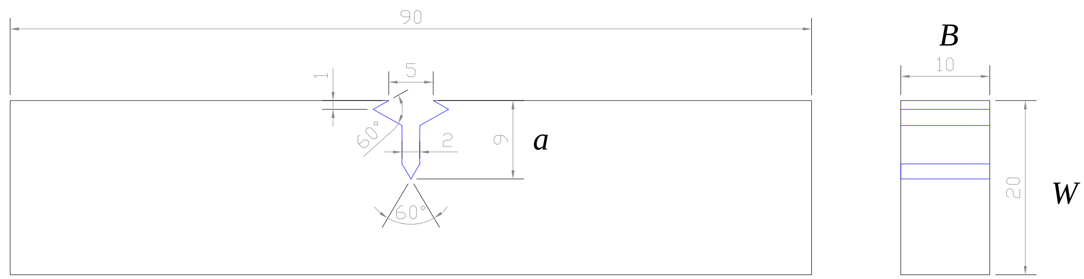

Fig. 3.12 Single edge bend SE(B) specimen (W/B = 2)

3.5.2 Load Control Testing

Triangular load profile was selected with a high loading rate, and a ramping time to maximum load of to 0.1s. This same time was used for the unloading segment with a hold time of minimum load (preload) of 0.4s. The cycle period was 0.6s and the loading frequency was 1.67 Hz.

3.5.3 Crack Length Measurement

Yu et al. define three different types of relations between impact and nonimpact fatigue crack growth rates: (a) The fatigue crack growth rate in impact fatigue is lower than nonimpact fatigue when the yield strength at the crack tip is high; (b) The fatigue crack growth rate of impact fatigue is equal to that of nonimpact fatigue when the yield strength at the crack tip is low; and (c) The crack growth rate in impact fatigue is higher than nonimpact fatigue because brittle fracture takes place under impact fatigue [11]. Additionally, Yang and Liu, and Quispitupa have used the compliance technique to crack length measurements under high loading rates on steels [21, 64]. Due to the ductility of these composite matrix, the crack length in each cycle was calculated employing the compliance technique based on Eq. 3.1 [41, 42], and via visual inspection.

$$a/W = 1.000 - 3.950U + 2.982U^2 - 3.214U^3 + 51.516U^4 - 113.031U^5 \quad \textbf{(3-1)}$$

Where:

$$U = \frac{1}{1 + ((E'BV_m / P)(4W/S))^{1/2}} \quad \textbf{(3-2)}$$

$$E' = E \quad \text{(Plane stress)} \qquad\qquad E' = \frac{E}{(1-\nu^2)} \quad \text{(Plane strain)}$$

a is the crack length and *W* is the depth of the specimen. *Vm*, *P*, *E'*, *v*, *B* and *L* are the crack mouth opening displacement, applied load, effective Young's modulus, Poisson's ratio, thickness and span length, respectively. Using a strain gauge to measure the crack mouth opening displacement (CMOD) and resolving Eq. 1 for *a*, i.e. crack length, the progression of the crack was readily assessed for each consecutive loading cycle. In addition, the calculated crack length was verified via visual inspection using a traveling microscope with 20X magnification lens.

3.5.4 Calculation of the Stress Intensity Factor

The calculation of K_I was carried out following the procedures stated by the ATSM E1820 standard for measured of the fracture toughness [42]. The calculation of K for bend specimens at a force P_i is performed using equation 3.3:

$$K_{(i)} = \left[\frac{P_i \cdot S}{B \cdot W^{3/2}}\right] \cdot f(a_i/W) \quad \textbf{(3-3)}$$

where:

$$f(a_i/W) = \frac{3\left(\frac{a_i}{W}\right)^{1/2} \cdot \left[1.99 - \left(\frac{a_i}{W}\right)\left(1-\frac{a_i}{W}\right)\left(2.15 - 3.93\left(\frac{a_i}{W}\right) + 2.7\left(\frac{a_i}{W}\right)^2\right)\right]}{2\left(1+2\frac{a_i}{W}\right)\left(1-\frac{a_i}{W}\right)^{3/2}} \quad \textbf{(3-4)}$$

When plasticity occurs the calculation is performed in terms of the J integral. For this purpose a load-line displacement is used while the crack mouth displacement was utilized to calculate the crack size.

Calculation of J includes an elastic component as well as a plastic component according to equation 3.5.

$$J_{(i)} = J_{el(i)} + J_{pl(i)} \tag{3-5}$$

where:

$$J_{el(i)} = \frac{K_{(i)}^{\ 2}\left(1-\nu^2\right)}{E} \tag{3-6}$$

K is calculated from eq. 3.3 with $a = a_0$

$$J_{pl(i)} = \frac{\eta_{pl(i)} \cdot A_{pl(i)}}{B \cdot b_i} \tag{3-7}$$

where:

$A_{pl(i)}$ = area under force vs crack mouth opening displacement record to v_i

$\eta_{pl(i)} = 3.785 - 3.101\left(a_i / W\right) + 2.018\left(a_i / W\right)^2$, and

$b_i = W - a_i$

3.6 Fracture Surface Analysis

Fractured specimens were analyzed by means of secondary electron microscopy and optical stereoscopy. Microscopic analyses provided understanding of the fracture mode and evolution in the structural member and helped to identify the fracture pattern of these materials. Scanning electron microscopy (SEM) was used to analyze the fractures. The SEM (magnifications from 10-10000X) were helpful to obtain qualitative information of fatigue striations [24] and an optical microscope (magnifications from 1-20X) was used to study the macroscopic features of the fracture surface such as beach marks and river patterns.

4 RESULTS AND DISCUSSION

4.1 Microstructure Analysis

This segment of the dissertation is divided in two sections: the first one dedicated to gravity casting samples and the second, focused on the fabrication of centrifugal casting samples. In both cases the aluminum matrix is constituted by Al – 2.5wt.%Cu – 1 wt.%Mg. Therefore, in order to abbreviate figure captions, in the microstructures analyses of the composites only the content of boron is reported. In addition is it important to note that the microstructural analysis of the matrix was conducted only on gravity casting samples.

The phases present in the composite were identified using as reference the microstructure analyses performed in a prior research on AMCs with similar compositions [4]. In this work the identification of the phases was based on the study of the Al-master alloys used to fabricate the composite.

4.1.1 Gravity Casting Samples

After studying micrographs of gravity casting samples, the ones of the aluminum matrix in Fig. 4.1 and Fig. 4.2 were selected to observe de overall appearance of the matrix and to indentify the thermodynamically stable θ phase respectively. In these samples the presence of pores was minimal.

Moreover, the micrographs in Fig. 4.3 and Fig. 4.4 corresponding to a 4 wt.%B composite allow indentifying the AlB_2 particles. In Fig. 4.3 AlB_2 particle clusters are observed reinforcing the material, while Fig. 4.4 is the magnification of a rectangular area in Fig. 4.3, where the particles can be observed in detail; for example, in this figure some particles are oriented so that their hexagonal morphology of the AlB_2 dispersoids is visible.

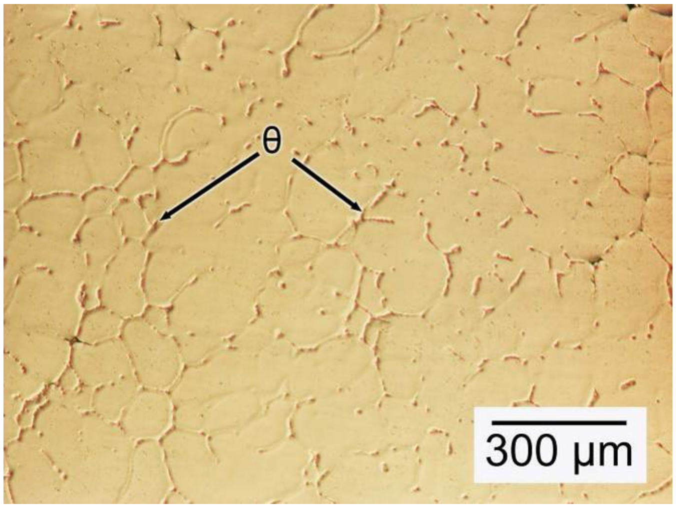

Fig. 4.1 Appearance of matrix microstructure.

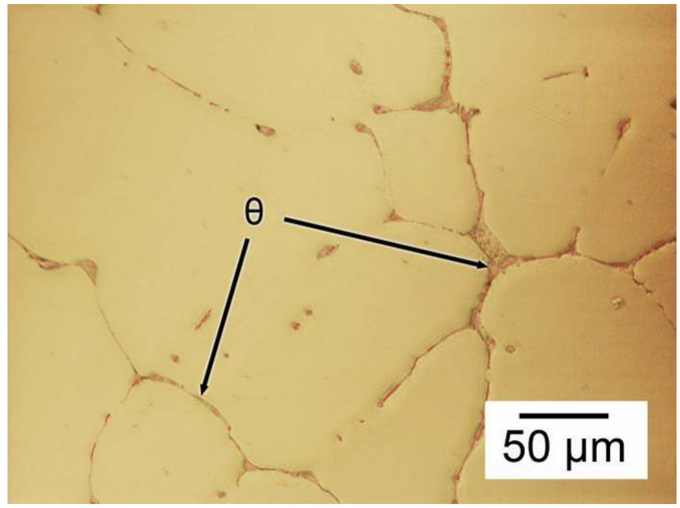

Fig. 4.2 Morphology of θ phase in the aluminum matrix.

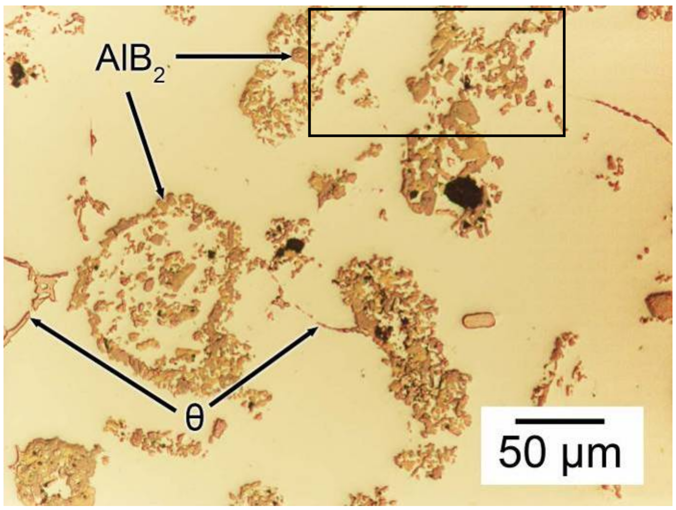

Fig. 4.3 Optical image of a composite containing 4 wt.%B showing clusters of AlB_2 particles.

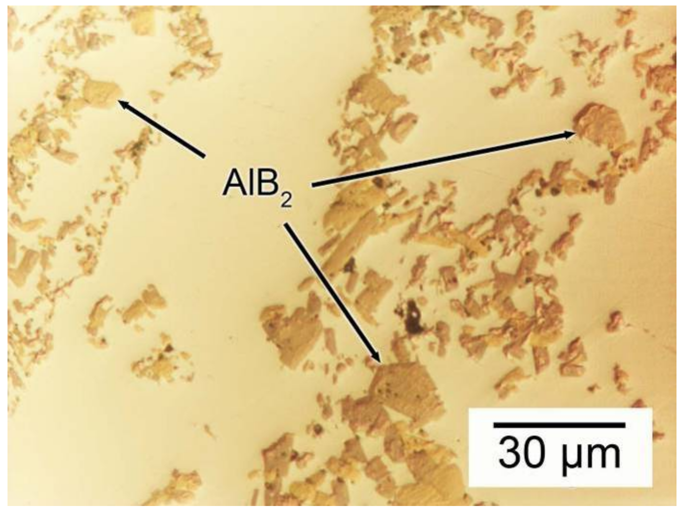

Fig. 4.4 Image of a area in Fig. 4.3 show in detail Clusters exhibiting AlB_2 hexagonal particles.

Once the phases in the composite were indentified, several micrographs were used for calculation of the volume fraction of particles and pores for each composite. The overall appearance of the composite microstructures containing 1, 2, 3 and 4 wt.%B are present in Fig. 4.5a to d respectively. Fig. 4.6 and Fig. 4.7 show the volume percent of particles and pores respectively. In Fig. 4.6 the error bars represent confidence intervals of 95%, while in Fig. 4.7 the negative part of the error bar was omitted, leaving open the possibility to find pore free areas in the composites.

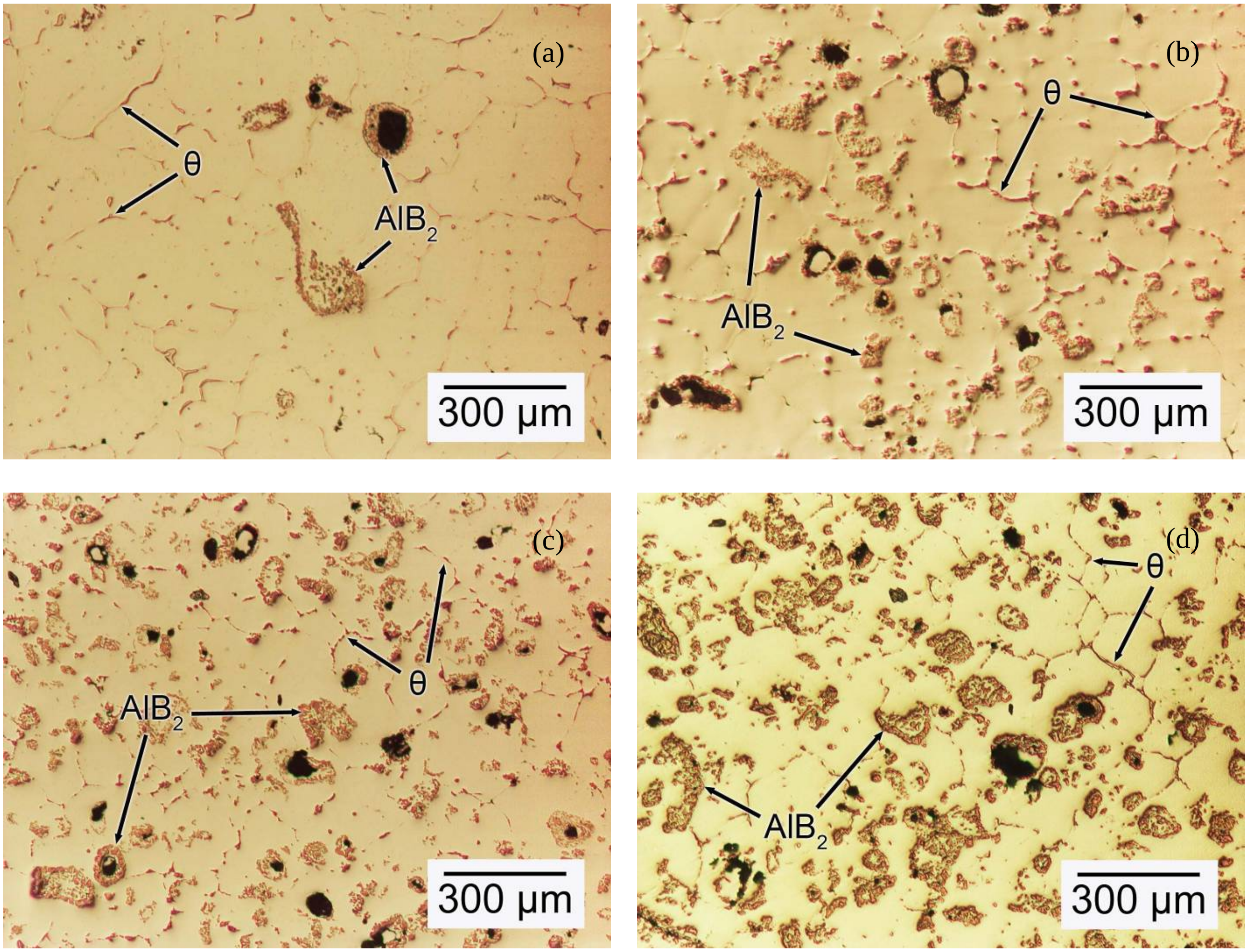

Fig. 4.5 Micrographs of composites with different weight percent of boron a) 1 wt.%B, b) 2 wt.%B, c) 3 wt.%B and d) 4 wt.%B.

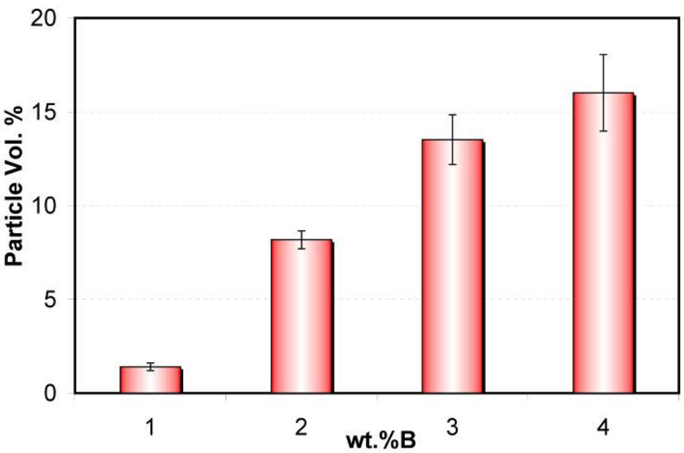

Fig. 4.6 Particle volume percent as function of wt.%B

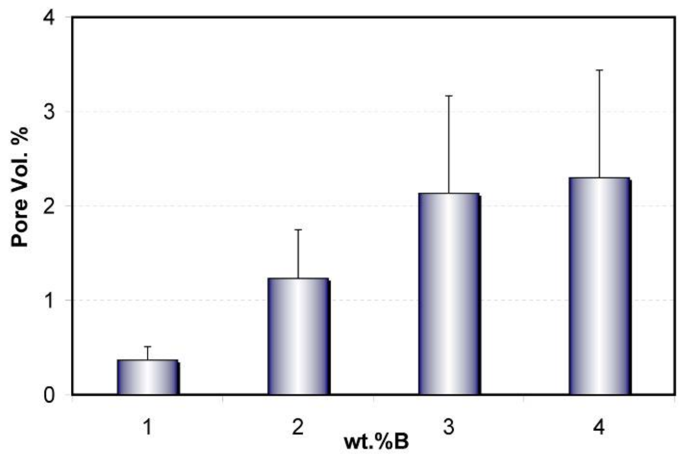

Fig. 4.7 Pores volume percent as function of wt.%B.

The results in Fig. 4.6 show that in general the volume fraction of particles in this series composite increases with the weight percent of boron, varying from 1.4% for samples containing 1 wt.%B to 16% for those with 4wt.%B. This variation is evidenced by Fig. 4.5. Moreover, the volume percent of pores also increases with the wt.%B: from 0.37 to 2.30% for the composites containing 1 and 4 wt.%B, respectively. Since several micro pores appear surrounded by particles, such increment in the porosity could be associated to a process of gas entrapment inherited from the Al-B master alloys. [65].

In general, the particle size ranged from 1 to 30 μm, while the average size of pores was around 50 μm and in few cases reached 100 μm. The pore size appears to be higher in comparison with the critical value of 25 μm reported to avoid the influence of porosity on the mechanical properties of the A356 type alloy [40]. This point to the need of other casting methods intended to reduced such porosity, e.g. squeeze casting [66].

4.1.2 Centrifugal Casting Samples

By adjusting the processing variables one can obtain composites with different characteristics. After a systematic fine-tuning process two types of particle segregation were achieved. Initially, complete particle segregation was obtained using silica molds. As mentioned before, the low thermal conductivity of this material is responsible of a slow cooling rate, which allows enough time for the particles to travel through the molten aluminum during the centrifugal casting process. Finally, gradual segregation of the particles along of the centrifugal force direction was achieved by employing graphite molds. The high thermal conductivity of this material reduces the solidification time, which permits controlling the gradual displacement of the particles by adjusting the casting parameters. To summarize, the parameters combinations employed with each mold material to achieve the two types of particles segregation are presented in Table 4.1.

Table 4.1 Parameters recommended using with each mold material.

Mold Material	Melting Temp	Mold Temp	Rot. Time	RPM	Radius
Silica	700ºC	400ºC	60s	300	0.25 m
Graphite	750ºC	200ºC	60s	350	0.35 m

In Table 4.1 it is evident that for short solidification times, for example using graphite molds, high levels of melting temperature, angular speed and radius of gyration are needed to promote the particles displacement, reaching 48 g forces. On the other hand, by using silica molds only 25 g are enough to achieve the complete segregation of particles. In these samples the extended solidification time causes the layer thickness profile of particle segregation to become sensitive to the mold geometry, as illustrated in Fig. 4.8.

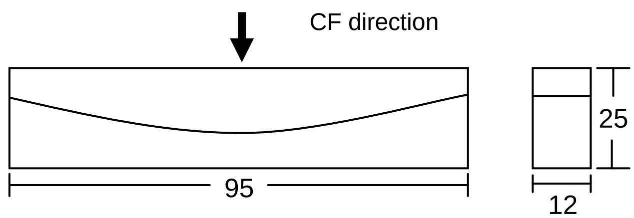

Fig. 4.8 Segregation profile model.

In addition the layer thickness of diborides decreases with smaller particle loading. Then to study the microstructure of these samples cuts from the mid section were prepared and three zones were defined in each specimen: zone 1 (highest particle segregation), zone 2 (transition) and zone 3 (particle-depleted matrix), as in Fig. 4.9.

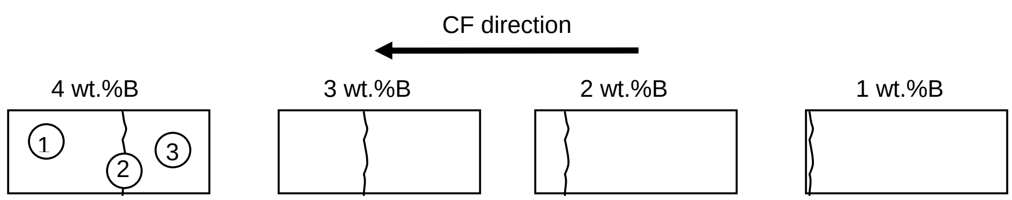

Fig. 4.9 Sketch of layer thickness in the center cross section of the specimens.

The resulting microstructures in each zone are presented in Fig. 4.10, where the increment in the particles volume fraction with the wt.%B in the zone 1 is apparent, as well as in the reinforced areas of the zone 2 (transition). Although the change in the particles layer thickness is not clear in this figure, the micrograph corresponding to the zone 2 of the composite containing 1 wt.%B shows the particles layer thickness around 400 μm. The small size of this layer does not permit obtaining a well defined micrograph of the zone 1 using the same magnification. This result exemplifies the layer thickness change, i.e. layer containing segregated particles, by comparing the 1 wt.%B and 2 wt.%B composites.

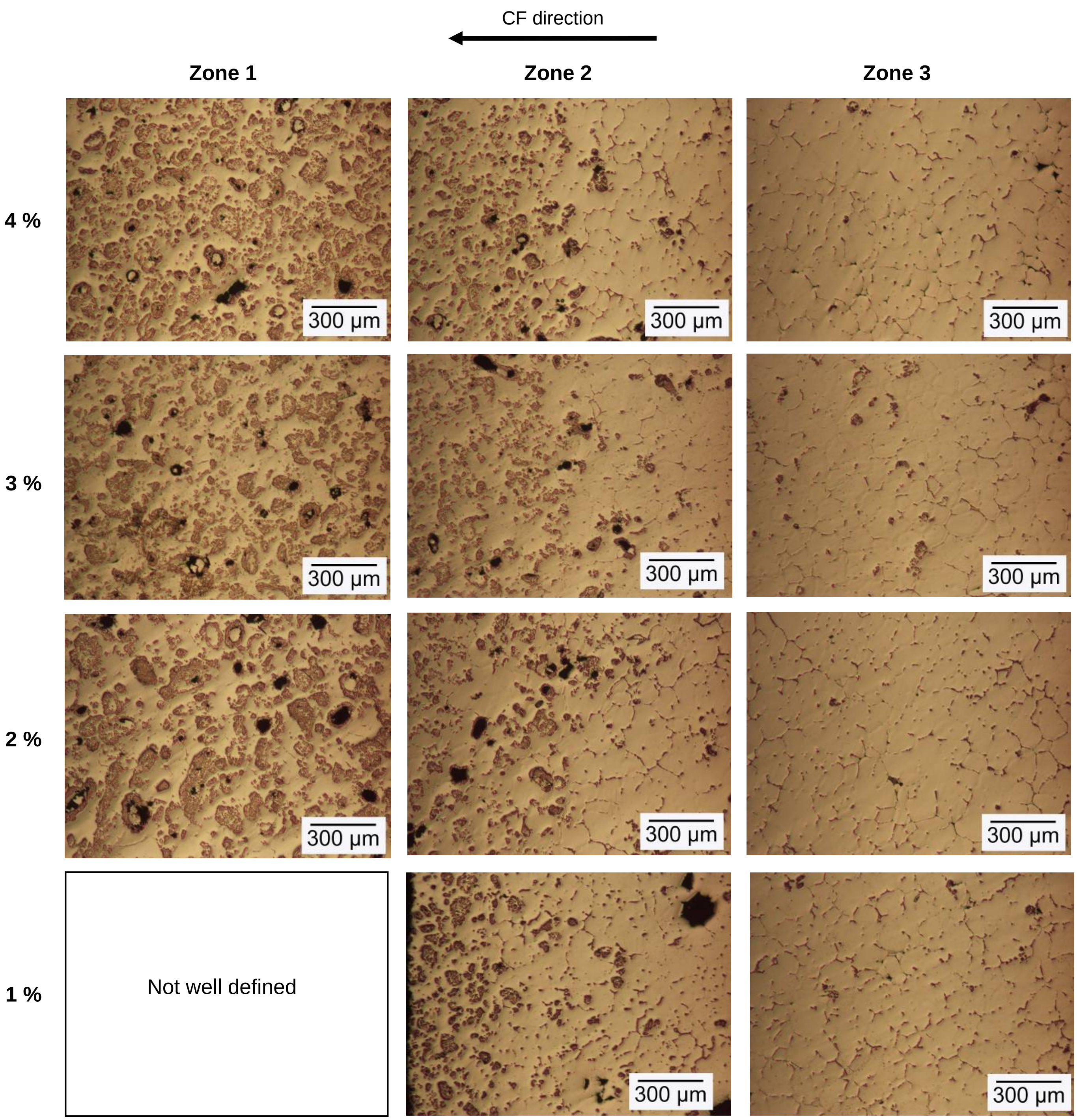

Fig. 4.10 Microstructures in the three defined zones for samples with different weight percent of boron obtained using silica mold.

In general the study of samples obtained using silica mold permits to achieve complete particle segregation with layer thickness controlled by the weight percent of boron (particle volume percent). This would be helpful in applications where the wear resistance is a critical factor. However, since the objective was to obtain a gradual variation of the volume fraction along the CF direction in each specimen, the microstructural analysis was focused in the samples obtained using a graphite mold.

Then, to study the evolution of the microstructure along the CF direction, cuts near to the mid section of the samples were selected and micrographs were obtained from three areas (red circles) in the extreme with high density of particles, which was designated now as zone 1; the center of the cross section, indentified as zone 2; and the extreme with low density of reinforcements, called zone 3, as illustrated in Fig. 4.11.

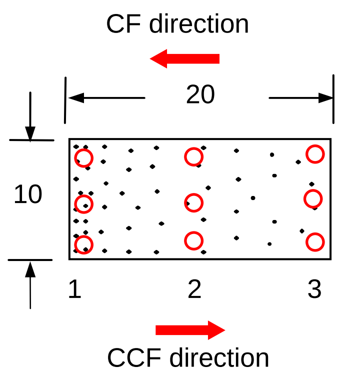

Fig. 4.11 Schematic illustration of areas selected to study in the cross section

The micrographics obtained were utilized to perform the volume fraction calculations of particles and pores and some images were selected to illustrate the evolution of the microstructure as the weight percent of boron increased, as shown in Fig. 4.12. In this figure the gradual variation of the particles volume fraction along with the CF direction in each wt.%B is evident.

Such variation in the particle volume percent was quantified and the results are presented in Fig. 4.13. In the same manner the volume percent of pores was also calculated in each zone and the results are presented in Fig. 4.14. These numbers are not apparent in Fig. 4.12. This is due to the high data dispersion of porosity. However, in general, the volume percent of pores was found to increase as the volume fraction of particles increases.

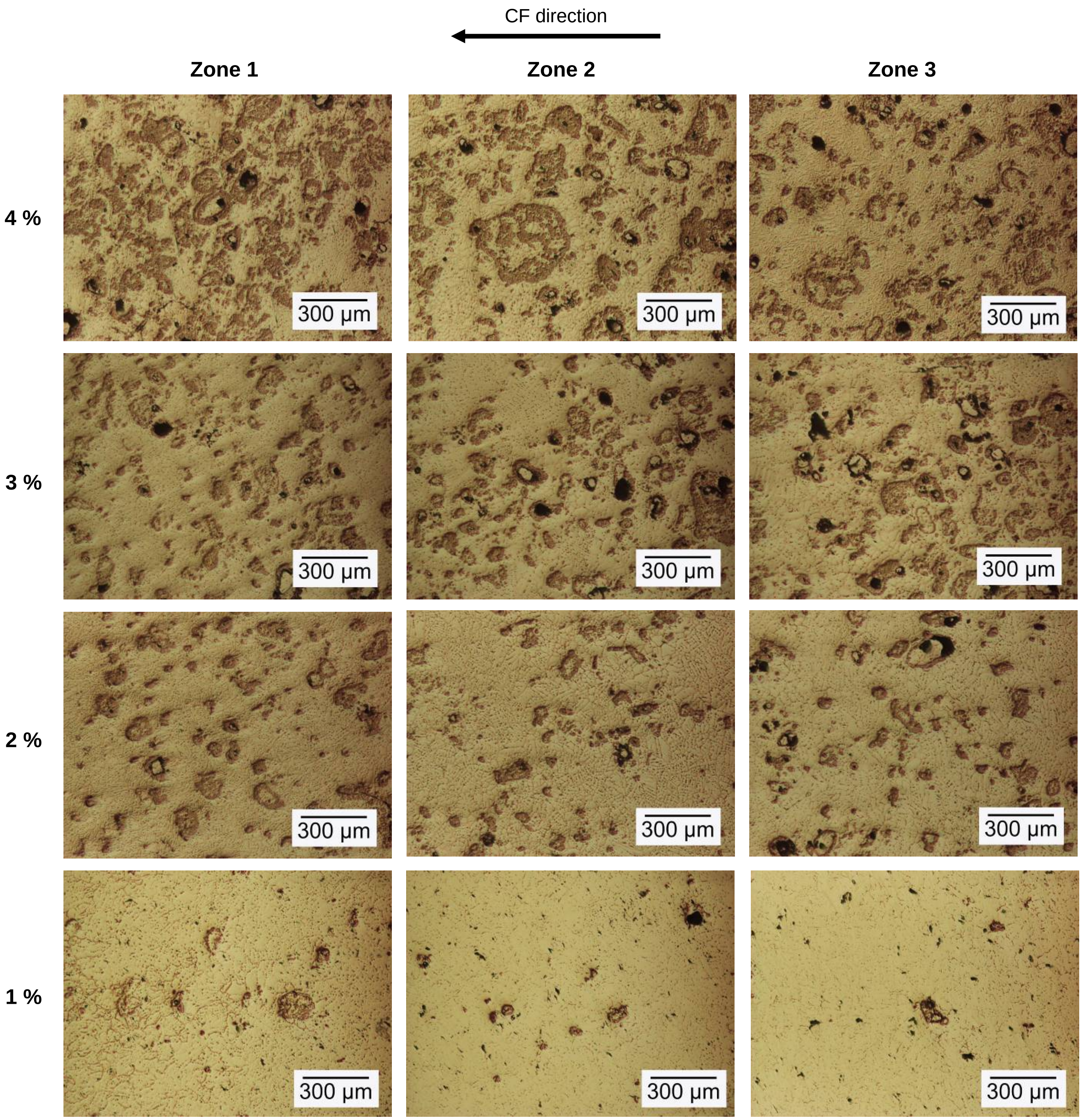

Fig. 4.12 Micrographs corresponding to center and edges, along of the CF direction, of samples with different weight percent of boron, obtained using graphite mold.

For the sake of comparison, in these two figures (4.13 and 4.14) the results from gravity samples were plotted again. Thus, the volume fraction of gravity casting samples appear to be close to the volume percent of the center zone for each wt.%B (see Fig. 4.13), while centrifugal casting samples exhibited smaller porosity than those samples obtained via gravity casting (Fig. 4.14). This reduction in porosity could result in an improvement of the mechanical properties of these FGMs in comparison with the gravity cast samples.

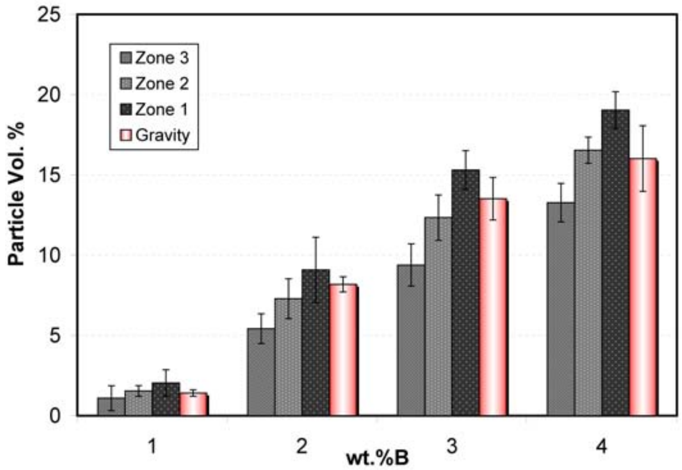

Fig. 4.13 Particles volume percent of FGMs in zones defined in Fig. 4.12.

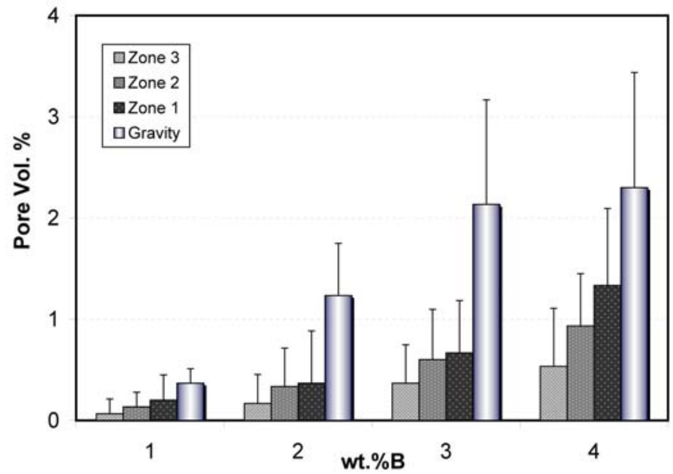

Fig. 4.14 Pores volume percent of FGMs in zones defined in Fig. 4.12.

Again in Fig. 4.14 the negative component of the error bars was omitted, since the possibility to find pore free areas is present in each zone. In addition, for reference the average values of particles and pores volume fraction are presented in Table 4.2.

Table 4.2 Mean Volume percent of particles and pores.

wt.%B	Particles volume percent				Volume percent of pores			
	Zone 1	Zone 2	Zone 3	Gravity	Zone 1	Zone 2	Zone 3	Gravity
1	2.03	1.53	1.08	1.40	0.20	0.13	0.07	0.37
2	9.08	7.28	5.42	8.18	0.37	0.33	0.17	1.23
3	15.30	12.33	9.38	13.51	0.67	0.60	0.37	2.13
4	19.03	16.53	13.27	16.01	1.33	0.93	0.53	2.30

4.1.3 Discussion

Gravity casting samples showed a relatively good distribution of the particles clusters. In these samples volume percent of particles from 1.40 to 16.01 % were approximately obtained for specimens containing 1 and 4 wt.%B respectively. In addition, the average values of gravity casting samples showed values close to the central zone of the cross section in centrifugal casting samples with the same wt.%B. This is reasonable since charging the same weight percent of boron to these two types of composites, the segregation of particles caused by the action of the centrifugal force produced zones with high and low density of particles, but in the average the composite contains an amount of particles similar to those contained in those samples obtained via gravity casting.

Moreover, in the fabrication of centrifugal casting samples the principal parameter to determine the proper particle distribution was the thermal conductivity of the mold material, since this variable affects the solidification time of the molten metal [67]. For example, for high cooling rates (graphite mold) the solidification front affects the particle distribution by hampering or even stopping the displacement of the particles, affecting the gradual variation of the particle volume fraction along with the CF direction. On the other hand, for slow cooling rates (silica molds) the molten metal keeps its fluidity for the required time to achieve a complete segregation of particles.

Although complete segregation of particles was the main objective of this work, those results are presented only as a reference. This serves to demonstrate that using the centrifugal casting process controlled variations in the material microstructure can be achieved.

In general, the gradual variation in the volume percent of particles along the cross section was around 40 % of the average particle volume percent obtained in gravity casting samples for each wt.%B. Thus, the difference in the amount of particles between the edges of the cross section increases with the wt.%B.

Moreover, since to study the effect of particle distribution, the notch in the majority of the FGM samples was prepared to promote the crack growth opposite to the centrifugal force direction (CCF direction) and some specimens were prepared to lead the crack to growth along in the crack growth direction (CF direction), the particle volume fraction information corresponding to the cross section center (zone 2) is valuable to determine the particle volume fraction change in the fractured section. For instance, for 4 wt.%B the change in the particle volume fraction through the particle denser section would be the difference between the results of zone 2 and zone 1 (2.50 %).

4.2 Particles Effect on the Fracture Impact Energy

The impact absorbed energy as function of the weight percent of boron is presented in Fig. 4.15. A significant variation in the measured energy as a result of increasing the quantity of AlB_2 dispersoids was not observed. However, unpublished work shows a positive correlation of the impact energy as the proportion of particles increases in similar composites reinforced with particles of both AlB_{12} + AlB_2 instead of AlB_2 [68].

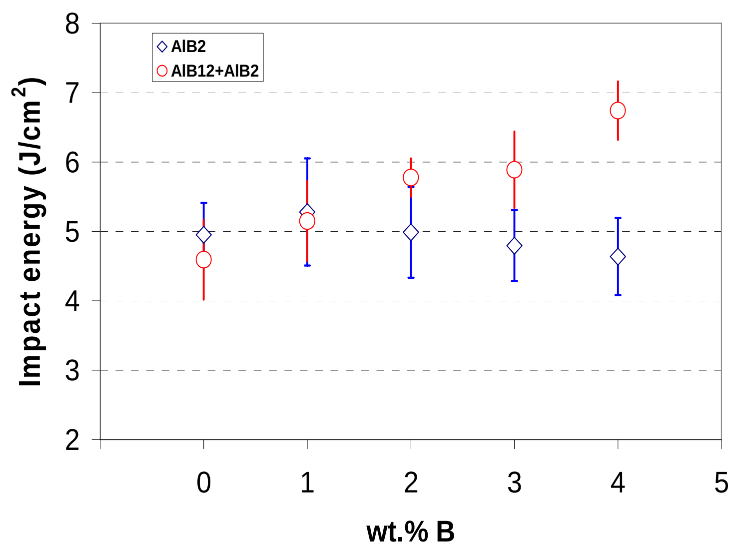

Fig. 4.15 Impact energy vs boron level in composites with matrix containing Al-2.5wt.%Cu-1wt.%Mg

At this point, it is important to consider that the presence of reinforcing particles in an aluminum matrix usually results in an increase of the composite stiffness and loss of ductility [69], behavior that also has been observed in Al-Cu-B composites reinforced with AlB_2 [70]. Thus, the increase in impact energy of samples reinforced with AlB_{12} + AlB_2 does not appear to be a direct consequence of increasing the amount of boron (and the subsequent amount of particles). For this reason, microstructure analyses were employed to study the origin of this tendency, initially associated with the presence of Mg and/or AlB_{12} in the composite. For instance, the microstructure of Fig. 4.16 corresponding to a specimen reinforced with AlB_{12} + AlB_2 with prevailing presence of AlB_{12} and some small AlB_2 particles, allowed identifying the phases present in each composite.

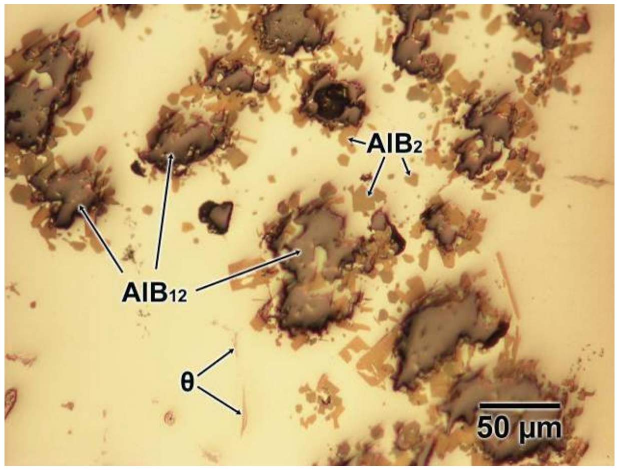

Fig. 4.16 Optical micrograph of sample containing Al - 2.5wt.%Cu - 1wt.%Mg - 4wt.%B

SEM observations permitted analyzing quantitatively and qualitatively the elements present in the composites. By this means, AlB_2 and AlB_{12} reinforcements were indentified assisted by backscattered electron imaging, as depicted in Fig. 4.17. Dark particles correspond to AlB_{12} while light gray ones are AlB_2.

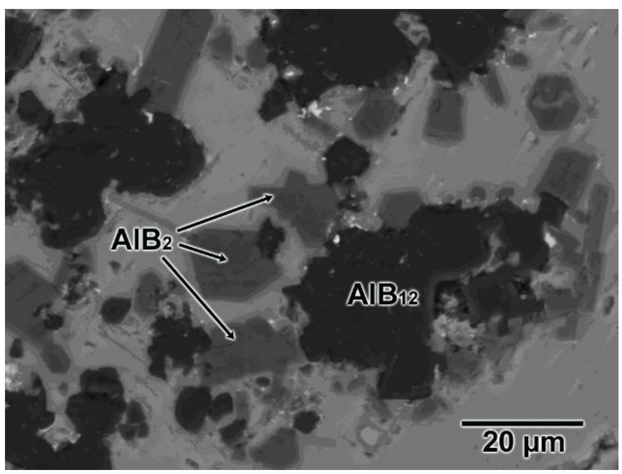

Fig. 4.17 Backscattered electron image of composite containing 2.5 wt.%Cu - 1wt.%Mg - 4 wt.% B (with boron forming AlB_{12} and AlB_2)

EDS allowed quantifying the chemical composition of the phases present in the composites. Coupled with x-ray mapping, EDS was able to reveal the interaction between Mg and the AlB_2 particles (Fig. 4.18a). In Fig. 4.18b higher concentration of magnesium is evident within AlB_2 particles but not in the AlB_{12} ones. After establishing the interaction between the Mg present in the matrix and the AlB_2, this work focused mainly on composites reinforced solely with AlB_2 and additional analyses were completed in order to estimate the amount of Mg absorbed by the particles, which will be discussed in a later section.

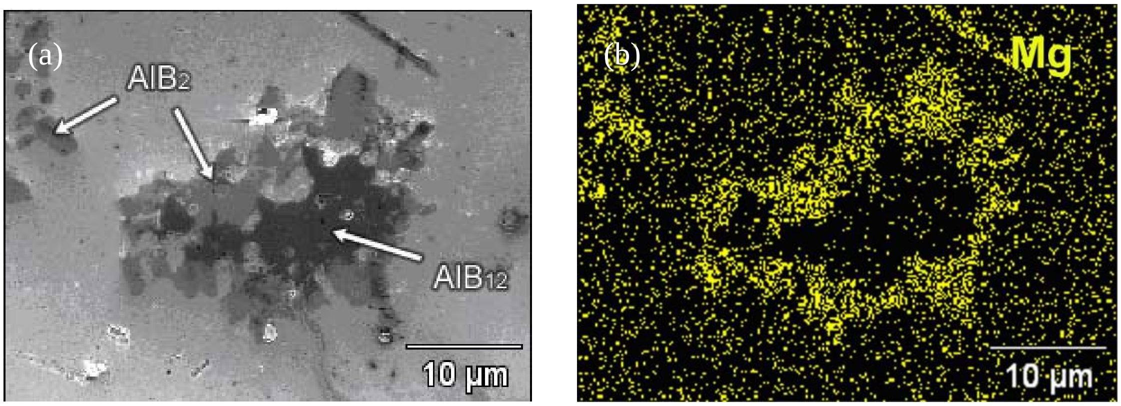

Fig. 4.18 EDS analysis in composite with 4wt.%B (AlB_{12} + AlB_2)
a) SEM image of composite microstructure, b) EDS mapping of Mg of the area in a.

4.2.1 Fracture Surface Analysis

A first look on the fracture surface of composites fabricated via gravity casting allows identification of the samples reinforced with the AlB_2 ceramic particles. The color of the surface changes from light to dark grey as the weight percent of boron increases in the sample, as shown in Fig. 4.19. The photographs in this figure, nevertheless, do not reveal major differences in the fracture morphology on these composites.

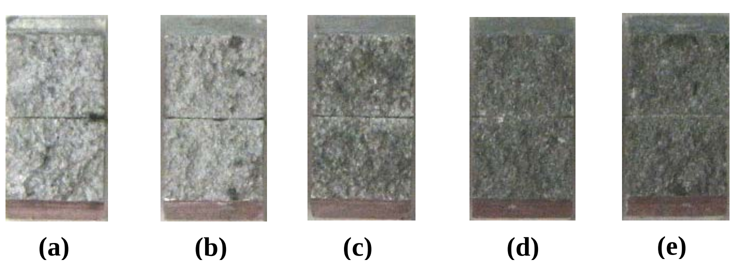

Fig. 4.19 Fracture surfaces photographs for different boron levels:
(a) 0wt.%B, (b) 1wt.%B, (c) 2wt.%B, (d) 3wt.%B, (e) 4wt.%B

Moreover, high magnification images of the fracture surface of these composites in Fig. 4.20, shows a combination of ductile and brittle fracture. In general, predominant presences of cleavage facets with areas of dimple rupture were the principal fracture characteristics of these composites.

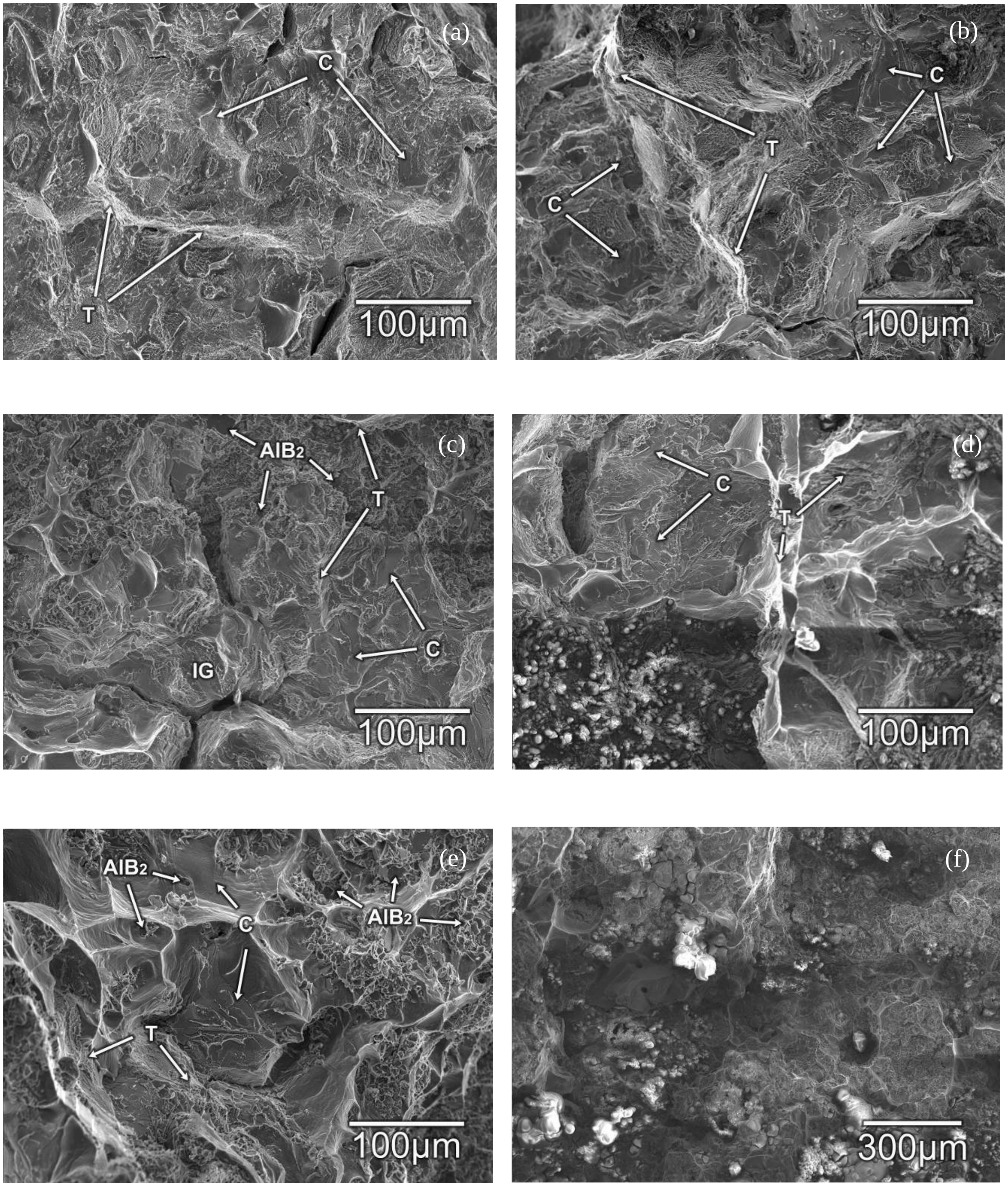

Fig. 4.20 High magnification SEM images of fracture surface of impact samples (a) 0wt.%B, (b) 1wt.%B, (c) 2wt.%B, (d) 3wt.%B, (e) 4wt.%B, (f) Casting defects on sample with 4wt.%B

Since tearing and cleavage areas (identified as T and C in the images respectively) were present in each photograph, the failure mode was defined as quasi-cleavage. However other characteristics like microcracks, intergranular fracture (IG), inclusions and oxides were occasionally observed in some samples and associated to the casting process. To illustrate, some of those casting defects are presented in the fractographs of Fig. 4.20d and Fig. 4.20f.

In general, fractured samples of 0 and 1wt.%B (with lowest levels of boron), Fig. 4.20a and Fig. 4.20b respectively, showed a higher presence of tearing than samples with 3 and 4wt.%B, Fig. 4.6 d and e respectively. Therefore, although the presence of fine ceramic particles was observed in ductile areas, the increment of brittle areas was associated with the presence of coarse clusters of particles, as illustrated in Fig. 4.20e. Additionally, the fracture analysis does not reveal evidence of the mentioned interaction occurring between the Mg in the matrix and the AlB_2 particles.

4.2.2 Discussion

Analyzing only the composites reinforced with AlB_2 the effect of the reinforcements is not clear. Although the mean values show small differences, the variability described by the error bars (95 percent of confidence) suggest there are not significant differences between samples as a consequence of the level of boron. On the other hand, in samples with the same matrix reinforced with AlB_{12} + AlB_2 the impact energy increase with the level of boron. However, such tendency could not be justified by the strengthening mechanisms associated to the presence of hard particles in a ductile matrix [31]. This discrepancy and additional microstructural analyses via SEM, shows an interaction between the Mg and the AlB_2 particles. In other words, the results from samples reinforced solely with AlB_2 did not allow the identification of such an interaction.

This could be corroborated by the fracture surface analysis, since there was no observed evidence of the mentioned interaction. In addition, the study showed a fracture behavior predominantly brittle with presence of tearing, which was denominated quasi-cleavage. The presence of some defects was associated to the casting process and those defects did not show a big influence over the measured impact energy as depicted by the error bars in Fig. 4.15.

The increase of the absorbed fracture energy as the level of boron increases in composites with AlB_{12} + AlB_2 can be explained by a weakening of the matrix due to the migration of Mg atoms to the particles. The interaction process in these composites containing both AlB_{12} and AlB_2 is not clear. Since the material is obtained using an Al-B master alloy forming solely AlB_{12}, the presence of the AlB_2 particles is explained by the transformation from tetragonal AlB_{12} to hexagonal AlB_2. Such transformation has been observed to be promoted by the presence of Mg in the matrix [71]. This could be associated to the affinity between the crystal structures of AlB_2 and MgB_2, since the literature reports a large solubility between AlB_2 and MgB_2 [72, 73]. Nevertheless, this solid phase transformation mechanism requires more study.

Moreover, since the particles remain solid at the processing temperatures, the interaction Mg-AlB_2 in composites reinforced only with AlB_2 was attributed to a diffusion process. To further understand the effect of the apparent diffusion of Mg into the diboride, microhardness tests, quantitative EDS analyses and X-ray diffraction techniques were employed and will be discussed in section 4.4.

4.3 Composite Hardness Analysis

After determining that composites absorbed impact energy of the composite was indeed affected by the Mg-AlB_2 interaction, the matrix microhardness results were inspected. These results as well as those of superficial hardness tests performed on the composites reveled also to be effected by the interaction mentioned. In Fig. 4.21 and Fig. 4.22, matrix microhardness and superficial Rockwell hardness HR-15T respectively, samples containing Mg showed a decrease in microhardness as the proportion of reinforcement increased.

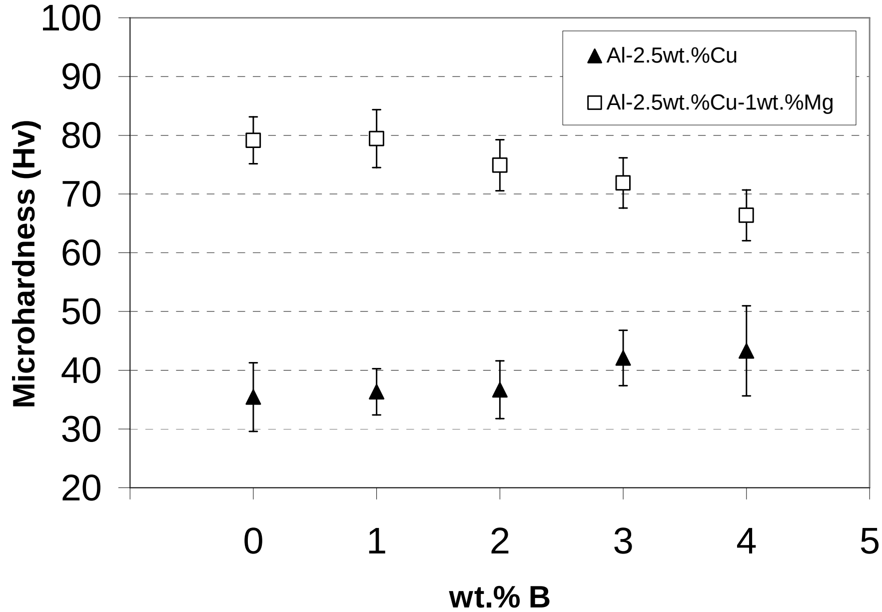

Fig. 4.21 Matrix microhardness (Hv) of Composites

On the other hand, in those figures, data of samples without Mg in the matrix (Al-2.5wt.%Cu) illustrated the typical behavior of aluminum composites reinforced with particles. For instance, the particles did not have a major effect on the matrix microhardness, only on samples with high levels of boron (3 and 4 wt.%B) the matrix microhardness is influenced by the high concentration of particles, which likely promote high dislocations density near the interfaces due to the mismatch between the particles and matrix expansion coefficients [31].

Again, the contradictory behavior observed in samples containing Mg was attributed to the Mg-AlB_2 interaction. Thus, with more particles in the composite more Mg is depleted from the matrix, promoting further matrix weakening.

To study this weakening, the matrix hardening was accessed by performing microhardness tests on samples containing 2.5wt.%Cu with percents of Mg between zero and one, as shown in Fig. 4.23. The matrix microhardness increment is evident and the resulting curve fitted can be used to relate the Mg level in the matrix with its microhardness. For instance, if the Mg level in the matrix is reduced below 1wt.% the hardness of the material will be also reduced.

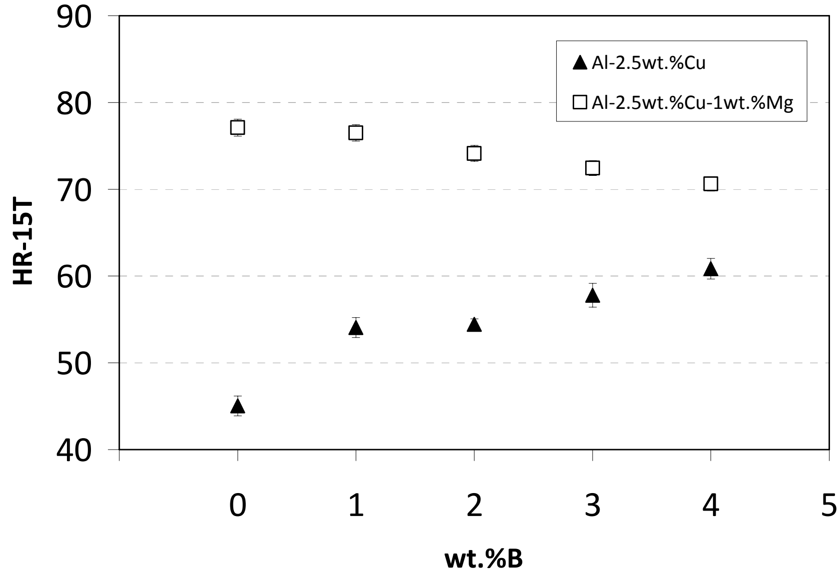

Fig. 4.22 Composites superficial hardness Rockwell HR-15T

In general, the study of the composites hardness indicates that those composites containing Mg showed the highest hardness values compared with those without Mg, as illustrated in Fig. 4.21 and Fig. 4.22. In addition, the hardness on the composites containing Mg decreased as the magnesium level in the matrix is reduced as a consequence of the Mg-AlB_2 interaction.

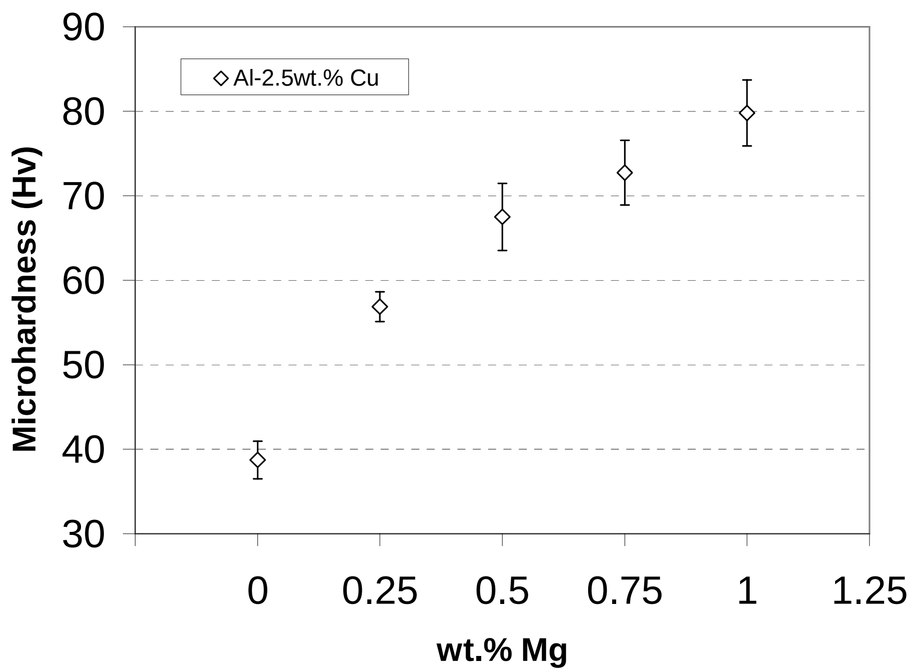

Fig. 4.23 Matrix microhardness (Hv) as function of Mg level

4.3.1 Discussion

This comparative study between samples with and without Mg was helpful to clarify the opposing behavior; it also indicates that the composites containing Mg presented the highest hardness values.

Furthermore, the tendency on the hardness curves of composites containing Mg was also associated to the Mg-AlB_2 interaction. In terms of ductility, these results corroborated the behavior observed for absorbed impact energy. In other words, the matrix is softened, resulting in an increment in the absorbed impact energy of the material and a reduction in the hardness. The matrix softening in composites reinforced with AlB_2 particles can be explained by the reduction of the Mg level in the matrix due to the migration of Mg atoms from the matrix to the solid AlB_2 dispersoids.

In addition, if we assumed that the matrix softening depend only on the reduction of Mg level in the matrix, the curve of Fig. 4.23 could be used to estimate the percent of Mg present in the matrix after the interaction takes place and if the matrix microhardness is known.

4.4 Mg-AlB_2 Interaction

The Mg-boride interaction reported in this work is responsible for the depletion of the Mg level on the composite matrix and likely occurred during the casting process. The high temperature attained during this process provided the necessary energy to activate the diffusion of Mg atoms into the AlB_2 structure, as schematically illustrated in Fig. 4.24.

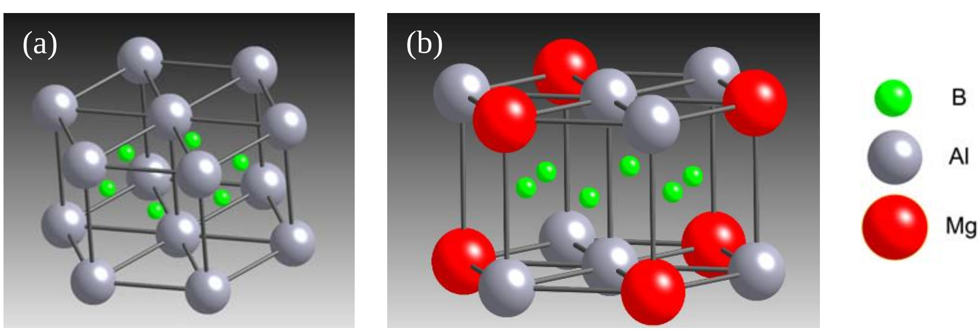

Fig. 4.24 AlB_2 hexagonal crystal structure
a) AlB_2 structure, b) $Al_{1-x}Mg_xB_2$ doped structure with x=0.33

In order to determine how much Mg diffused into the AlB_2 particles during the interaction, three approaches were used. In the first one, the matrix microhardness was correlated with the proportion of Mg present in the matrix. In a second approach, the Mg taken by the particles was also detected by quantitative EDS analysis. The third approach consisted in modeling the x-ray diffraction pattern of AlB_2 reinforcements doped with different proportions of Mg using CrystalMaker® and CrystalDiffract® software. Then were assessed and correlated to the amount of Al atoms substituted by Mg during the diffusion process.

4.4.1 Matrix Microhardness Approach

If we assume that the matrix microhardness is related to the level of Mg present in the matrix after Mg depletion caused by the Mg-AlB_2 interaction, then the percent of Mg can be estimated for a given matrix microhardness. For instance, the curve in Fig. 4.23 can be used to obtain a regression model in order to express the matrix microhardness (Hv) as function of weight percent of Mg (x) present in the solid solution matrix. The model is presented in Equation 4.1 and show a high R-square value, which indicates the appropriateness of the fitted model.

$$Hv = -31.467x^2 + 70.667x + 39.593 \qquad R^2 = 0.9911 \qquad \textbf{(4-1)}$$

Then, for instance, if a certain amount of Mg diffuses into the diboride particles in the sample containing 2wt.%B Fig. 4.21, the weight percent of Mg associated to its sample microhardness (74.9) is 0.75 and the actual amount of Mg absorbed by the particles would be 0.25 wt.%. Such amount of Mg can diffuse into the reinforcements if 11.1% of all Al atoms in the diboride unit cell are replaced by Mg ones. The resulting chemical formula of the doped ceramic particles would then be $Al_{0.889}Mg_{0.111}B_2$.

4.4.2 Quantitative EDS Analysis

In this approach, the Mg taken by the particles was detected by quantitative EDS analysis on particles of AlB_2 in a specimen containing 4wt.% B. For instance, Fig. 4.25 presents the atomic percent of Mg and Al in the particle, in the matrix-particle interface and in the matrix of a sample containing both AlB_{12} and AlB_2. Then, the results of each EDS spot were summarized in Table 4.3.

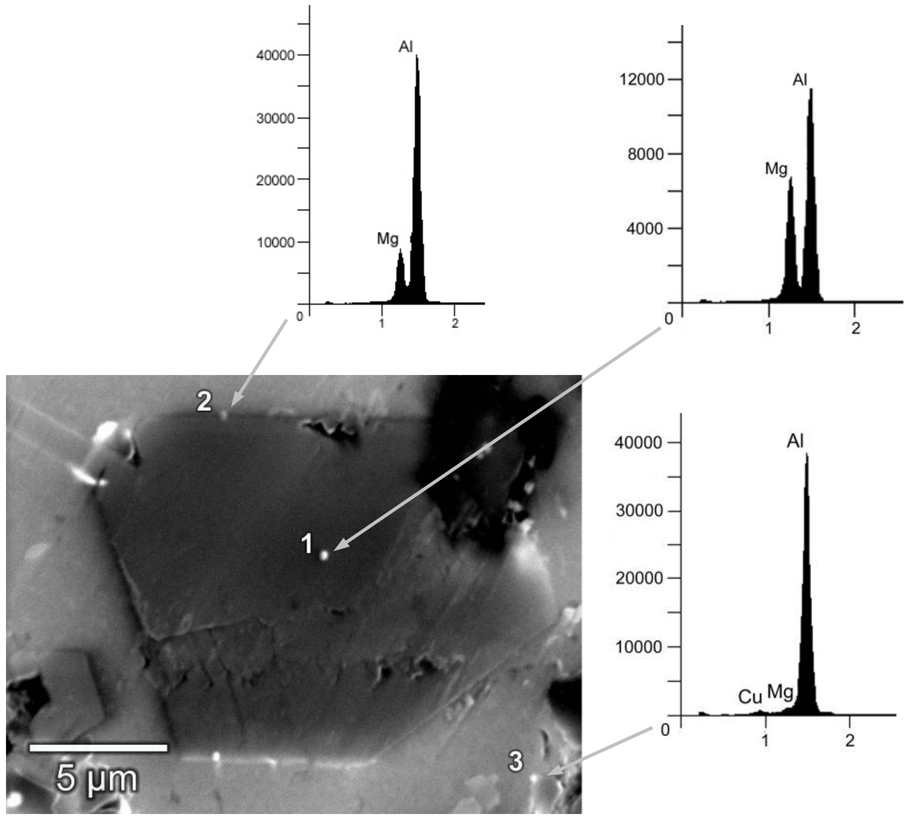

Fig. 4.25 EDS analyses on sample of Al-2.5wt.%Cu-1wt.%Mg with 4 wt.% B. Spots on particle (1), matrix-particle interface (2) and matrix (3) indicate the level of Mg present in each case

Table 4.3 Relative atomic percent of the elements in each spot on Fig. 4.25

Element	Particle (spot 1)	Interface (spot 2)	Matrix (spot 3)
Al	68.38	82.43	96.83
Mg	31.62	16.35	0.5
Cu	ND*	ND	2.41

*Not detected. Element not detected.

The results in Fig. 4.25 indicate that the level of Mg in the particles and the interface (matrix/particle) is higher than the level of magnesium in the matrix. In addition, based in the atomic percent of elements presented in Table 4.3 the percent of Mg measured in the particle is 31.6 %. Consequently, the formula of the doped particle would be $Al_{0.684}Mg_{0.316}B_2$, Moreover, the same study was performed on samples solely reinforced with AlB_2, as shown in Fig. 4.26a. The results revealed lower levels of Mg in the AlB_2 particles. This suggests that the phenomena that influence the presence of Mg in AlB_2 in composites with these two types of reinforcements, is different. Then, to corroborate if a diffusion process take place on samples reinforced solely with AlB_2, part of the sample was annealed at 630°C for 4 hours (Fig. 4.26b).

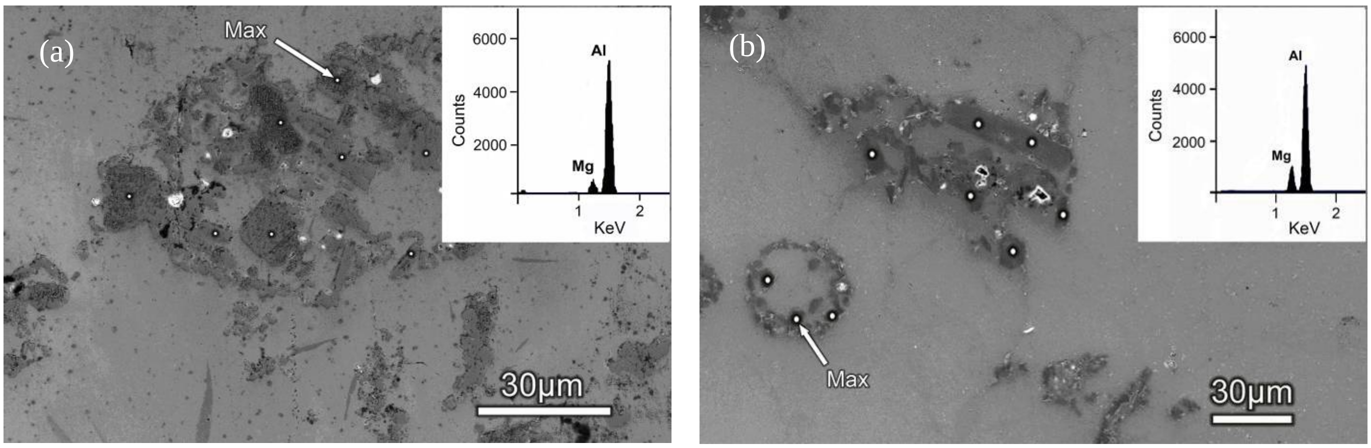

Fig. 4.26 EDS analyses on particles of composite containing 4 wt.% B (solely AlB_2).
a) As Cast specimen, b) Heat Treated sample

The annealed sample showed higher level of Mg in the diboride particle compared with the as-cast specimen. The mean values of the chemical compositions on the spots were summarized in Table 4.4 and illustrated in Fig. 4.27, where the maximum levels of Mg were also included.

Table 4.4 Mean of relative atomic percent of the elements in the spots

Element	AlB_2 As Cast	AlB_2 Heat Treated
Al	92.18	87.68
Mg	7.82	12.32

This is evidence that a diffusion process occurred and was responsible for such interaction in samples with AlB_2 reinforcements only. Thus, the chemical formula of the Mg- doped particles in an as-cast specimen would be $Al_{0.922}Mg_{0.078}B_2$.

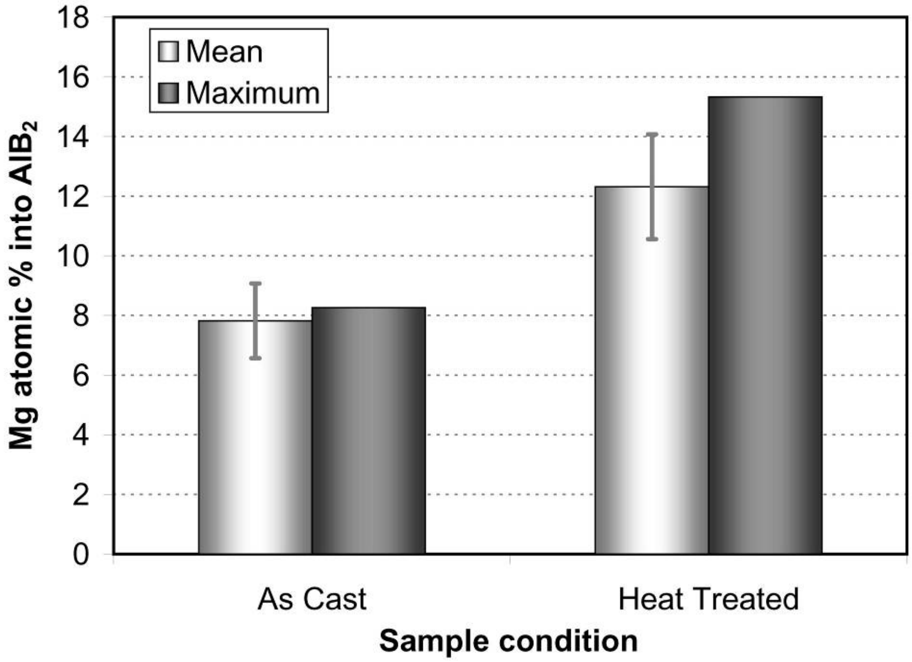

Fig. 4.27 Variation in the relative atomic percent of Mg due to heat treatment

Nevertheless, the mechanism responsible of higher levels of Mg into AlB_2 particles in samples containing also AlB_{12} is not clear. Since the material is obtained using an Al-B master alloy forming solely AlB_{12}, the presence of the AlB_2 particles is explained by the transformation from tetragonal AlB_{12} to hexagonal AlB_2. Such transformation has been observed to be promoted by the presence of Mg in the matrix [71]. This could be associated to the affinity between the crystal structures of AlB_2 and MgB_2, since the literature reports a large solubility between AlB_2 and MgB_2 [72, 73]. Nevertheless, this solid phase transformation mechanism requires a more extensive study.

4.4.3 X-Ray Diffraction Modeling

To estimate the Mg present in the reinforcements consisted in modeling the x-ray diffraction pattern of AlB_2 reinforcements doped with different amounts of Mg using CrystalMaker® and CrystalDiffract® software. The positions of the peaks observed in the modeled x-ray diffractograms were then compared with the ones obtained experimentally on the composite samples.

Values of X in the formula $Al_{1-x}Mg_xB_2$ between 0.1 and 0.2 were selected and the lattice parameters for each X value were calculated using Vegard's rule [74]. Starting from the lattice parameters of AlB_2 and MgB_2 [59, 75] as end points, the lattice parameter *a* and the *c/a* relation were obtained by interpolation, then the parameter *c* was calculated [72, 76] and presented in Table 4.5.

Table 4.5 Calculated lattice parameters for X values modeled

AlB_2	3.0054	3.25276	1.082305
x	**a**	**c**	**c/a**
0.10	3.0135	3.2792	1.0882
0.15	3.0176	3.2925	1.0911
0.20	3.0216	3.3057	1.0940
MgB2	3.0864	3.5215	1.140973

To model the diffraction patterns of the doped AlB_2 structure, the first step was to construct the models of the hexagonal structure with the information presented in Table 4.5 using CrystalMaker®. Then, the peak positions corresponding to each plane were obtained using CrystalDiffract® and are presented in Table 4.6. These values were compared with the peak shifts experimentally detected in the diffraction study of samples containing Mg with 2 and 4 wt.%B (Fig. 4.28).

The diffraction patterns presented in Fig. 4.28 correspond to composites containing Mg with 0 (matrix), 2 and 4 wt.% B, as well as the matrix and the composite containing 4 wt.% B without Mg. In this figure, the peaks corresponding to the phases Al_2Cu and AlB_2 were indentified in samples without Mg. Then, the peak shift due to the presence of Mg was evident when the diffraction patterns of samples containing boron of these two groups of samples were compared. This confirms that in effect, Al atoms are replaced by Mg atoms during the material processing.

Table 4.6 2θ Peaks positions for different X values from CrystalDiffract® modeling and experimental data

Plane	X					
hkl	AlB_2	0.10	0.15	0.20	MgB_2	4% B
001	27.418	27.17	27.06	26.95	25.27	**27.38**
010	34.414	34.33	34.28	34.24	33.48	**34.26**
011	44.542	44.32	44.21	44.10	42.41	**PC***
002	56.539	56.04	55.79	55.55	51.89	**56.01**
110	61.694	61.49	61.39	61.30	59.89	**61.40**
012	67.907	67.39	67.14	66.90	63.17	**ND****
111	69.77	68.47	68.33	68.19	66.04	**ND**
020	72.56	72.35	72.24	72.13	70.40	**ND**
021	79.219	78.88	78.72	78.56	76.13	**ND**

* Peak confounded. Peak of (011) plane overlaps with the Al (200) peak.
** Not detected. Peaks have low intensity.

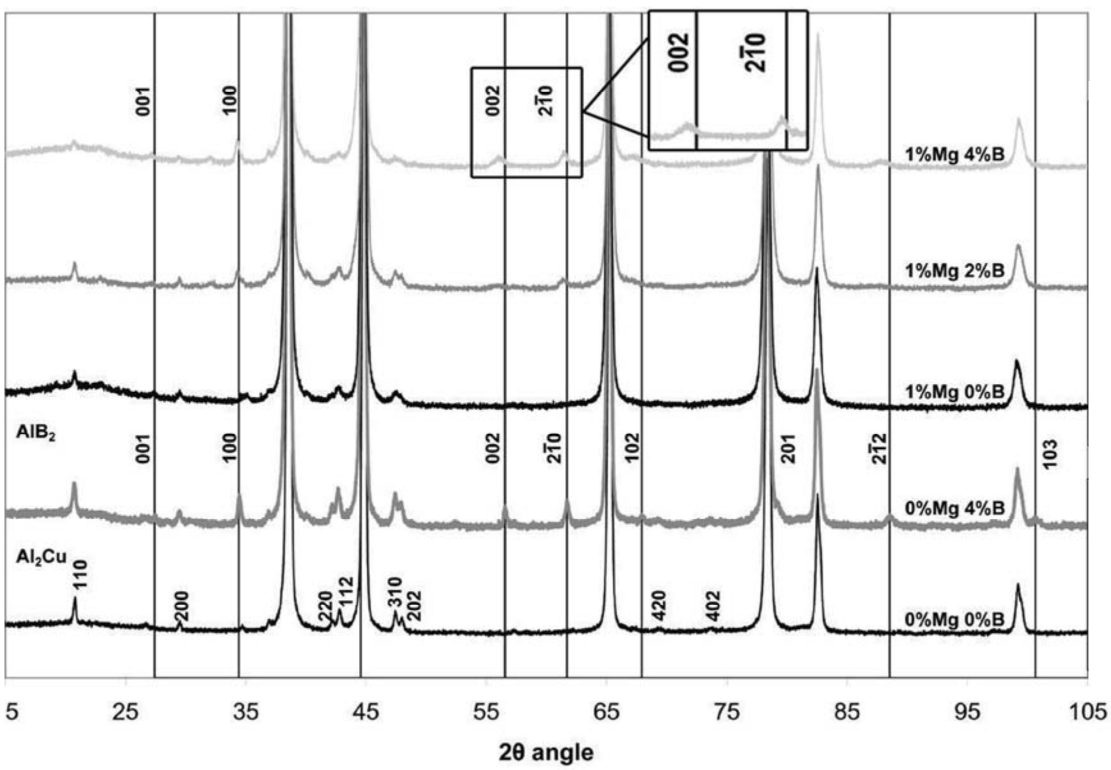

Fig. 4.28 Diffraction patterns of samples with and without Mg

Then, for clarification purposes, the positions of the detected peaks in the sample containing Al-2.5wt.%Cu-1wt.%Mg with 4wt.%B in Fig. 4.28 were also included in Table 4.6. The results presented in this table suggest that approximately 15% of Al atoms have been substituted by Mg to promote the peak shift detected. Then, the chemical formula of doped diborides would be $Al_{0.85}Mg_{0.15}B_2$. This represents an X value higher than the obtained by the other approaches for the composites containing only AlB_2 particles

4.4.4 Discussion

A first look at the results permits inferring that the addition of boride particles to an aluminum matrix with Mg in solid solution could result in a negative effect on the strength of the composite. This was reflected by the impact and hardness tests as a reduction of the composite stiffness as the level of boron increases. However, if it is possible to determine the amount of Mg taken by the particles, such quantity could be used to correct the mass balance prior to the composite fabrication in order to obtain the best benefit of the reinforcements.

Taking into account the three approaches, the range of the atomic percent of Mg into AlB_2 would be between 8 and 15 % for the composites containing only AlB_2 particles. Thus, those X values indicate that the Mg diffusing into the particles is approximately between 0.09 and 0.169 the weight percent of boron respectively. Additionally, an X value of 0.316 was obtained using the EDS analysis. This value is almost double of the X values obtained with the other analyses. This could be explained since the EDS study was developed in a particle of AlB_2 of a sample with 4wt.%B containing both AlB_{12} and AlB_2. As illustrated before the presence of AlB_2 in this type of sample result from the transformation of the AlB_{12} to AlB_2, which is promoted by the presence of Mg [71]. In this case the tetragonal AlB_{12} structure transform into the hexagonal doped structure $Al_{(1-x)}Mg_xB_2$. However, the transformation mechanism is not clear and this would be the cause of the difference of the x value calculated using the EDS analysis.

Moreover, although several works have been realized to study XB_2 doped structures [72, 73, 76], this is the first time that an Mg-AlB_2 interaction activated by a diffusion process is reported to be the cause of the decrease in strength of particle reinforced composites. By this reason, the analyses developed to obtain the approaches presented in this section represent the principal contribution to understand the mechanical behavior of composites with diboride particles in presence of Mg.

4.5 Tensile Testing

The monotonic and rapid loading tests performed in the composites showed similar results, as illustrated in Fig. 4.29 and Fig. 4.30, which present the tensile curves of the matrix and composites reinforced with AlB_2 respectively. It is apparent that there was not clear difference or tendency as a result of the rapid loading. For each composition the results were summarized in an average curve (green curve),

Moreover, if the tensile curves of particle reinforced samples in Fig. 4.30 are compared, the differences between consecutive levels of boron are small. This can be explained by the combined effect of the particle strengthening mechanisms and the Mg-AlB_2 interaction. In other words, while the particles reinforce the material, the interaction Mg-AlB_2 is reducing the strength of the matrix. In general, the results of composite samples were within a range of 110 to 150 MPa. In addition, the results of the composites with different levels of boron revealed a similar trend than the results of the impact and hardness tests: higher levels of boron are detrimental to the strength of the material. For instance, the average yield strength of the composite reinforced with 4 wt.%B was 95.23 MPa, is around 75% of the average exhibited by the matrix (128.41 MPa), as illustrated in Table 4.7.

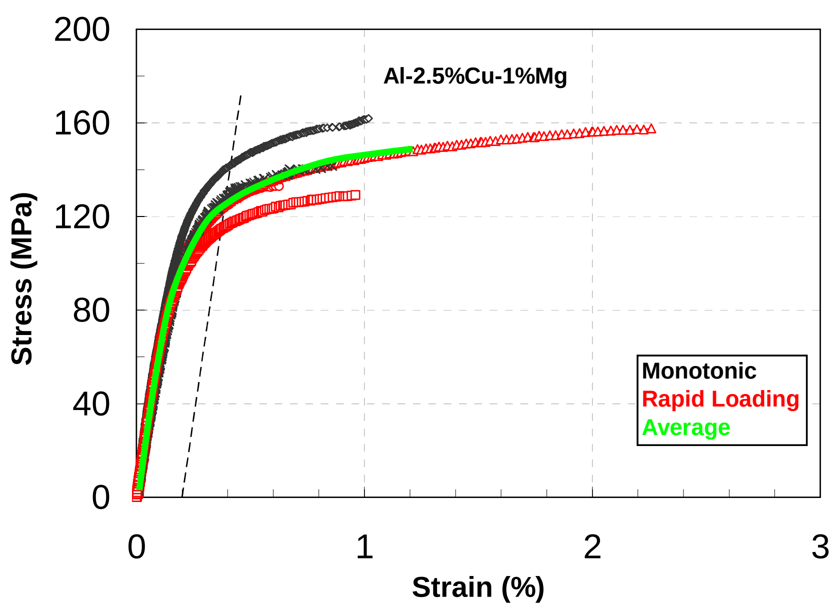

Fig. 4.29 Engineering stress vs strain of aluminum matrix with 2.5 wt.%Cu and 1 wt.%Mg

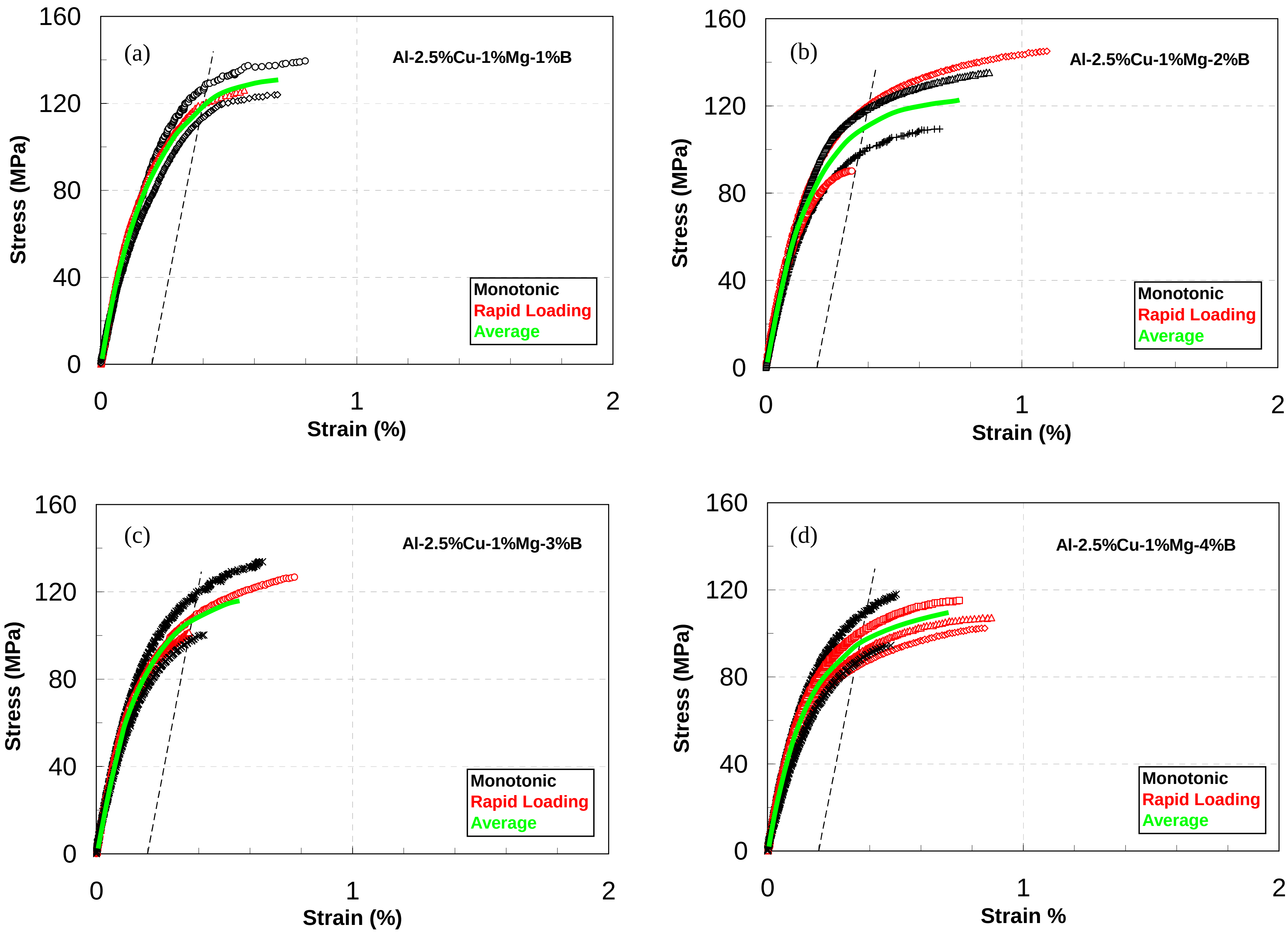

Fig. 4.30 Engineering stress vs strain curves of composites reinforced with AlB_2
(a) 1 wt.%B, (b) 2 wt.%B, (c) 3 wt.%B and (d) 4 wt.%B

Table 4.7 Tensile properties of Al-2.5wt.%Cu-1wt.%Mg based composites

Composite Al-2.5%Cu 1%Mg		Yield Strength* (MPa)	Ultimate Strength (MPa)	Strain Max Load (%)	Elasticity Modulus (GPa)
Matrix	max	142.82	161.92	2.25	66.67
	ave	128.41	144.67	1.14	
	min	115.05	129.14	0.62	
1wt.%B	max	129.21	139.49	0.79	63.64
	ave	120.68	129.85	0.68	
	min	112.89	123.98	0.56	
2wt.%B	max	120.95	145.05	1.09	63.1
	ave	107.03	121.47	0.77	
	min	90.06	90.14	0.34	
3wt.%B	max	120.7	133.7	0.77	61.57
	ave	107.4	115.53	0.55	
	min	97.47	100.23	0.36	
4wt.%B	max	110.58	117.97	0.88	60.29
	ave	95.23	107.33	0.69	
	min	84.62	94.04	0.48	

*Using offset at 0.2% of strain [63]

In Table 4.7, the maximum, the minimum as well as the average value of the tensile properties for each composite are presented. These values were useful to plan and set up the subsequent fatigue experimentations. Also a small decrease in the elasticity modulus for higher boron levels is apparent in the results from this table, while the variation in ductility was not consistent. For instance, samples with 1 and 3 wt.%B showed the lowest ductility, while samples with 4, 2 and 0 wt.%B showed highest values of deformation at maximum load. In addition, some samples had a early failure near to the yield stress calculated using the 0.2% offset method [63]. This was attributed to casting defects in those samples. Nevertheless, this was not corroborated because a fracture surface study was not part of the present dissertation.

4.5.1 Discussion

The dispersion observed in the tensile curves is the usual behavior of a composite material reinforced with dispersed particles. In some cases, the samples did not reach their maximum capacity, due to defects inherent to the fabrication process. Such dispersion allowed to indentify clear differences between samples with 1, 2 and 3 wt.%B.

All things considered, unreinforced samples showed a better behavior. This contradictory behavior was again attributed by the Mg-AlB_2 interaction, which was shown to affect other mechanical properties like the impact strength and the hardness of these composites. A similar behavior was reported by Lu, et al. in composites with a Mg9%Al alloy system as matrix [77]. In this case a composite reinforced with TiB_2 reveals the decrease in strength even compared to its matrix. The authors attributed the decrease in strength to a possible decomposition of the TiB_2 due to a predominantly reaction of B with Mg forming MgB, which was not proved in the mentioned work. On the other hand, this fact could be caused by an interaction Mg diboride forming a doped structure $Ti_{(1-x)}Mg_xB_2$ like the one observed in AlB_2 particles. In fact, the formation of TiB_2 doped structures has been studied before [76] and the interaction with the Mg would not be unexpected since MgB_2 has an extended solubility with AlB_2 and its share the same crystal structure.

For practical proposes the average values of tensile properties reported in Table 4.7 were used for the fatigue calculations in the next sections. However, for design purposes the minimum values of the tensile properties could be used for safety. In general, the yield strength range of these composites appears to be low compared to results from similar composites reported before [70, 78]. However, the strength of these materials can be improved by precipitation hardening and/or mechanical deformation treatments [4].

4.6 Fatigue Crack Growth

The fatigue results are presented separately for the gravity and centrifugal casting specimen. To determine the maximum bending load for each composite and the corresponding levels of loading for the fatigue tests, monotonic bending tests were conducted and are summarized in the same section.

4.6.1 Maximum Bending Load

The monotonic bending results of both gravity and centrifugal casting samples showed a decrement in maximum load capacity with the weight percent of boron, as illustrated in Fig. 4.31. In this figure, the samples obtained by centrifugal casting (black datapoints), bear higher loads than those samples obtained via gravity casting (red datapoints).

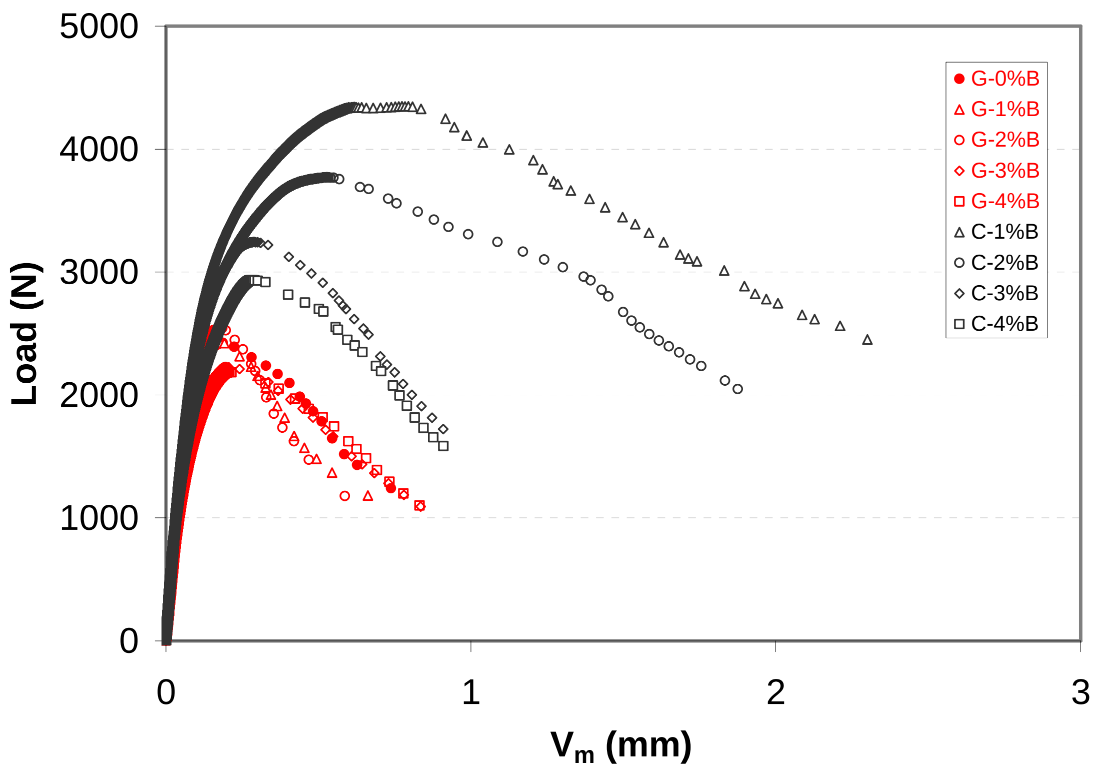

Fig. 4.31 Load vs crack mouth opening displacement measured at the location of the integral knife edges

There is a larger variation of the maximum load with respect to the percent of boron and the processing features. For instance, the maximum load corresponding to the base material (0 wt.%B) was around 2500 N. This value was used as a benchmark to define the fatigue load range for all composites. Thus, for 80, 70, 60 and 50 % of maximum load, the corresponding fatigue load selected were 2000, 1750, 1500 and 1250 N respectively.

4.6.2 *Effect of K_{max}*

With different maximum load conditions it was important to evaluate whether the variations in the load ratios had any effect on the fatigue crack growth of the composites. In aluminum alloys, the aforementioned load ratio effect commonly influence the crack closure phenomenon, which was described in section 2.6. Such phenomenon has been studied by several researchers and different modifications of the Paris equation have been proposed to take it into account.

Although the Elber's model and the adjusted compliance ratio (ACR) approach proposed by Donald [50, 51] are widely used as well as the partial crack closure model proposed by Paris [52] and other models, the discussion over crack closure effect is still open. Furthermore, models that do not use disputable fatigue crack closure data have also been proposed, e.g. Kujawsky [48] and Walker [53] models, equations 2.13 and 2.14 respectively. These models assume that the crack growth is principally affected by ΔK and Kmax, responsible of cyclic damage and monotonic damage contribution respectively [79, 80].

In particular, Kujawsky obtained fairly good results when using $(\Delta K^{+}\cdot Kmax)^{0.5}$ as the driving force for crack growth [48]. In addition, a variation of these two-parameter approach was presented by Dinda and Kujawsky, where a correlation parameter α was introduced, leaving the equation for K^* very similar to the Walker approach, showed in equation 2.14. However, the model of equation 2.13 presented by Kujawsky for ΔK^* was implemented in this dissertation due to its simplicity and good correlation with the R-ratio effect shown before [48]. For sake of comparison, the crack growth curves obtained using ΔK and ΔK^* for an aluminum alloy containing 2.5 wt.%Cu and 1 wt.%Mg (without reinforcements) are shown in Fig. 4.32a and Fig. 4.32b.

There are not significant differences between curves obtained using the ΔK and ΔK^* approaches shown in figure Fig. 4.32. Only a small shifting to the right in curves using ΔK^* is observed. This displacement of the curves is mainly due to the contribution of K_{max} in the arithmetic mean. Although this approach has been proved to collapse the data from different R-ratios, in this work the collapse of the curves is not ensured. This is because in the curves of Fig. 4.32 the change in R-ratio is influenced only by variations in the maximum fatigue load. In other words, the model would be more effective if changes in the minimum fatigue load were also influencing the R-ratio variation.

In addition, the curves separation in Fig. 4.32 reveals an effect of the maximum load (monotonic damage) on the crack growth behavior of the aluminum alloy (base material) obtained via gravity casting. The separation between curves was also observed in composite samples reinforced with AlB_2 and obtained via gravity casting, as illustrated in Fig. 4.33.

Conversely, such phenomenon was not observed in the crack growth curves of centrifugally cast composite (Fig. 4.34).

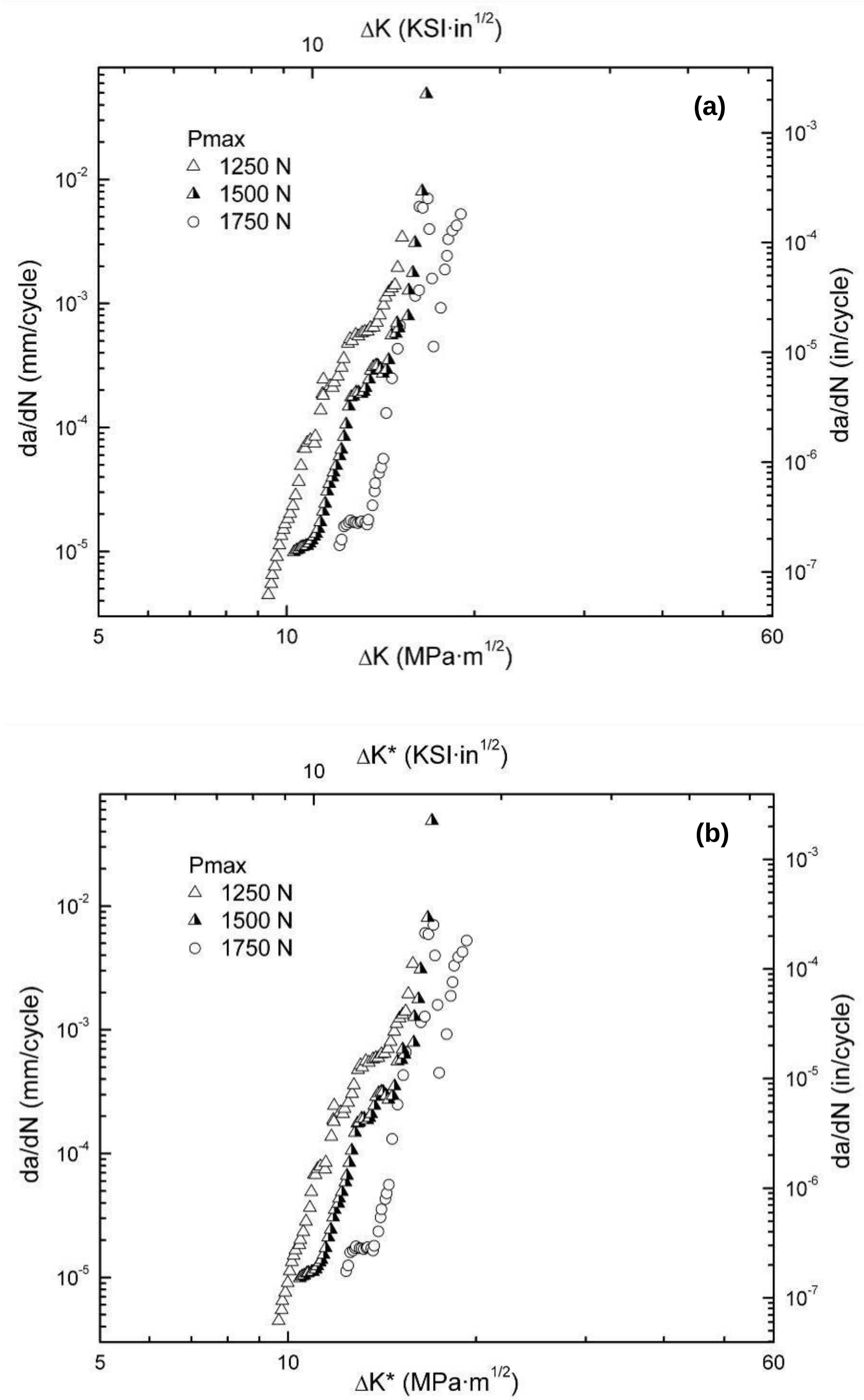

Fig. 4.32 Crack growth curves of Al-matrix containing 2.5wt.%Cu and 1wt.%Mg obtained by gravity casting a) Using applied ΔK and b) Employing the ΔK* approach proposed by Kujawsky

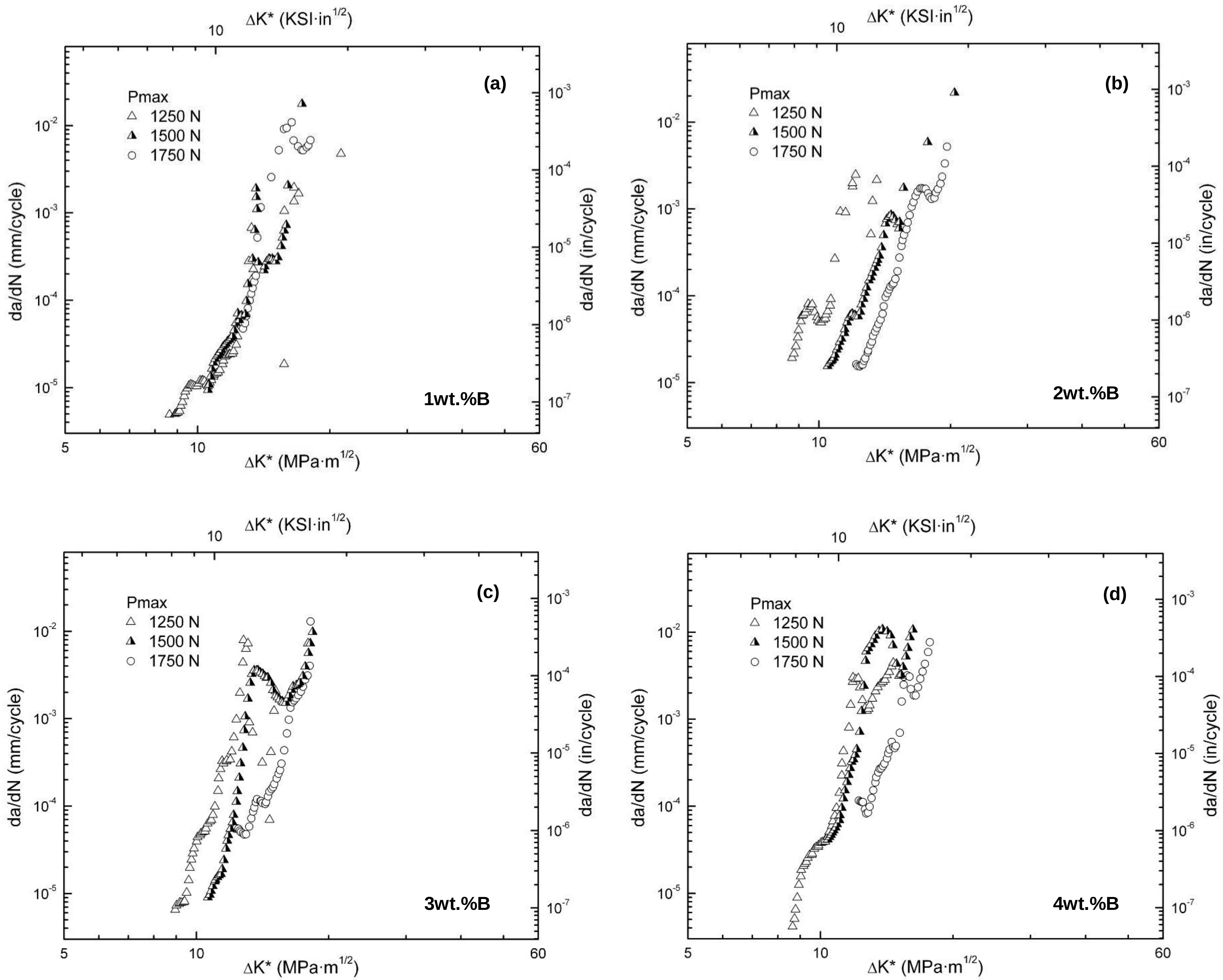

Fig. 4.33 Crack growth curves of AMC's obtained via gravity casting, containing 2.5wt.%Cu and 1wt.%Mg; and reinforced with different wt.% of boron a) 1wt.%B, b) 2wt.%B, c) 3wt.%B and d) 4wt.%B.

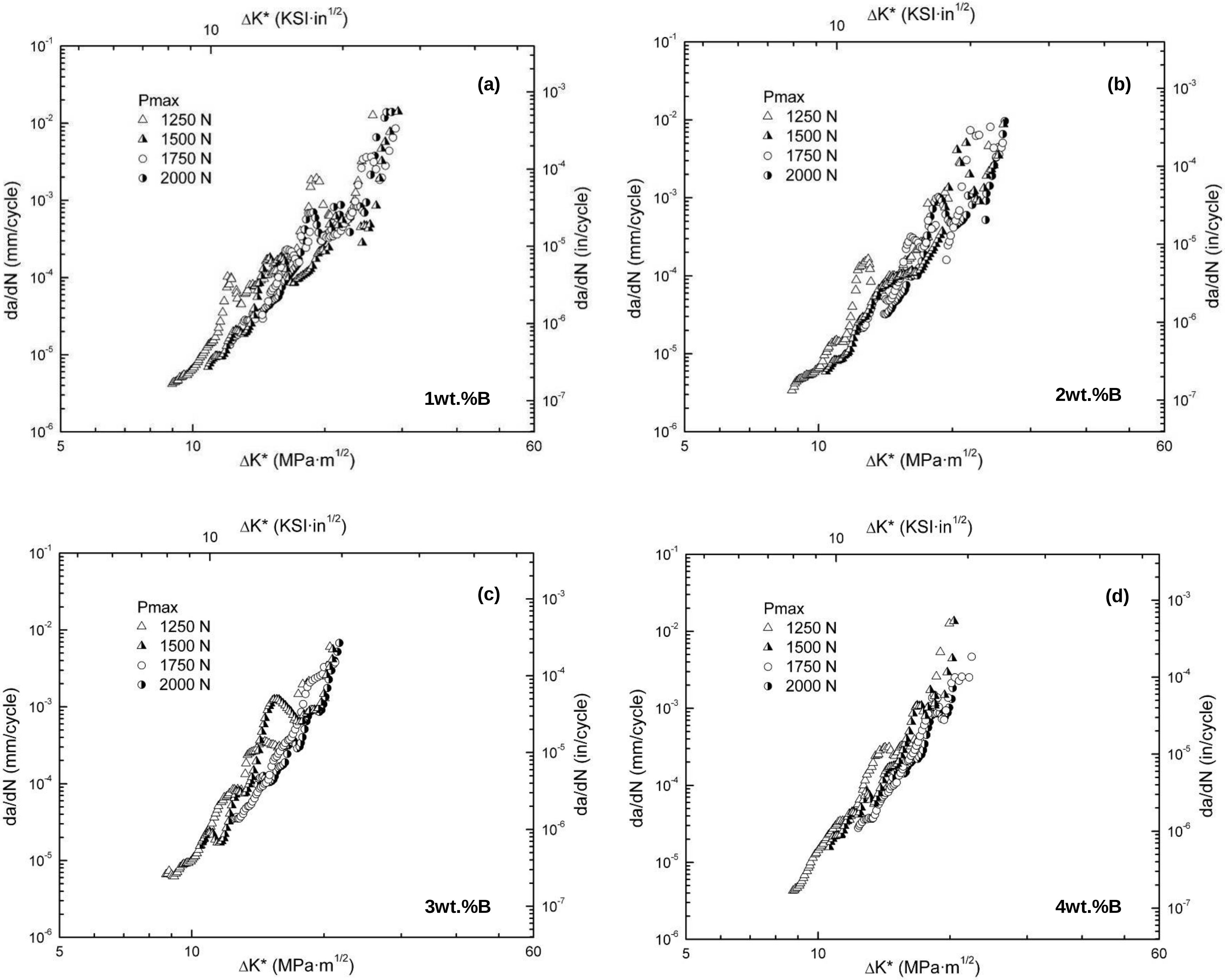

Fig. 4.34 Crack growth curves of AMC's obtained via centrifugal casting, containing 2.5wt.%Cu and 1wt.%Mg; and reinforced with different wt.% of boron a) 1wt.%B, b) 2wt.%B, c) 3wt.%B and d) 4wt.%B

In other words, since all samples were tested under the same conditions, the levels of maximum fatigue load employed demonstrated a larger effect on the gravity cast composites than on centrifugally cast ones.

In fact, since gravity cast samples showed lower levels of maximum bending loads than centrifugal casting samples in Fig. 4.31, the maximum fatigue loads employed have a higher effect on those samples. Moreover, curves of centrifugally cast samples showed to collapse (converge), as illustrated in Fig. 4.34. However, some events of crack growth rate changing are observed in both Fig. 4.33 and Fig. 4.34.

These crack growth acceleration/deceleration events could be influenced by the presence of casting defects, crack branching or uneven particle clusters distribution, which results in variations in the crack path and morphology. For this reason, the analyses of such events will be treated in the fracture analysis section.

In general, the fatigue crack growth curves of centrifugally cast samples showed lower slopes and capacity to support higher stress intensity factors (SIF). In other words, these samples possessed higher fatigue strength. Such difference in the response of these two types of composites can be explained by differences in the microstructure produced by both casting processes. For instance, the molten metal is submitted to high acceleration (48 g) during the centrifugal casting, which produces a reduction of the casting defects compared with gravity casting samples, which is also assisted by gradual variation of the particle volume fraction in the direction of the centrifugal acceleration.

4.6.3 Effect of Boron Level

Since one of the principal goals of this dissertation has been to identify how crack growth varies as a function of the weight percent of boron present in the material, in this section the crack growth curves are plotted as function of the wt.%B, as illustrated in Fig. 4.35 and Fig. 4.36. These figures shown the results of the samples obtained through gravity casting and centrifugal casting respectively.

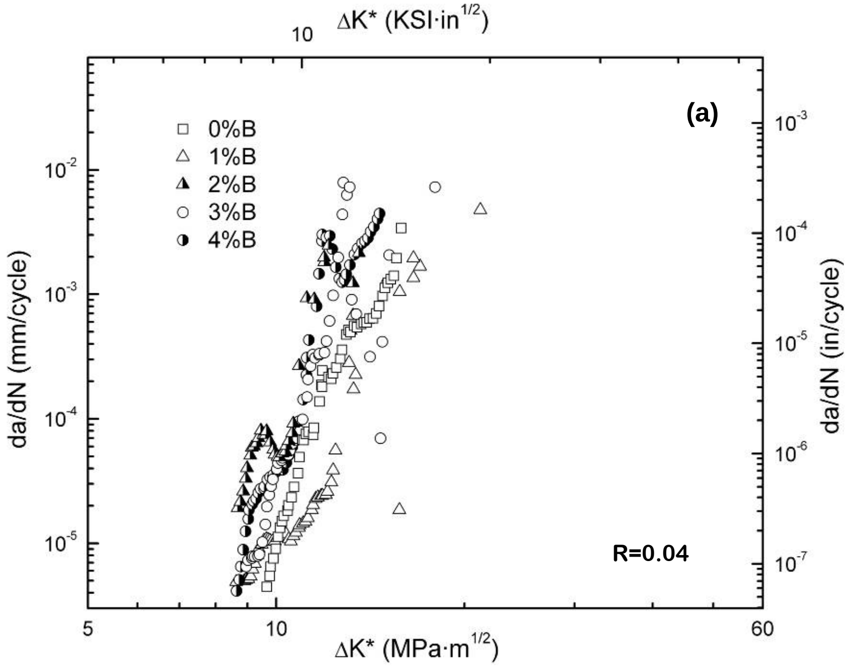

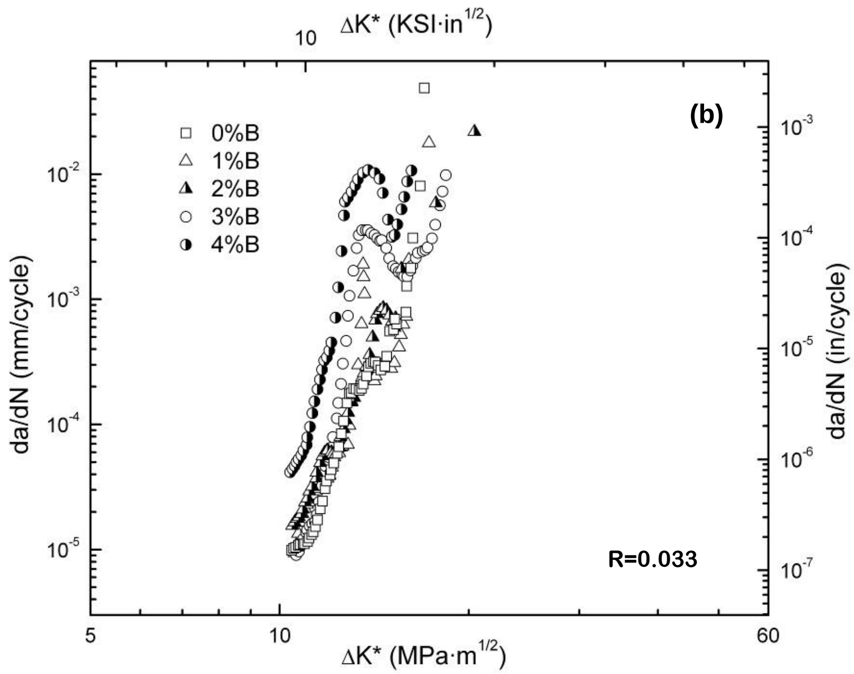

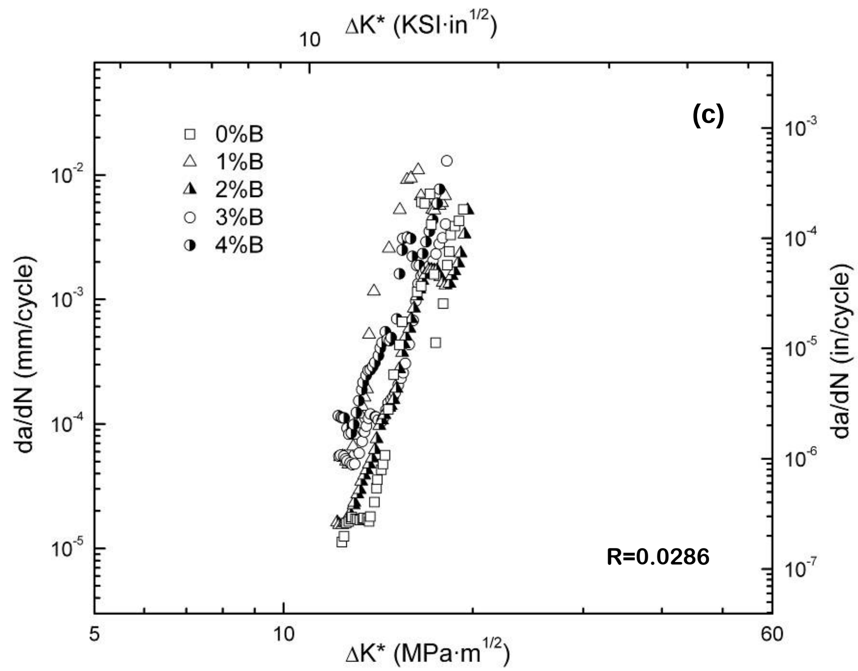

Fig. 4.35 Effect of boron weight percent on the da/dN vs ΔK curves of composites obtained via gravity casting for different load ratios (Min load of 50N). a) R=0.04 (Max. 1250 N), b) R=0.033 (Max. 1500 N) and c) R=0.02857 (Max. 1750 N).

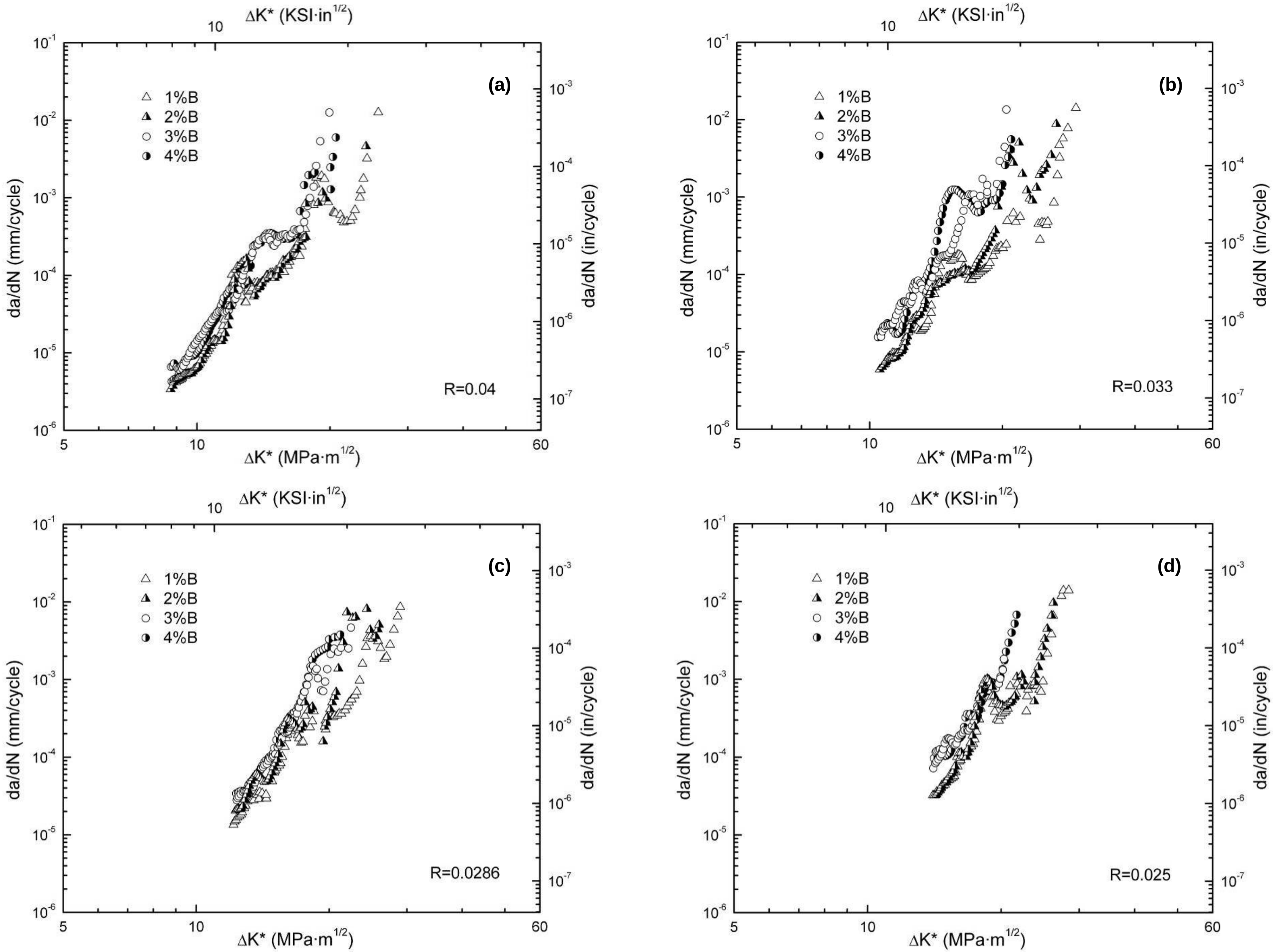

Fig. 4.36 Effect of boron weight percent on the da/dN vs ΔK curves of composites obtained via centrifugal casting for different load ratios (Min load of 50N). a) R=0.04 (Max. 1250 N), b) R=0.033 (Max. 1500 N), c) R=0.02857 (Max. 1750 N) and d) R=0.025 (Max. 2000 N)

Centrifugally cast samples were tested at maximum load conditions of 1250 N, 1500 N, 1750 N and 2000 N, as shown in Fig. 4.36a, b, c and d respectively. The test corresponding to 2000 N is not shown in Fig. 4.35, because some gravity cast samples showed very short fatigue life when tested at such conditions and the calculation of the fatigue crack growth curve was no possible.

In general, in both gravity casting and centrifugally casting samples, the first part of the curves are displaced to the right as the maximum testing load increases. This is also a consequence of monotonic damage associated with the increment of the maximum testing load and corroborates the observations conducted in the previous section.

Moreover, although there are not large differences between curves due to the weight percent of boron, in both gravity and centrifugal casting samples, the curves can be separated in two groups. The first one corresponds to samples containing 1 and 2 wt.%B with similar behavior, which showed the highest SIF and the second includes the samples containing 3 and 4 wt.%B, which appears shifted to the left in the charts, showing lower SIF and reflecting a shortening of the fatigue life of those samples.

In order to further study the effect of boron levels on the crack growth of this series of composites, the research was focused in obtaining and comparing the slope of the da/dN vs ΔK^* of each composite. This is a measure of the fatigue crack growth resistance of the material assumes that the stress intensity factor concept can still be used to study the fracture behavior of AMCs reinforced with ceramic particles and FGMs. Such assumption was also employed by Xu et al. [39] to study the crack growth behavior of graded and homogeneous SiC_p reinforced Al composite.

The slope of the crack growth curve for each condition could have been obtained via simple linear regression. However, the presence of events of acceleration/deceleration in the crack growth of some samples would have affected the calculation of the slope. Therefore, it was decided to use the robust fit function, a MatLab® tool that employs robust statistic to obtain a linear fit, where less weight is assigned to outliers or data that can cause unexpected deviation with respect to the majority of sample data. This reduces the effect of data segments with events of acceleration/deceleration of crack growth on the slope calculation. Detailed information about the use of the Robust Fit function was included in the appendix X.1.

Once the slope for each sample was computed, the data from gravity and centrifugally cast samples were plotted separately in Fig. 4.37 and Fig. 4.38 respectively. In these figures an almost linear increment of the slope as a function of the boron level is evident in the 1 to 4 wt.%B range. This increment in the slope translates in a reduction of the fatigue strength as the wt.%B increases in this kind of composites. This agrees with the results obtained from impact and tensile tests, where the Mg-AlB_2 interaction was shown to reduce the material strength.

Nevertheless, the slopes obtained for the matrix (0 wt.%B i.e. unreinforced alloy) shows to be higher than the slopes obtained in samples containing only 1 wt.%B, as illustrated in Fig. 4.37. This contradiction could be explained by the combination of two phenomena. The first one is associated with direct and indirect strengthening mechanisms involved in the particle reinforcement of an aluminum matrix, a topic treated in section 2.4, and the second one relates to the material strength reduction promoted by the Mg-AlB_2 interaction, phenomenon studied in section 4.4.

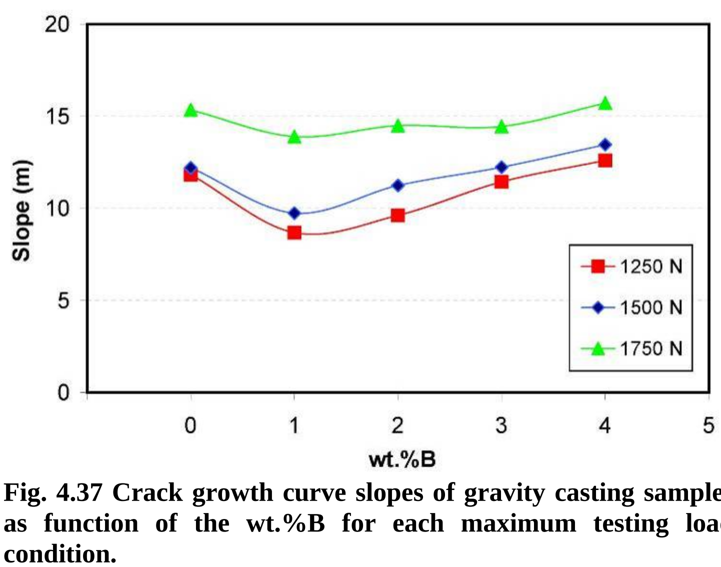

Fig. 4.37 Crack growth curve slopes of gravity casting samples as function of the wt.%B for each maximum testing load condition.

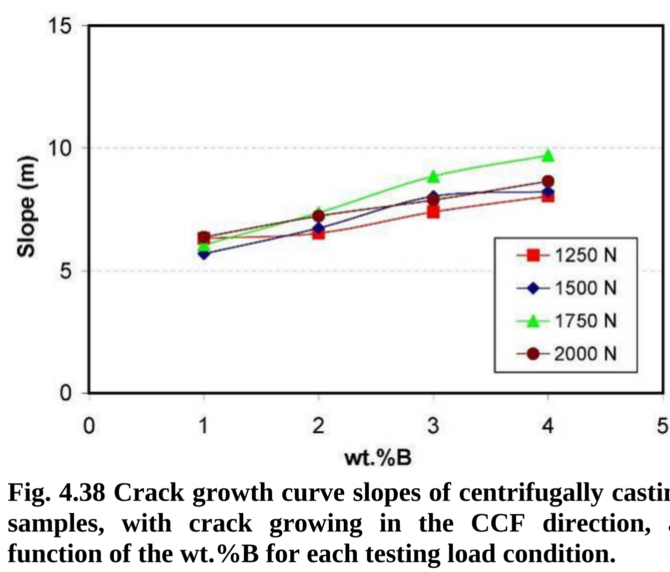

Fig. 4.38 Crack growth curve slopes of centrifugally casting samples, with crack growing in the CCF direction, as function of the wt.%B for each testing load condition.

As a consequence for lower particle loadings, for example 1 and 2 wt.%B (group 1), the crack growth curve slope would be influenced mainly by the strengthening mechanisms, promoting a reduction in the slope or the increases in the fatigue resistance; which is the usual effect of particle reinforcing. On the other hand, for 3 and 4 wt.%B (group 2) the slope values is more affected by the Mg-AlB_2 interaction. With these levels of boron, the higher quantity of particles results in a higher contact area of particles, increasing the detrimental effect of the aforementioned interaction.

Fig. 4.37 reveals the effect of the monotonic damage in the gravity cast samples. In this figure, the slope values increase with the maximum testing load and, again, the results from the FGMs plotted in Fig. 4.38 do not show a clear effect of the monotonic damage by increasing the maximum testing load. Therefore, the slope for samples with the same level of boron in this figure could be used as replicates to obtain a regression model for the crack growth curve slope as function of the wt.%B, as illustrated in Fig. 4.39. On the other hand, for data of gravity casting samples in Fig. 4.37, regressions of each testing condition, in the range from 1 to 4 wt.%B were obtained and are presented in Table 4.8.

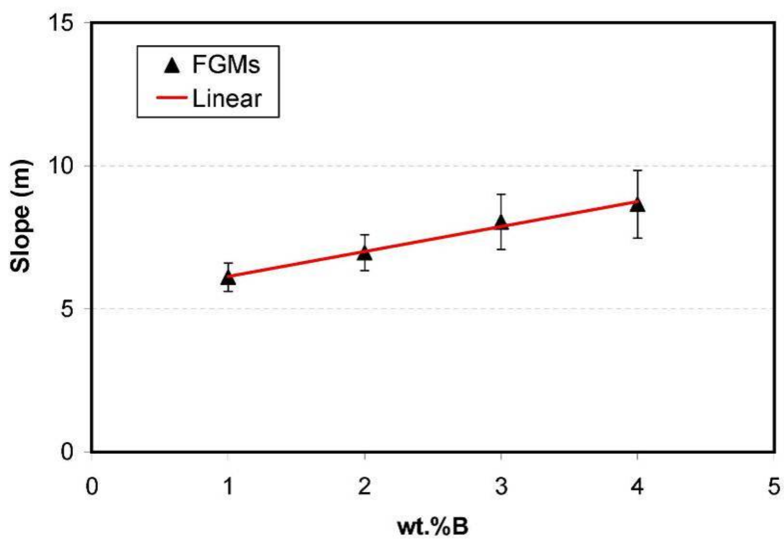

Fig. 4.39 Linear regression of data in Fig. 4.38.

Table 4.8 summarize the regression parameters fitting a model of the form

$$Slope\ (m) = X_1 \cdot (wt.\%B) + X_2 \quad \textbf{(4-2)}$$

Table 4.8 Linear regression parameters for each condition.

Casting Method	Max Fatigue Load (N)	X_1	X_2	R^2
Gravity	1250	1.3591	7.194	0.986
	1500	1.2114	8.637	0.994
	1750	0.5382	13.297	0.827
Centrifugal	All	0.8722	5.260	0.990

The last row in the table corresponds to the linear regression of FGMs data in Fig. 4.38. It is important to emphasize that the high R-squared values obtained corroborate the linear variation of the crack growth curve slope with the wt.%B.

4.6.4 Effect of Loading Rate

All tests were performed under high loading rates. However, to identify the loading rate effect on the fatigue crack growth, the results from two loading rates were compared (15 and 20 KN/s respectively) at 1500 N of maximum fatigue load.

Again the results from samples obtained via gravity and centrifugal casting are presented separately in Fig. 4.40 and Fig. 4.41. For comparative proposes Fig. 4.35b and Fig. 4.36b corresponding to samples tested at maximum fatigue load of 1500 are presented again as Fig. 4.40a and Fig. 4.41a respectively. Despite the some small differences in the crack growth curves obtained by using loading rates of 15 and 20 KN/s, the slope analyses showed that there is not a clear effect of the loading rate on centrifugally cast samples, as illustrated in Fig. 4.43. Conversely, an evident effect of the loading rate on gravity casted samples is observed in Fig. 4.42. Samples tested at 20 KN/s exhibit lower crack growth slopes than those tested using 15 KN/s, with exception of the samples containing 1 wt.%B, which showed very similar values. This discrepancy in the response of these two kinds of composites could be related to level of fatigue load utilized. Since gravity casting samples showed lower strength than the FGMs in Fig. 4.31, crack growth rates of gravity cast samples would be more susceptible to the loading rate.

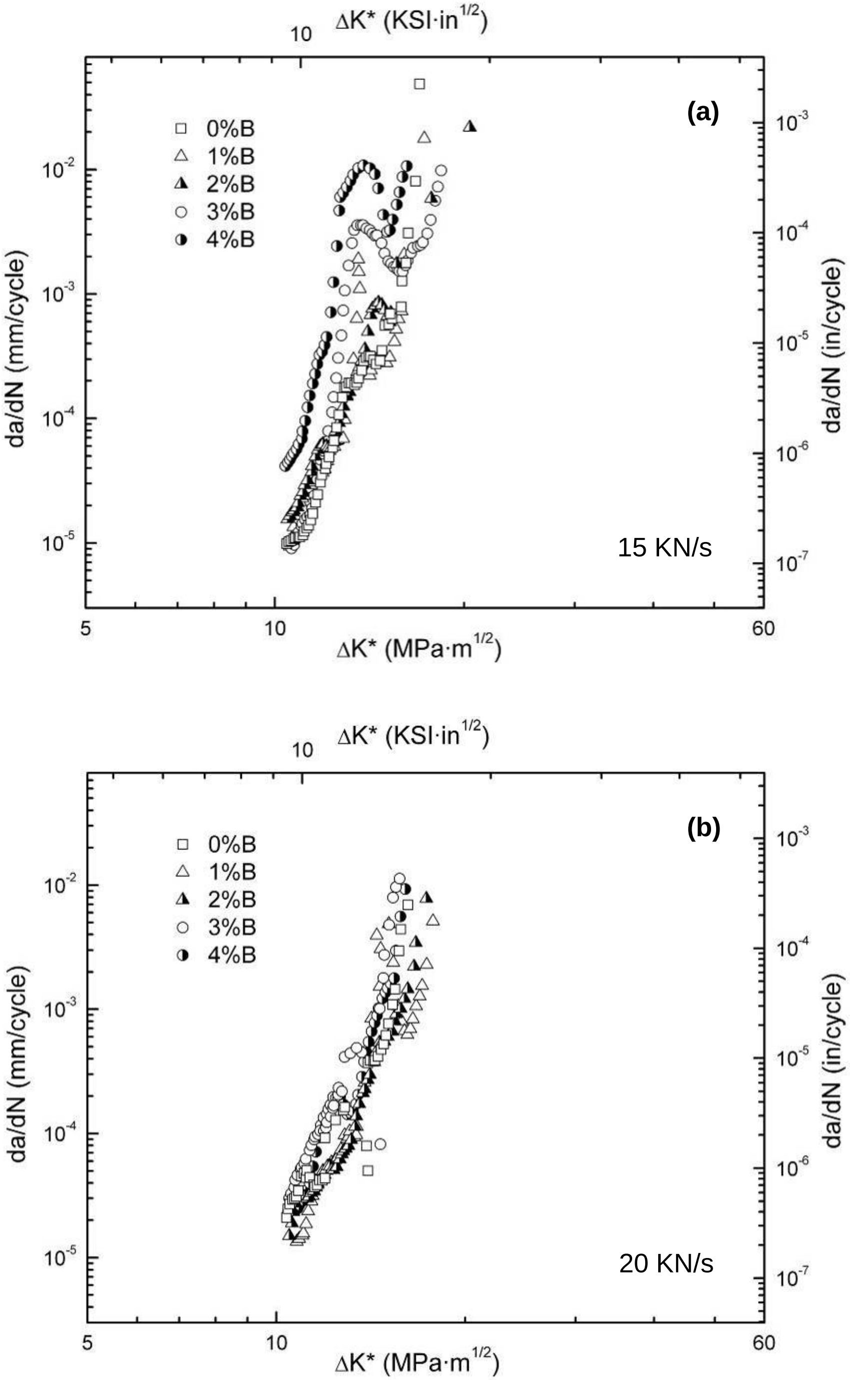

Fig. 4.40 Crack growth curves of gravity casted samples tested at maximum load of 1500 N and R=0.033, a) Loading rate of 15 KN/s, b) Loading rate of 20 KN/s.

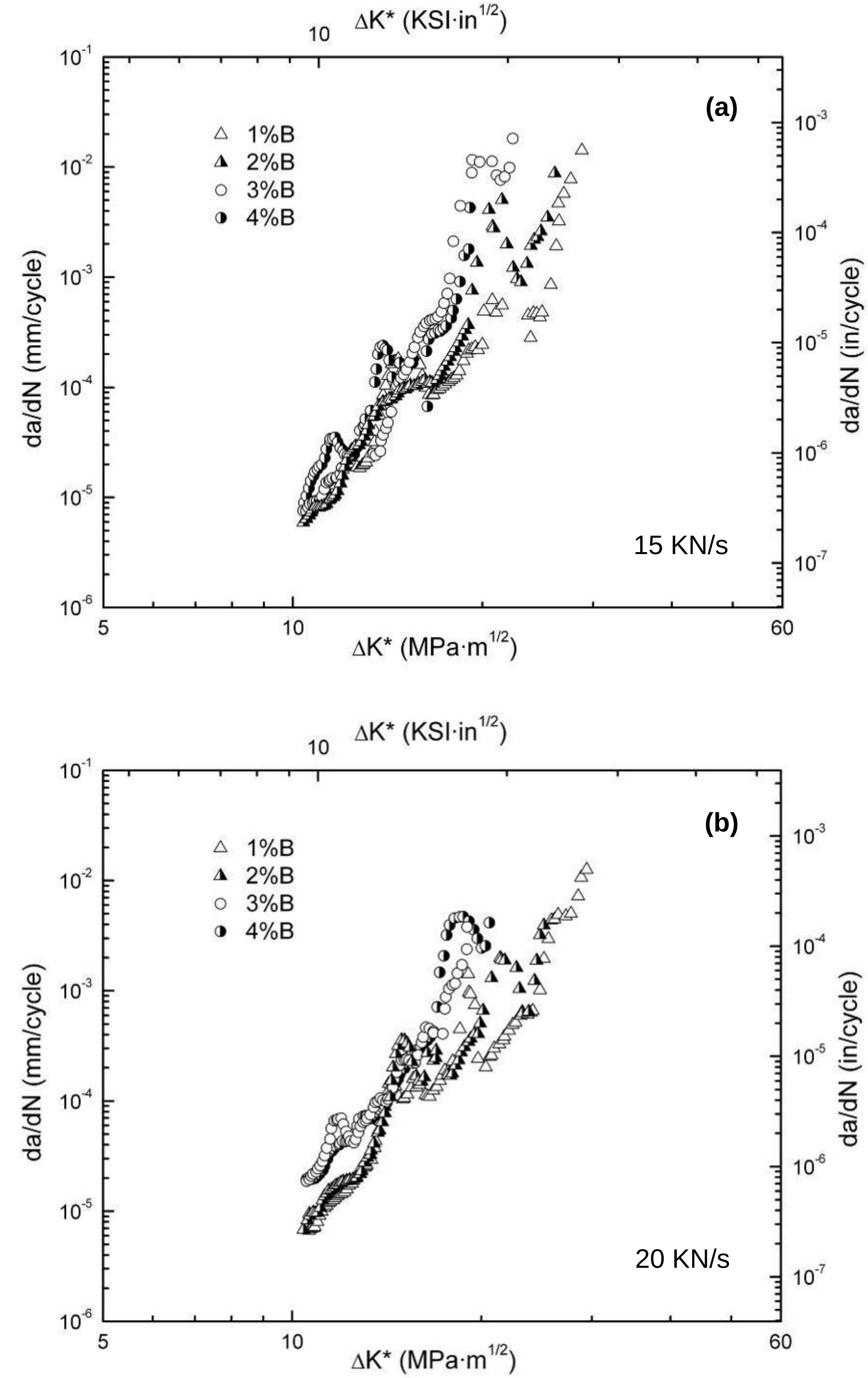

Fig. 4.41 Crack growth curves of centrifugally casted samples tested at maximum load of 1500 N and R=0.033, a) Loading rate of 15 KN/s, b) 20 KN/s.

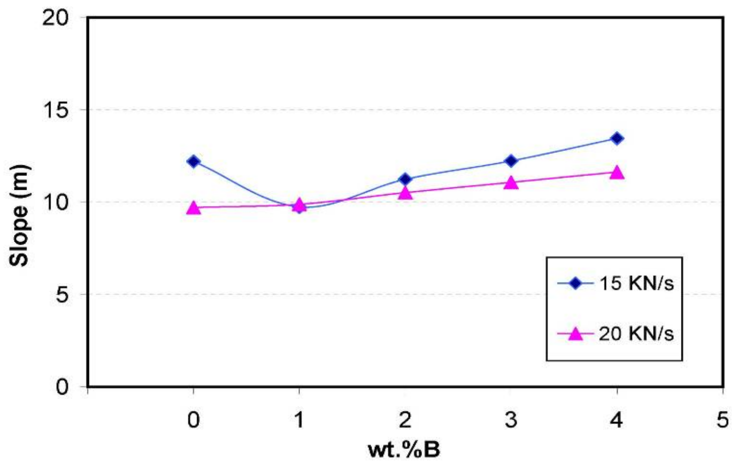

Fig. 4.42 Crack growth curve slopes of gravity casted samples for two loading rates (15 and 20 KN/s). Samples tested at maximum load of 1500 N and R=0.033.

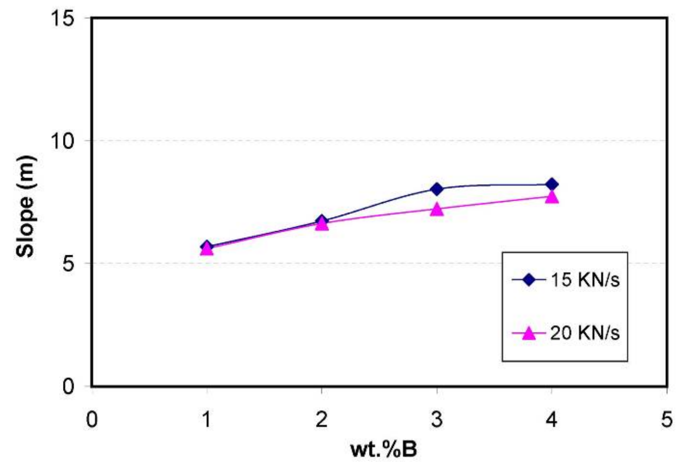

Fig. 4.43 Crack growth curve slopes of centrifugal casting samples, with crack growing in the CCF direction, for two loading rates (15 and 20 KN/s). Samples tested at maximum load of 1500 N and R=0.033.

In this respect, Buršák and Mamuzić who studied the effect of loading rate in drawing steel sheet, concluded that increasing the strain rate up to the critical value, the resistance of the material against plastic strain also increases [81]. Therefore, since gravity samples have exhibited lower strength than FGMs, these samples would reach larger areas of plasticity nearby the crack process zone, forcing these materials to be more sensitive to the loading rate. Nevertheless, the tensile results of gravity cast samples do not show to be affected by the loading rate, which lead to an apparent contradiction.

However, the small effect of the loading rate observed in Fig. 4.42 could have been unnoticed in the tensile testing results of section 4.5. Since fatigue crack growth is highly depending of the plastic strain field ahead of the crack tip, the fatigue crack growth would be more sensitive to be affected by the loading rate.

4.6.5 Effect of Particles Distribution on Functionally Graded Composites

To analyze the effect of the particle distribution on a specimen cross section on the crack growth of the FGMs, results from tests with the crack growing in opposite directions were studied. For instance in Fig. 4.44a and Fig. 4.44b the crack growth curves for different boron levels are presented with the crack growing opposed to the centrifugal force direction (CCF direction) and in the centrifugal force direction (CF direction) respectively. It is important to clarify that the results presented in the previous section correspond to samples tested with crack growing in the CCF direction or through the section with lower particles density.

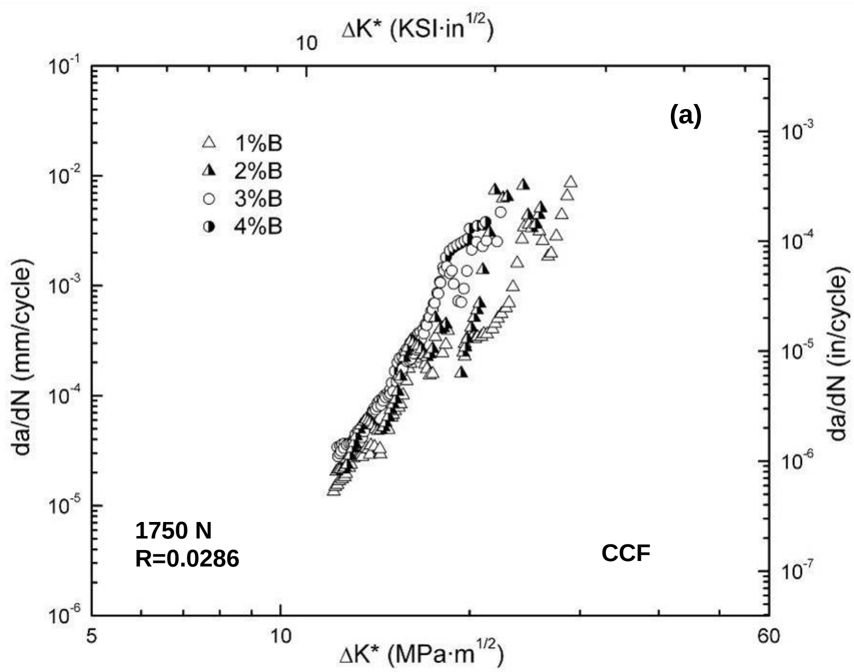

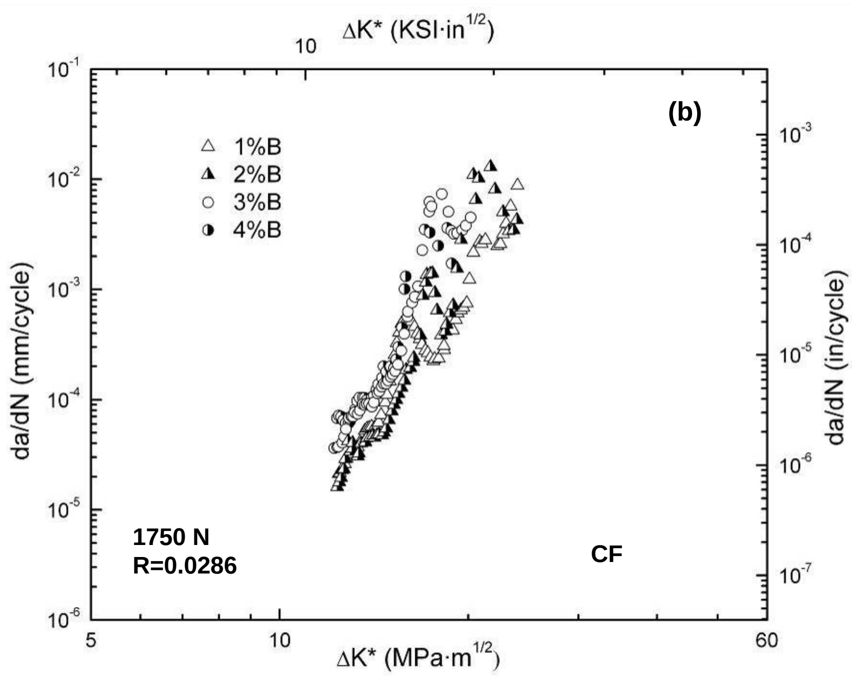

Fig. 4.44 Crack growth curves of FGMs tested at maximum load of 1750 N and R=0.0286, with crack growing in: a) CCF direction and b) CF direction.

The results in Fig. 4.44 do not show significant differences between specimens. However, when the slopes of the crack growth curves in Fig. 4.44a and Fig. 4.44b are compared, the samples tested in the CCF direction show lower slopes values, as illustrated in Fig. 4.45, where the crack growth slopes of samples tested in both direction are presented.

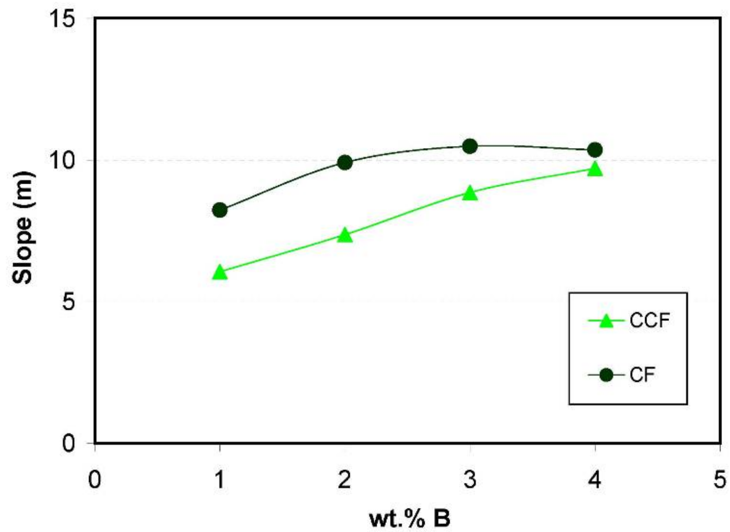

Fig. 4.45 Crack growth curve slopes as function of the wt.%B for two crack growth directions.

The results in this figure agree with the effect of the weight percent of boron presented in section 4.6.3, where the slopes of the da/dN vs ΔK* curve increased as the wt.%B increased. In this section, when the samples are tested in the CF direction, the crack growths from an area close to the center of the cross section to the edge with higher density of particles. Thus, as the crack grows the amount of particles near to the crack tip process zone increases. This means that the growing crack encounters regions with increasing particle volume percent. Therefore, the analyses of the section 4.6.3 would be valid to explain the variation in the crack growth due to the particle distribution in the FGMs.

4.7 Fracture Analysis

The fracture study was conducted on fatigue tested samples by means of optical microscopy. Additionally, crack path features were observed using both secondary electrons backscattered electron imaging to qualitatively determine fracture patterns and the location of the composites phases with respect to the crack path.

4.7.1 Optical Microscopy of the Crack Path

After analyzing the crack path of several samples, some micrographs were selected to illustrate the fracture characteristics of this series composite. For example, in Fig. 4.46 where the crack grew from left to right, the presence of intergranular fracture (IG) in the composites containing 1 wt.%B can be observed. This low energy form of fracture was present in both gravity and centrifugally cast samples (Fig. 4.46a and Fig. 4.46b respectively). As depicted in these figures, the separation of coarse grains leads to an irregular crack path, which results in a fracture surface with high roughness.

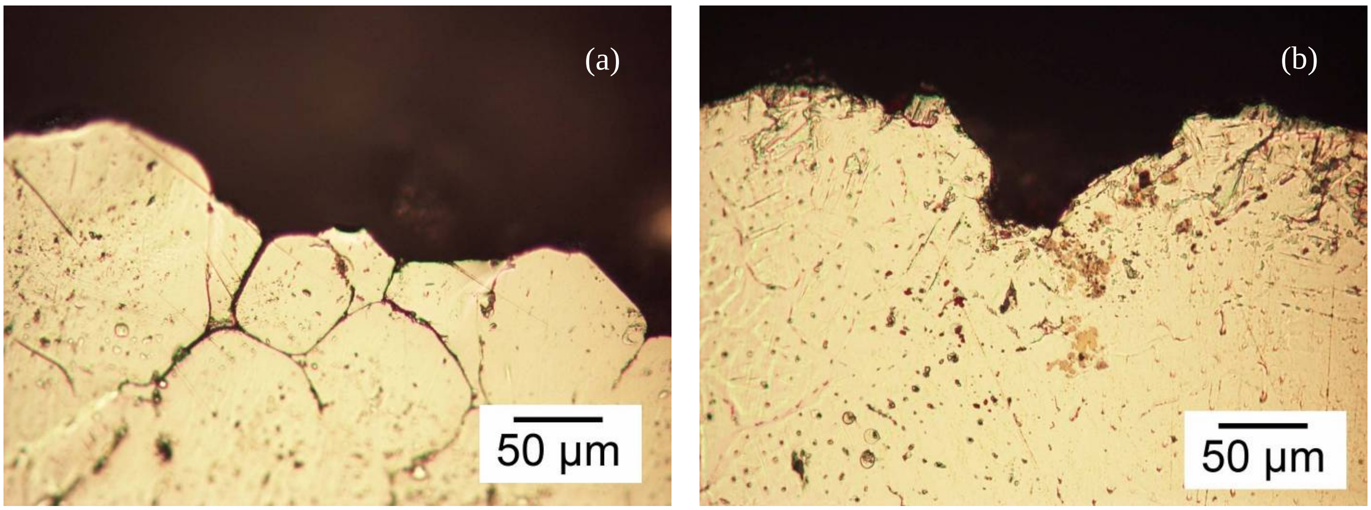

Fig. 4.46 Intergranular fracture in composites containing 1 wt.%B
a) Gravity casting, tested at R=0.04, b) Centrifugal casting, tested at R=0.033.

In addition, crack branching, which is a typical characteristic of the crack growth in particle reinforced composites, was also observed, as shown in Fig. 4.47. Crack branching and bridging features due to particle debonding are results of crack deflection and where believed to enhance the fatigue resistance of casting aluminum alloys [38, 39]. Fracture of coarse particles was also detected in some samples, where the crack grew through clusters of particles, as presented in Fig. 4.48. In this figure the particle fracture seems to promote branching of the crack path at load ratios as low as R=0.02857. In the literature the particle breaking have been associated with fatigue with high load ratios, for example R=0.8 [31]. However, since in this case the rupture of particles occurs at low load ratios, such phenomena could be consequence of monotonic damage associated to stress concentrations in free defects zones with particle clusters.

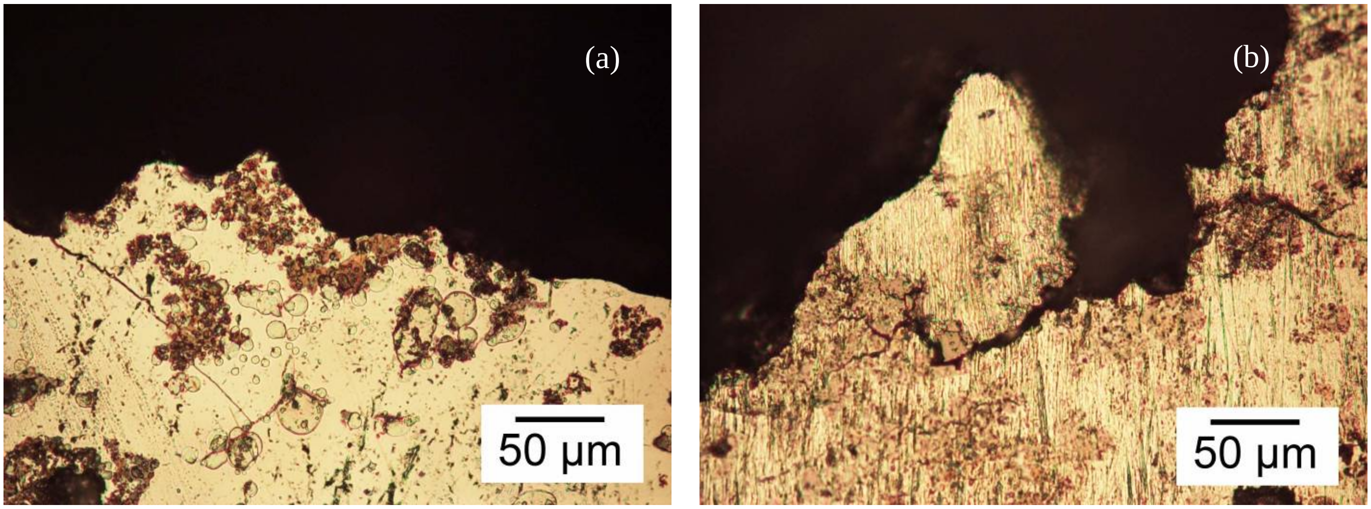

Fig. 4.47 Evidence of crack branching associated with the particle reinforcement in samples tested at R=0.02857. a) Gravity casting, 2 wt.%B, b) Centrifugal casting, 3 wt.%B.

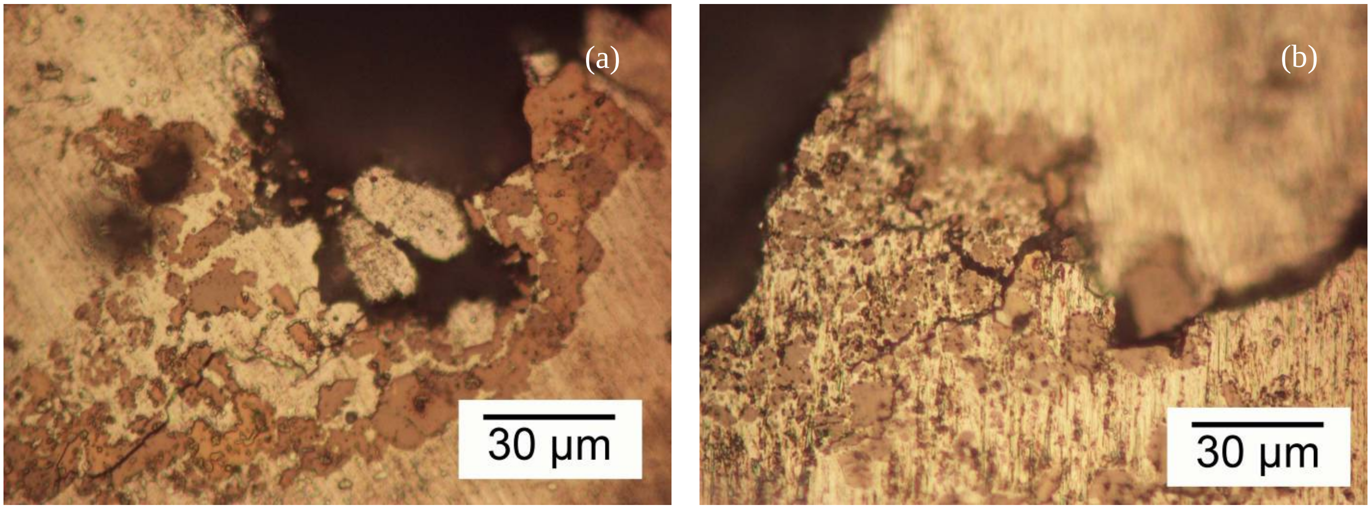

Fig. 4.48 Particles breaking when crack growth trough clusters in samples tested at R=0.02857. a) Centrifugal casting, 2 wt.%B, b) Gravity casting, 3 wt.%B.

Other pattern in the crack growth of this series of composites is the failure or separation of clusters, as showed in Fig. 4.49. This represented the largest deflection of the crack path observed, promoting higher roughness in the fracture surface. The separation of clusters was associated to defects surrounding the cluster structure. Such defects are inherented from the cast Al-B master alloys and are the result of air entrapment during the alloy fabrication. These defects were observed in gravity samples and in a small degree in centrifugally cast samples, as in Fig. 4.50a.

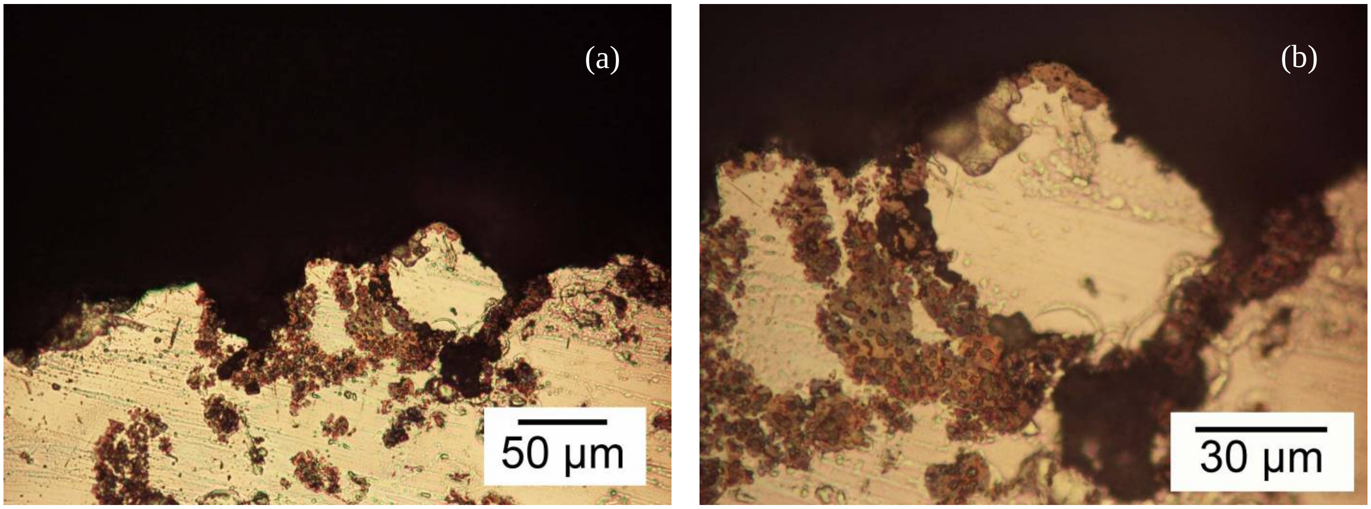

Fig. 4.49 Failure of clusters allow increasing the roughness in gravity casted composites containing 4 wt.%B. a) Appearance of the crack path, R=0.033, b) Close up of cluster separation in a.

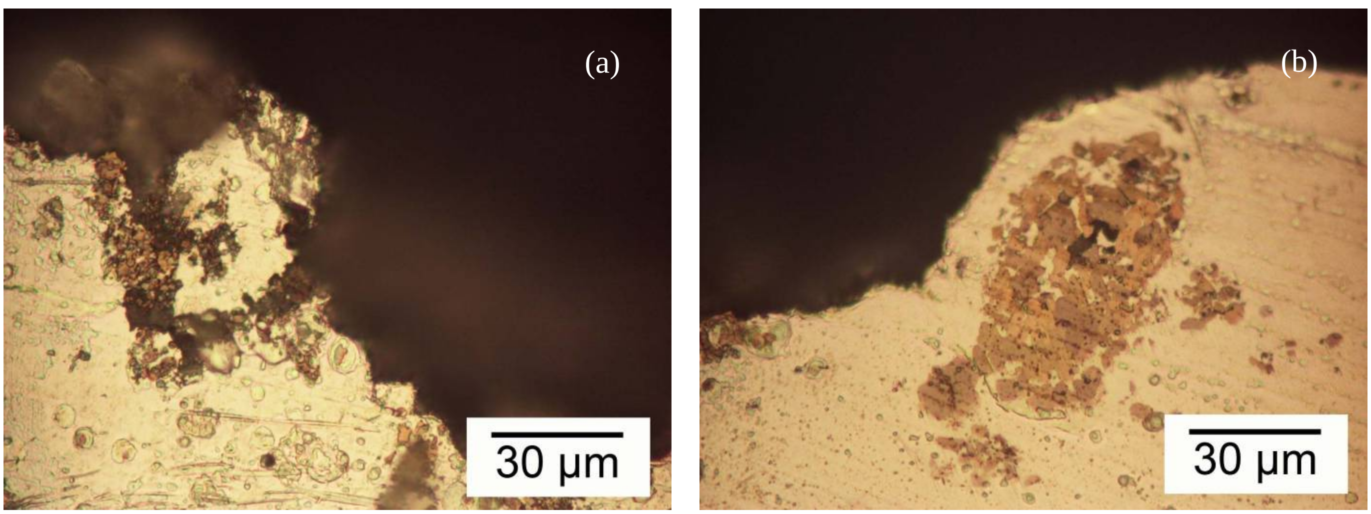

Fig. 4.50 Fracture of zones with particle clusters in FGMs containing 4 at.%B, tested at R=0.02857. a) Sample exhibiting cluster separation, b) Crack bordering a cluster almost free of defects.

On the other hand, when the particle clusters appears free of defects, they do not separate from the matrix, letting the crack grow enveloping the cluster, as shown in Fig. 4.50b. However, even tough the clusters do not fail from defects, it also could cause crack deflection, promoting more roughness in the fractured surface. Another form of failure of the defect free clusters is particle breaking (Fig. 4.48), which was observed in the crack path of a FGM containing 4 wt.%B, as illustrated in Fig. 4.51.

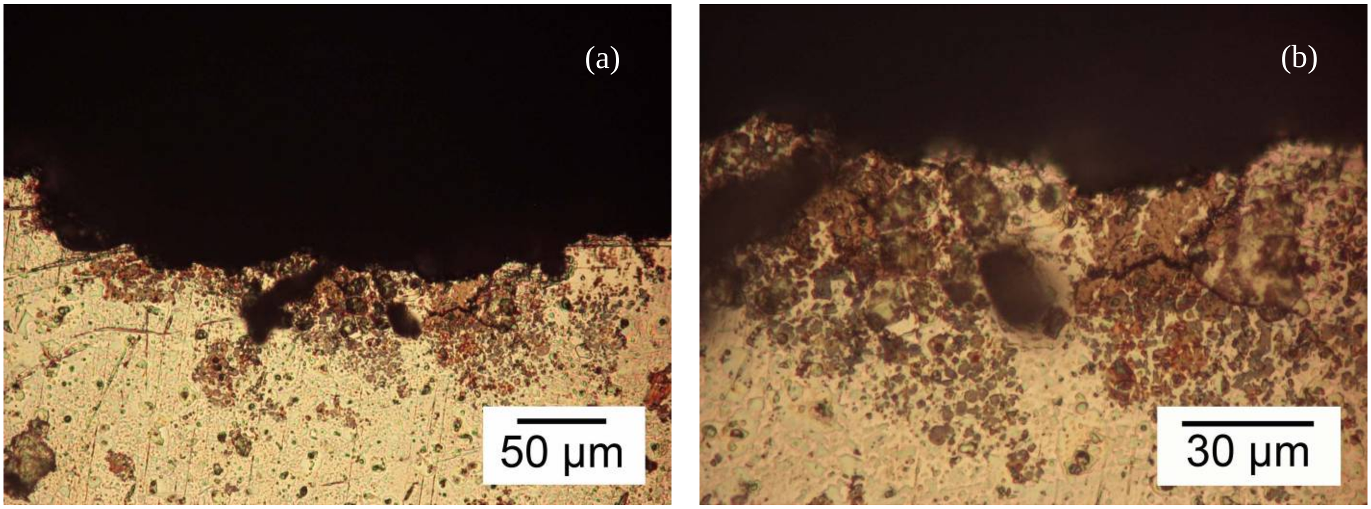

Fig. 4.51 Crack path appearance of FGM with 4 wt.%B, tested at R=0.033.
a) Some defects appear influencing the roughness, b) Particle breaking in a defect-free cluster is evident.

In general the fracture roughness of these series of composites is affected by casting defects as well as by the nature of the reinforcements shape and distribution. While particles clusters could cause crack deflection and consequently retardation of the crack growth; the presence of defects nearly the clusters could cause a low energy failure of the particulate cluster.

4.7.2 SEM Studies of Fractured Surfaces

The fractured surface analysis of gravity cast composites and FGMs are treated separately in this section. It is important to clarify that, the matrix or base material was included in the analysis of gravity cast composites, once that the matrix was processed via gravity casting. Moreover, the images were prepared to show the direction of crack propagation from top to bottom.

SEM of Gravity Casted Composites

To illustrate the fracture surface characteristics of these samples, SEM secondary electron images were organized so as to present fracture morphology of the matrix (0 wt.%B) and composites containing 2 and 4 wt.%B respectively. Then, for each composition the images corresponding to the minimum and maximum fatigue loads, i.e. 1250 N and 1750 N, with R=0.04 and 0.02857 respectively, are presented from Fig. 4.52 to Fig. 4.54.

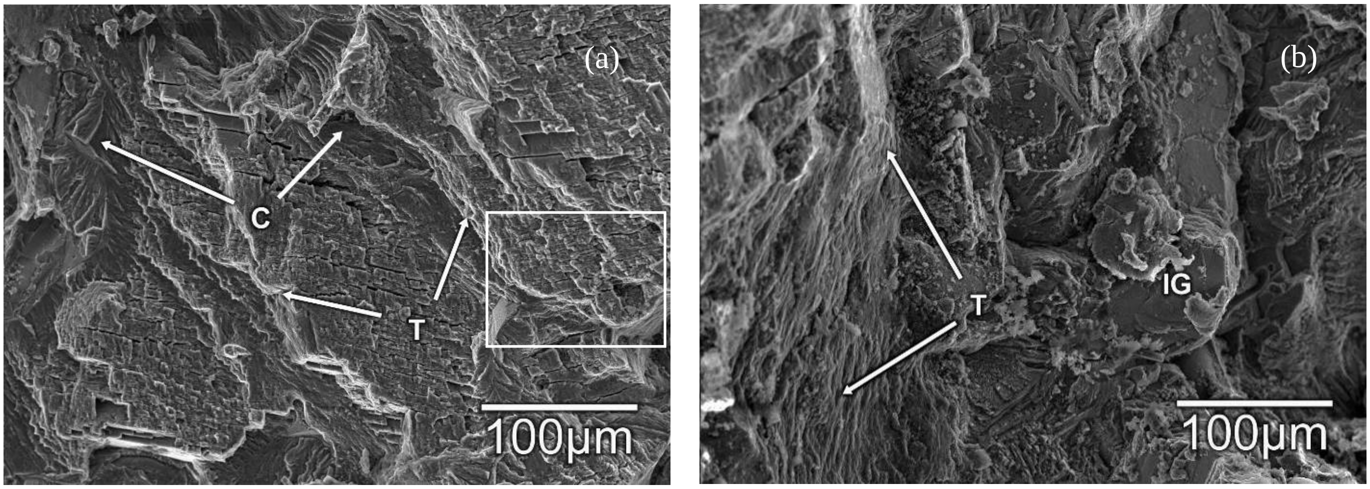

Fig. 4.52 Fracture surface appearance of aluminum matrix
a) Image of sample tested at maximum fatigue load of 1250 N (R=0.04), b) Image of sample tested at 1750 N (R=0.0285)

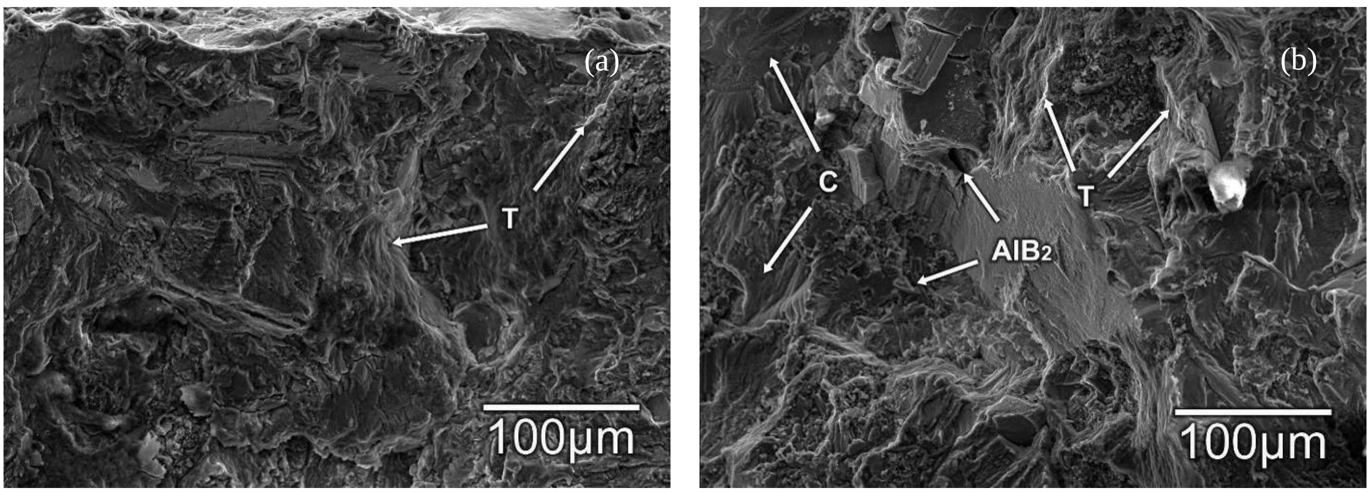

Fig. 4.53 Fracture morphology of composite containing 2 wt.%B
a) Image of sample tested at maximum fatigue load of 1250 N (R=0.04), b) Image of sample tested at 1750 N (R=0.0285)

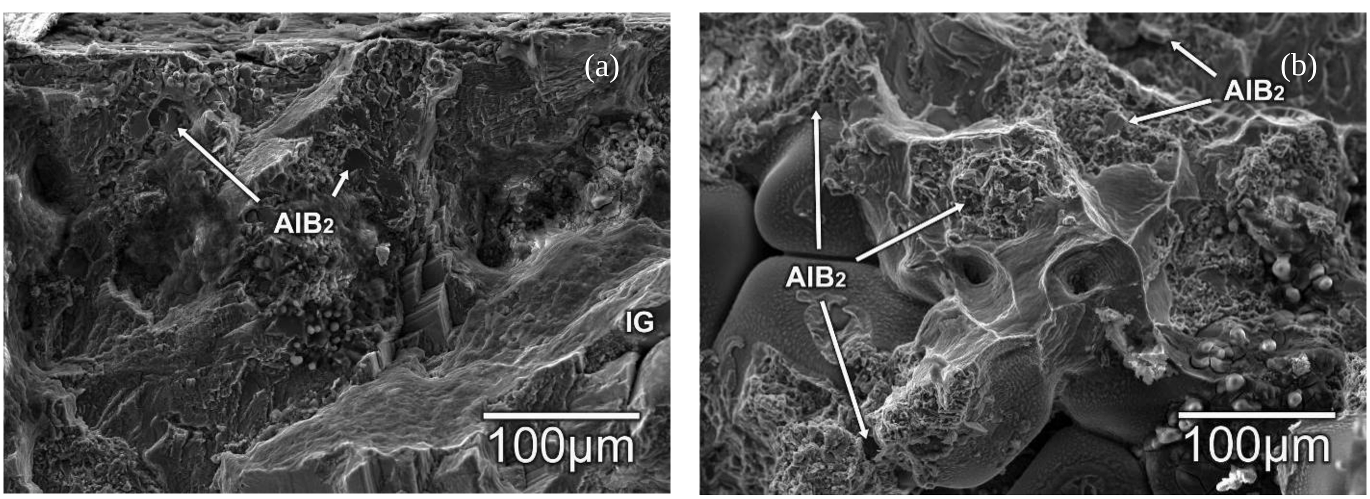

Fig. 4.54 Fracture surface of composite containing 4 wt.%B
a) Image of sample tested at maximum fatigue load of 1250 N (R=0.04), b) Image of sample tested at 1750 N (R=0.0285)

In the matrix, a combination of cleavage (C) and ductile tearing (T) was the characteristic mode of failure observed (Fig. 4.52a). However, some intergranular fracture (IG) could also be detected in the fracture, as illustrated in Fig. 4.52b. In addition, in Fig. 4.52a characteristics 'river patterns' (associated with brittle fracture) can be observed; these are formed when the cleavage fracture is forced to re-initiate at the boundary of a grain in a different orientation (via a step-wise process) [82]. Moreover, some regions in Fig. 4.52a show pronounced secondary cracking, as illustrated in the close up of Fig. 4.55.

It was difficult to indentify differences induced by the test conditions in the fracture of composites containing 2 wt.%B (Fig. 4.53). The fracture was mainly brittle with some small areas of tearing. In addition, in Fig. 4.53b one could identify AlB_2 particles in cleaved regions, which indicates a strong particle-matrix interface. The fracture of the composite with 4 wt.%B of Fig. 4.54 has a similar appearance. Nevertheless, in these samples intergranular fracture was again present, as show in Fig. 4.54b. A close up of a region near the IG fracture permitted detecting particles in the bottom of a cavity produced by tearing of the matrix, as indicated in Fig. 4.56. In addition fatigue striation can be observed in this figure.

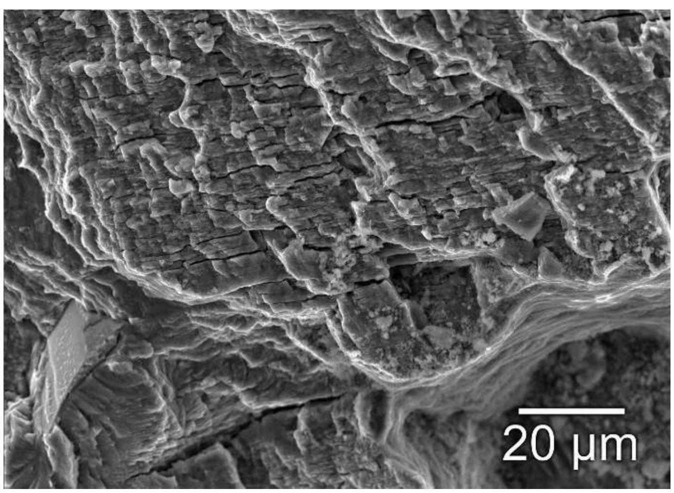

Fig. 4.55 View a higher magnification of area in Fig. 4.52a

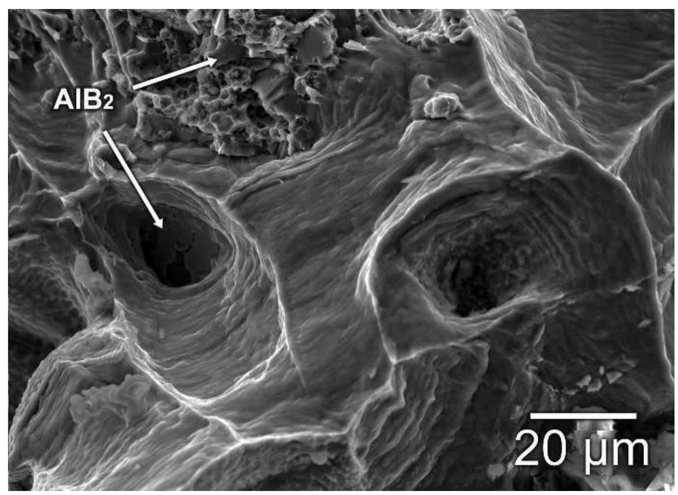

Fig. 4.56 View a higher magnification of area in Fig. 4.54b

Other phase identified in the fracture surface of these composites was θ (or Al_2Cu), which was detected using secondary electron imaging (Fig. 4.57a) of the composite containing 2 wt.%B. This θ phase appears broken in the grain boundaries as result of low energy IG fracture. In addition, backscattered electron images were employed to identify the denser Al_2Cu phase, which appears as bright gray in cleaved regions of Fig. 4.57b.

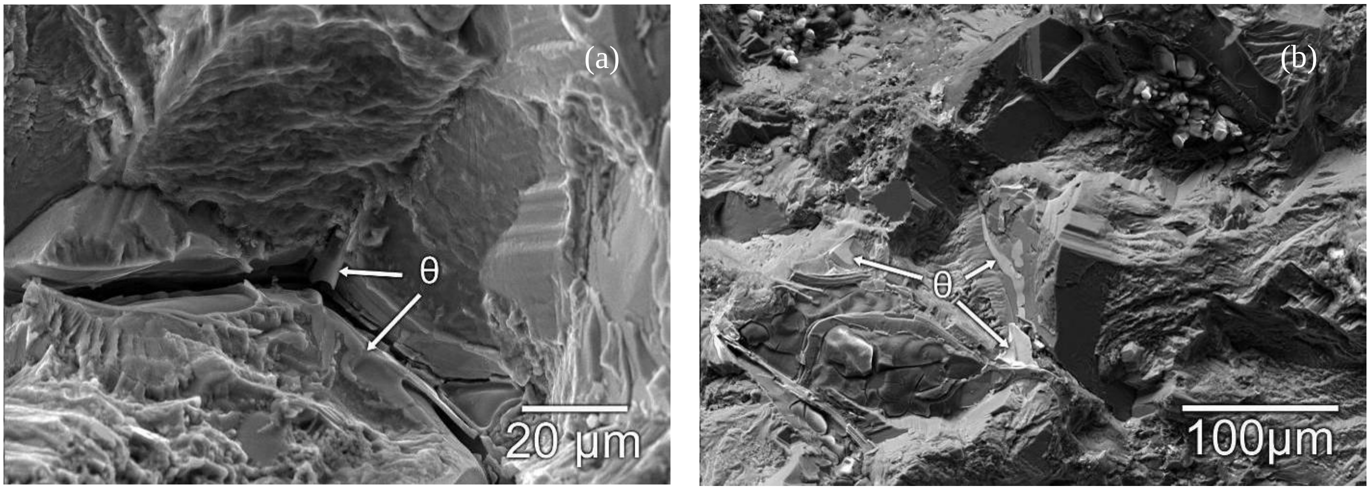

Fig. 4.57 Identification of θ phase in the fracture surface of composites tested at R=0.033
a) Secondary electron image of sample with 2 wt.%B, b) Back-scattered electron image of composite with 4 wt.%B

Moreover, in the 4 wt.%B composite (Fig. 4.58a) one can find failure by debonding of a cluster of AlB_2 particles and finally, evidence of fatigue striations with separation around 0.5 μm was observed at high magnification (Fig. 4.58b) of the rectangle in Fig. 4.58a. In general the mode of failure of the composites fabricated via gravity casting was a combination of brittle and ductile regions, which commonly is defined as quasi-cleavage (QA). However the presence of casting defects and IG fracture can also are observed in some regions of the fracture (i.e. Fig. 4.54b). Thus, these low energy fracture regions could be responsible for the anomalous variations of the crack growth rate (CGR) on the da/dN vs ΔK* curves.

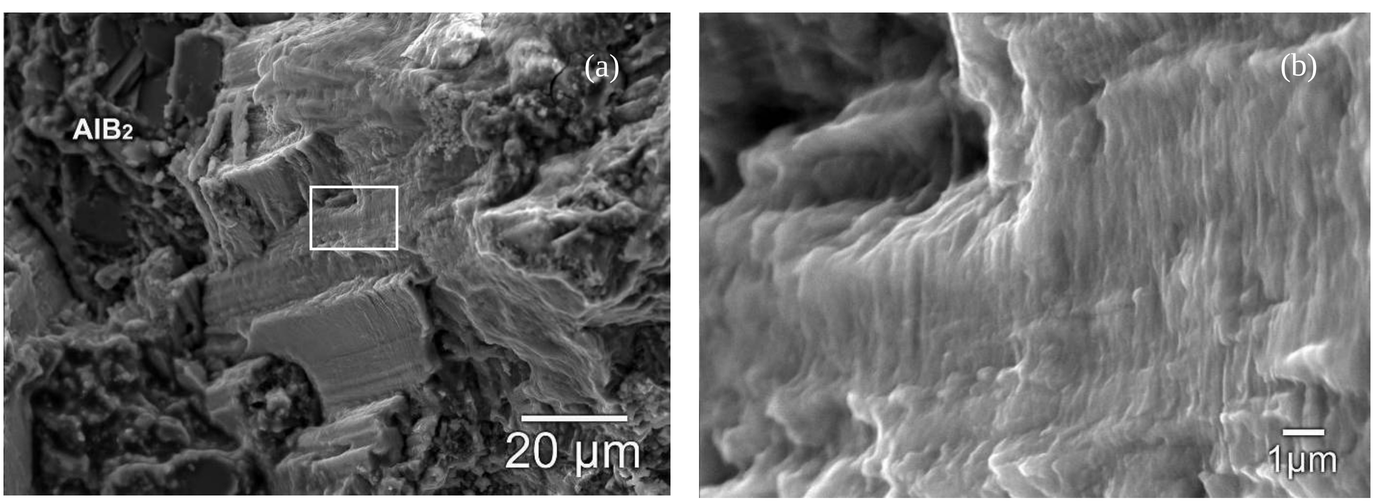

Fig. 4.58 Identification of fatigue striations in the fracture of a composite with 4 wt.%B, tested at R=0.033
a) High magnification image illustrating particles failure, b) Area in the rectangle in *a* show evidence of fatigue striations

SEM Study of FGMs

The secondary electron images of FGMs are organized to show first the fracture surface of samples containing 1 and 3 wt.%B, tested at R=0.033, as illustrated in Fig. 4.59. The fracture morphology of these images is similar. It is predominantly brittle with some areas of ductile tearing. Again, the presence of IG fracture was detected, as indicated in Fig. 4.59b. The presence of AlB_2 dispersoids was also identified in these images. In addition, some large cleavage areas were observed in the samples with 3 wt.%B of Fig. 4.59b.

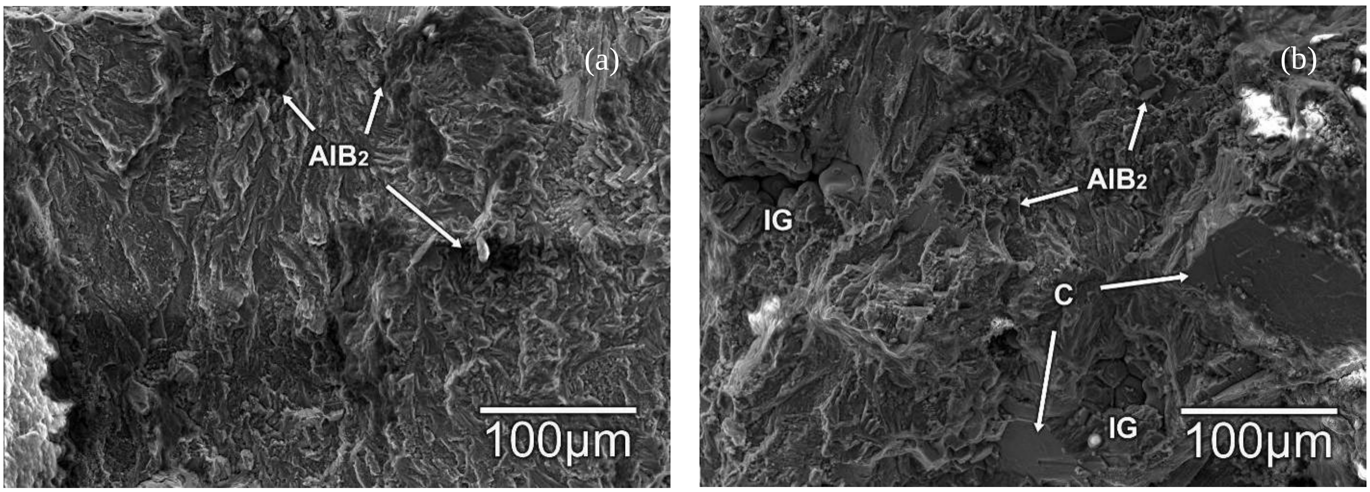

Fig. 4.59 Fracture surface appearance of FGMs tested at R=0.033
a) 1 wt.%B composite sample, b) 3 wt.%B composite sample

As in the study of gravity cast samples, SEM images of FGMs containing 2 and 4 wt.%B are organized to compare the fracture appearance for the two test conditions: maximum fatigue loads of 1250 N and 1750 N, with R=0.04 and 0.02857 respectively. The images in Fig. 4.60 show similar fracture characteristics: a combination of cleavage areas with small regions of ductile tearing. For both images in Fig. 4.60 secondary microcracks are observed. These cracks could be associated with crack subdivision (branching) similar to the observed in Fig. 4.51b.

The centrifugal cast samples containing 4 wt.%B also showed a quasi-cleavage type of fracture, with the presence of some oxides (Fig. 4.61). The particles in these composites exhibited some debonding, as indicated in the high magnification images of Fig. 4.62, corresponding to the rectangular areas in Fig. 4.61a and Fig. 4.61b respectively.

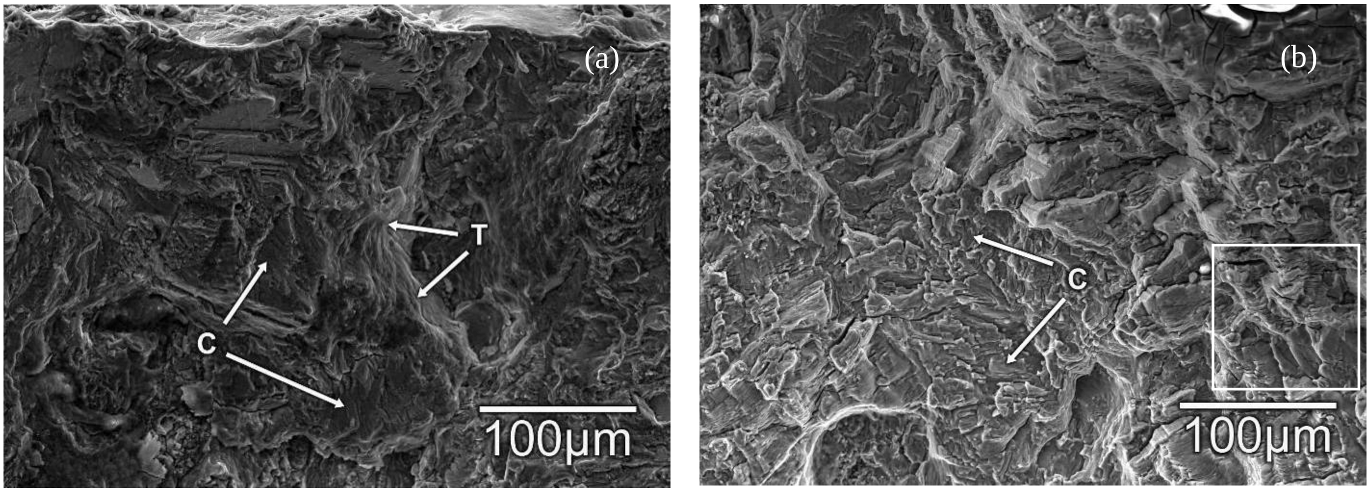

Fig. 4.60 Fracture morphology of FGM containing 2 wt.%B
a) Image of sample tested at maximum fatigue load of 1250 N (R=0.04), b) Image of sample tested at 1750 N (R=0.0285)

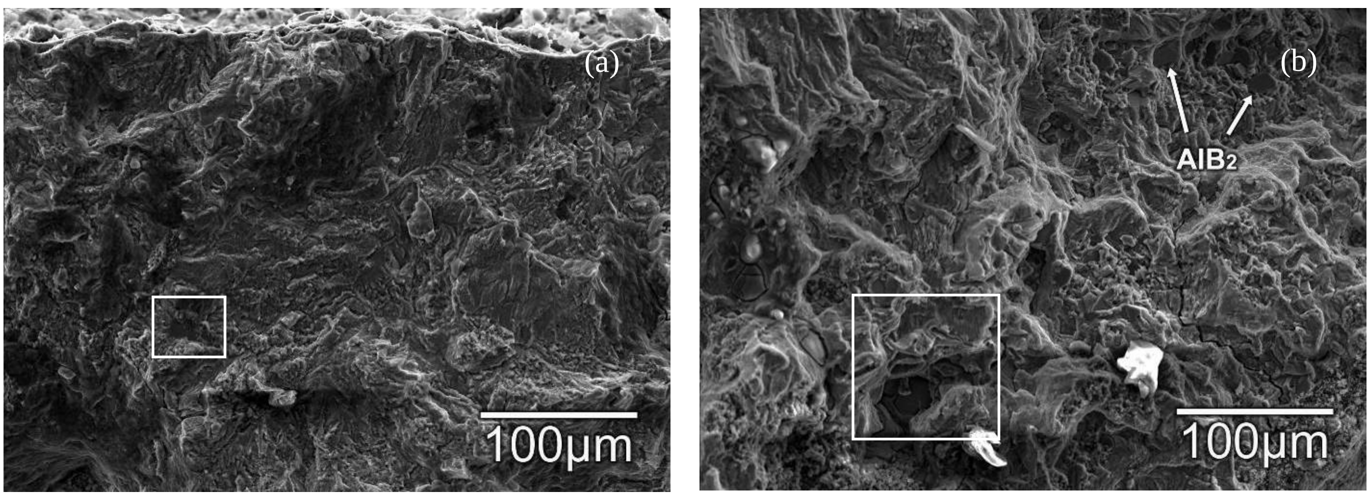

Fig. 4.61 Fracture surface of FGM containing 4 wt.%B
a) Image of sample tested at maximum fatigue load of 1250 N (R=0.04), b) Image of sample tested at 1750 N (R=0.0285)

The images in Fig. 4.62 indicate that independently of the orientation of the particles in the fracture surface, debonding would be one of the principal mechanisms of particle failure. In addition, the presence of particles within the depressions suggests that ductile tearing occur in the matrix nearby the particles before the crack advances. Something similar is also observed in Fig. 4.56, which corresponds to a gravity cast sample.

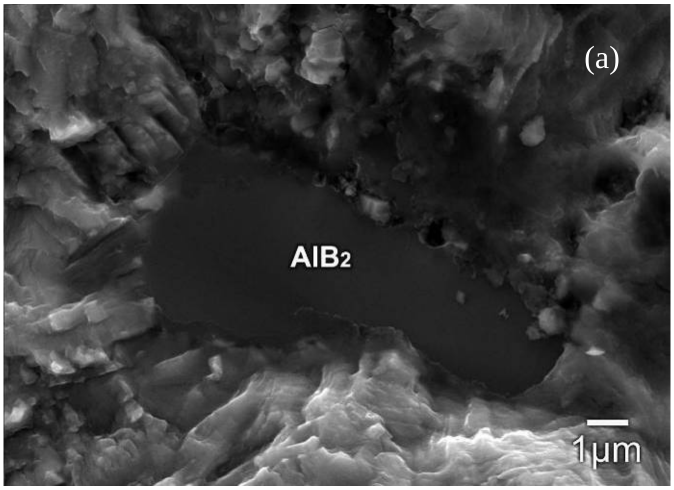

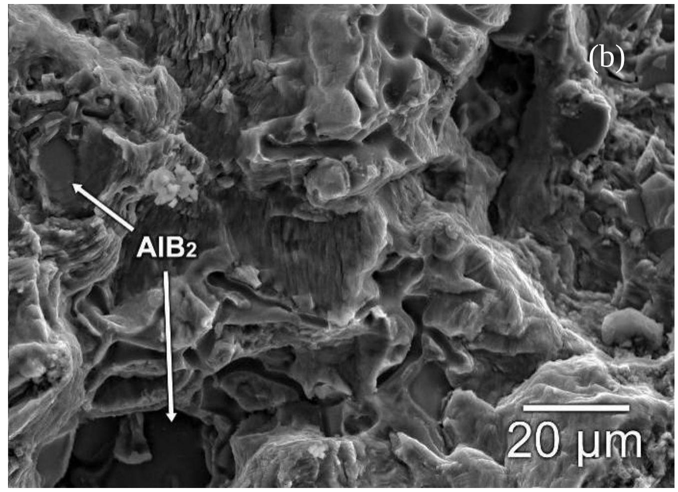

Fig. 4.62 High magnification images of FGMs with 4 wt.%B showing evidence of debonding of particle planes a) Area in the rectangle in Fig. 4.61a show a particle border, b) Area in the rectangle in Fig. 4.61b show particle planes

More evidence of particle debonding is presented in Fig. 4.63, which is a high magnification image of an FGM containing 2 wt.%B. In this figure a particle with the hexagonal planes oriented normal to the fracture surface appears almost separated from the matrix. In addition, the presence of fatigue striations is evident in this image. Moreover, the backscattered electron image in Fig. 4.64 permitted to identify the θ phase embedded in the fracture of the FGM. In this figure, this θ phase can be observed in the matrix and promoting the matrix cracking by traction of the phase, when the precipitated θ appears oriented normal to the surface.

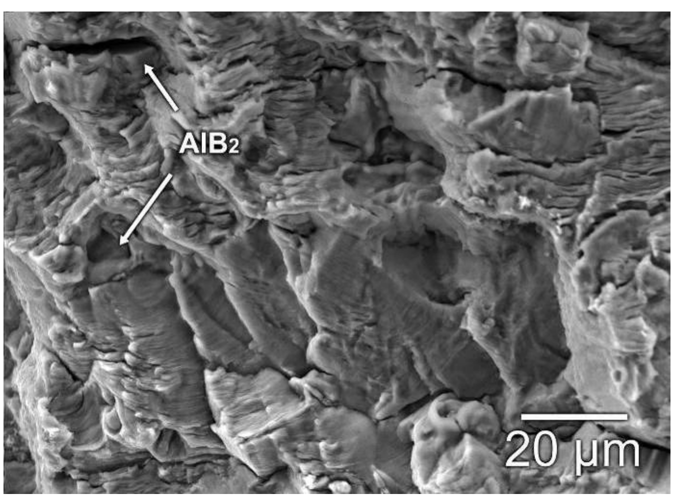

Fig. 4.63 Area in the rectangle in Fig. 4.60b, exhibiting particle debonding and presence of striations

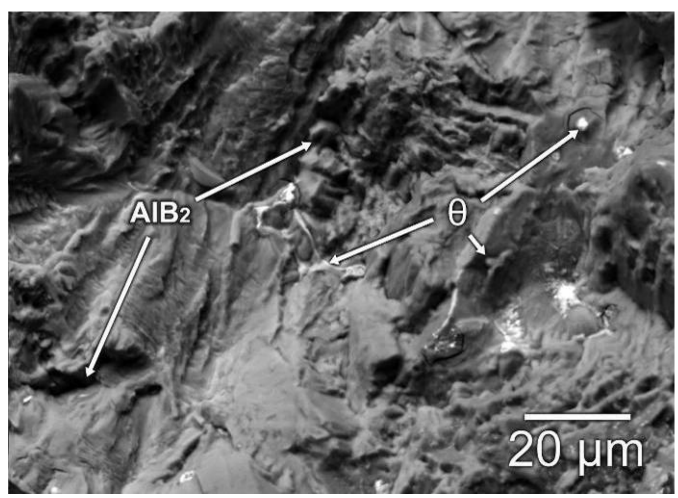

Fig. 4.64 Back-scattered electron image of composite with 3 wt.%B, tested at R=0.033

In the FGM fatigue striations were also detected. By magnifying the rectangular area in Fig. 4.65a one can identify those fatigue striations, as shown in Fig. 4.65b. The striations indicate the local direction of the crack growth, which almost coincides with global crack growth. The crack grew from top to bottom in all images presented in this section. Finally, additional images of FGM with 4 wt.%B (Fig. 4.66) are included to illustrate how the orientation of the hexagonal particle in the fracture has affected the local crack deflection. Thus, the failure of the interface causes higher roughness of the fracture surface

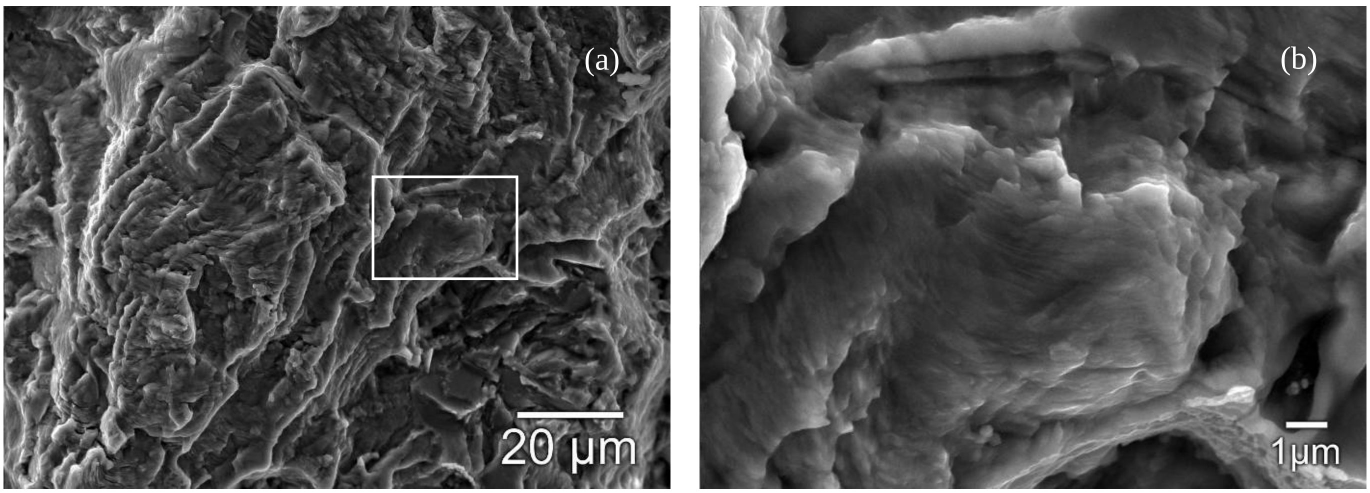

Fig. 4.65 Identification of fatigue striations in the fracture of a FGM with 4 wt.%B, tested at R=0.02857
a) High magnification image, b) Enlarge image showing evidence of fatigue striations

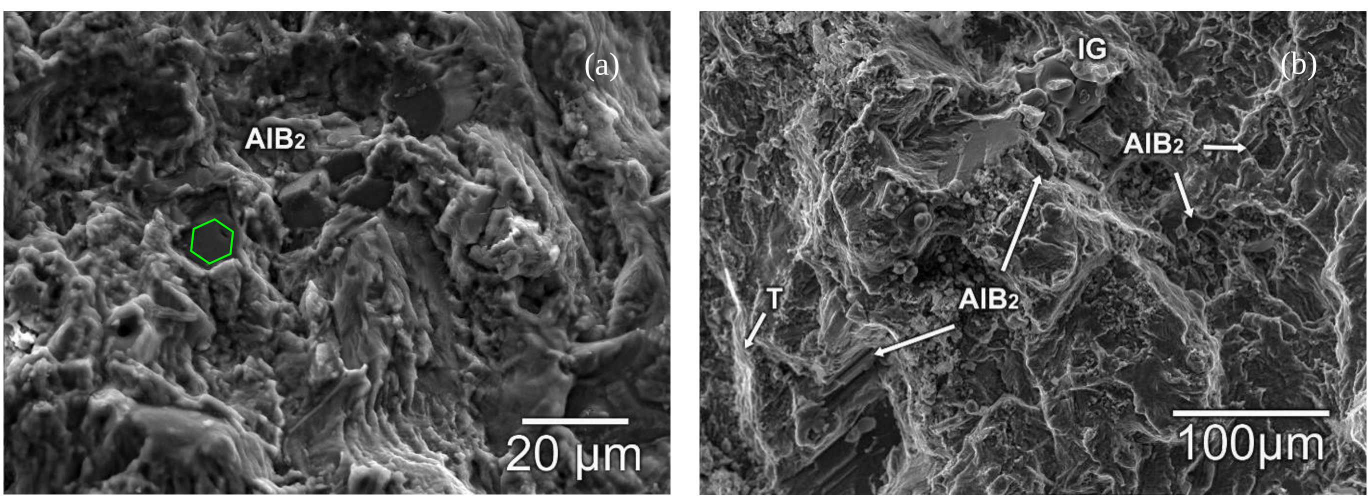

Fig. 4.66 Hexagonal planes of particles in the fracture surface of FGM with 4 wt.%B
a) Tested at maximum load of 1500 N (R=0.033), b) Tested at maximum load of 1750 N (R=0.02857)

4.7.3 Discussion

The study of the crack path allowed revealing features like crack branching, particle cluster separation and particle breaking. The analysis of the fracture surface via SEM permitted distinguishing the fracturing mode and possible failure mechanisms of the material, as well as the influence of the microstructure on the roughness of these composites.

Despite the small differences in the crack growth curve slopes, it was hard to identify any large difference in the fracture morphology between gravity cast samples and the FGM. In both cases, one could observe similar failure patterns (IG fracture, cluster separation, particle breaking, crack branching) and there were no appreciable differences in the mode of failure due to the testing conditions, where the failure mode was defined as a combination of cleavage and tearing regions, also known as quasi-cleavage. However, the roughness of the fracture surface was higher in gravity cast samples than in FGM. According to the microstructure analysis, gravity casting samples showed a higher level of porosity, which do result in more areas sensitive to failure; this leads to an eventual rougher surface.

Using backscattered electron imaging one could identify the θ phase (Al_2Cu) and determine that this phase also affected the crack growth in these composites. However, since deformation of this phase showed to help fracture the matrix (Fig. 4.64) and this phase appears also associated to regions of IG fracture, the effect of this phase on the crack growth behavior of these composites is not clear.

Moreover, although the reduction in the strength of these composites as the level of boron increases was associated to the weakening of the matrix by Mg depletion in the matrix (as a result of the Mg-AlB_2 interaction), the mechanism of the strength reduction is not entirely clear. However, taking into account the characteristics of the particle failure shown in Fig. 4.56, Fig. 4.61, Fig. 4.62 and Fig. 4.63; the key of such strength drop could be attributed to the weakening of the particle-matrix interface. Finally, since the anomalous variations in the CGR in the da/dN vs ΔK curves correspond to an increment and posterior reduction of the CGR, such phenomenon should be associated with the low energy forms of fracture detected, like IG fracture, cluster separation and/or casting defects.

5 CONCLUSIONS

- A systematic methodology was successfully implemented to obtain gradual variation of particle volume fraction along the cross section of the specimens by using a centrifugal casting process. By this procedure it was also possible to obtain complete particle segregation in the specimens, and two sets of parameters were found optimal to reach both types of particle distributions.

- The microstructural analyses revealed that reinforcing particles volume percent in the centrifugally cast varied in a range close to the particle volume percent calculated in gravity casting samples with the same level of boron. While a reduction in the porosity of the material was achieved by using the centrifugally casting process, such reduction was associated to the higher pressure reached by employing a high centrifugal acceleration (48 g).

- The first tests (impact and hardness) performed on the composites obtained via gravity casting were helpful to identify a detrimental interaction between the AlB_2 particles and the Mg present in the matrix. Such interaction occurs at casting temperatures as low as 750°C and is attributed to substitutional diffusion into the AlB_2 phase that deplete Mg atoms from the aluminum matrix.

- The study of the Mg-AlB_2 interaction was carried out by three means. Analyses of EDS, X-ray diffraction and a microhardness-based model to understand the phenomena. The three different approaches permitted estimating the fraction of Mg (X value) in the formula of doped diborides ($Al_{1-X}Mg_XB_2$) as ranging between 0.08 and 0.15, for composites containing only AlB_2 particles, and around 0.32 for AlB_2 particles transforming from AlB_{12}.

- The tensile and flexural strength of composites obtained via centrifugal casting showed to be higher than the strength exhibited by gravity cast samples. This was associated with the defects reduction due to the high acceleration employed during the fabrication process. Moreover, the strength of composite samples obtained by both methods decreases with the amount of particles (volume fraction). This is attributed to Mg-AlB_2 interaction, which reduces the matrix strength around the particles by softening the adjacent matrix.

- The study of fatigue resistance was based in the comparison of the Paris equation exponent calculated for each composition as the slope (m) of the da/dN vs ΔK curve plotted in a log-log scale. This implies that:

$$\log\left(\frac{da}{dN}\right) = m\log(\Delta K) + \log C$$

  This, combined with the utilization of the new crack driving force parameter (ΔK*), proposed by Kujawsky, and the linear fit employing robust statistics, allows the identification of variations in the crack growth behavior due to changes in the material microstructure and testing conditions.

- As a result of the casting defects reduction, centrifugally cast composites showed to have lower slopes (m) than gravity cast composites, which meant a higher crack growth resistance of the FGMs. Consequently, gravity cast samples showed to be more sensitive to monotonic damage at the maximum fatigue loads of the testing conditions.

- In both gravity and centrifugally cast composites the crack growth resistance decreases as the level of boron increases in the range from 1 to 4 wt.%. Linear regression models were obtained for the crack growth curve slope as function of the wt.%B.

- The results from two loading rates show that the gravity cast composites were more susceptible to the loading rate than other samples. These composites exhibited lower crack growth slopes as a result of the higher loading rate. This was explained in terms of the resistance of the material against plastic strains when the strain rate reaches a critical value.

- FGMs exhibited lower fatigue resistance when the crack grew through the CF direction than when the crack grew in the opposite direction. This is understandable, since the crack front is displacing through the particle denser region of the cross section in the CF direction; this causes the crack growth to be affected by the volume fraction of particles and its distribution.

- The crack path is affected by the composite phases as well as some casting defects. As a result, gravity cast composites showed higher roughness, which increased with the level of boron in the composites. In general the fracture mode was a mix of brittle and ductile regions (quasi-cleavage).

- Despite of the differences in the crack growth behavior between gravity and centrifugally cast composites, it was difficult to identify large differences in the fracture morphology of these materials.

- Although the reduction in the strength of these composites as the level of boron increases was associated to the depletion of Mg in the matrix adjacent to the particles (as result of the Mg-AlB_2 interaction) the mechanism of the strength reduction is not clear. Nevertheless, taking into account the characteristics of the particle failure observed, the strength reduction could be attributed to the weakening of the particle-matrix interface.

- In general, it is important to note that, despite the deleterious effect of the interaction Mg-AlB_2, these composites showed higher strength than similar composites without Mg in the matrix. In addition, the studies were performed to as-cast annealed specimens. As a consequence, the strength of these composites can be increased even more by thermomechanical treatments (i.e. aging and cold work), taking advantage of the alloying elements [3, 70, 83].

APPENDIX

X.1 Robust Fit [84, 85]

Since some events detected during fatigue testing can affect the slope of conventional linear regressions in the Paris regime of a da/dN vs ΔK curve, a robust statistical analysis was also implemented. Robust statistics are a helpful tool to obtain linear models even in the presence of a few outliers. The outliers are defined as values that cause unexpected deviations with respect to the majority of sample points and can alter the sample mean $\hat{y}$ if the data value $y_i \rightarrow \pm\infty$. Sample median is barely affected by moving any single value to ±∞. In other words, the median is resistant to gross errors, whereas the mean is not.

The *robustfit* function in MATLAB uses an iteratively reweighted least square algorithm, where the weights for each iteration are calculated by applying a bisquare function to the residuals from the previous iteration. This algorithm gives lower weight to points that do not fit well. The procedure removes the sensitivity to outliers in the data as compared with ordinary least squares regression. Thus, in the weighted least squares regression a scale factor w is included in the fitting process, so the error estimate is minimized.

$$S = \sum_{i=1}^{n} w_i (y_i - \hat{y}_i)^2 \qquad \textbf{(X-1)}$$

Then the parameters estimate b is calculated as:

$$b = (X^T W X)^{-1} X^T W y \qquad \textbf{(X-2)}$$

Then, the standardized adjusted residuals are calculated as:

$$u_i = \frac{r_i}{K \cdot s \cdot \sqrt{1 - h_i}} \qquad \textbf{(X-3)}$$

where, K is a tuning constant equal to 4.685, which give 95% efficiency at the normal, s≈MAD/0.6745 and MAD is the median absolute deviation of the residuals defined as:

$$MAD = median_i \left\{ \left| Y_i - median_j \left(Y_j \right) \right| \right\} \quad \textbf{(X-4)}$$

At the normal

$$MAD = median\left\{ \left| Y - \mu \right| \right\} \approx 0.6745\,\sigma \quad \textbf{(X-5)}$$

Additionally, h_i are the main diagonal of the hat matrix H, also known as leverages, which adjust the residuals by downweighting high-leverage data points. Finally the robust weights are computed using the bisquare function given by

$$w_i = \begin{cases} (1-(u_i)^2)^2 & |u_i| < 1 \\ 0 & |u_i| \geq 1 \end{cases} \quad \textbf{(X-6)}$$

Then the fitting is reached by convergence and the coefficients are obtained. In this case a linear regression is required to obtain the model parameters in the Paris regime. To do this, the data is first fitted using the incremental polynomial method described in the ASTM-E647 [45]; second the asymptotic initial and final parts of the data are avoided, as illustrated in Fig. X.1. Where the red line describes the data adjusted by least squares using a second order polynomial (parabola) to sets of (2n+1) successive data points, with n equal to 3.

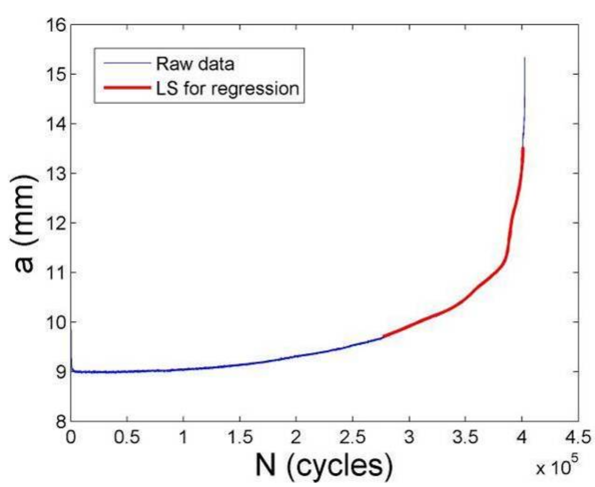

Fig. X.1 Crack length as function of the number of cycles N.

The red line data in Fig. X.1 is used to obtain the da/dN vs ΔK curve plotted in the log-log graphic shown in Fig. X.2. There, some changes in the crack growth (da/dN) are observed, which results in disturbance in the Paris linear behavior. This affects the calculation of the slope via linear regression. However, seeing that these events have been identified to occur due to the microstructural heterogeneity of the sample (reinforcements or casting defects), and do not correspond to the normal behavior of the composite, the use of robust statistics help to reduce such effect on the linear fitting of the log(da/dN) vs log(ΔK), as illustrated in Fig. X.3.

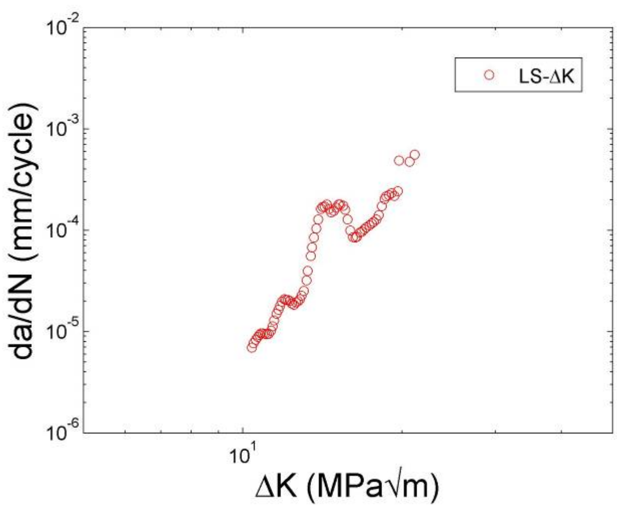

Fig. X.2 Crack growth of centrifugally cast sample (2.5%Cu-1%Mg-1%B) showing anomalous behavior

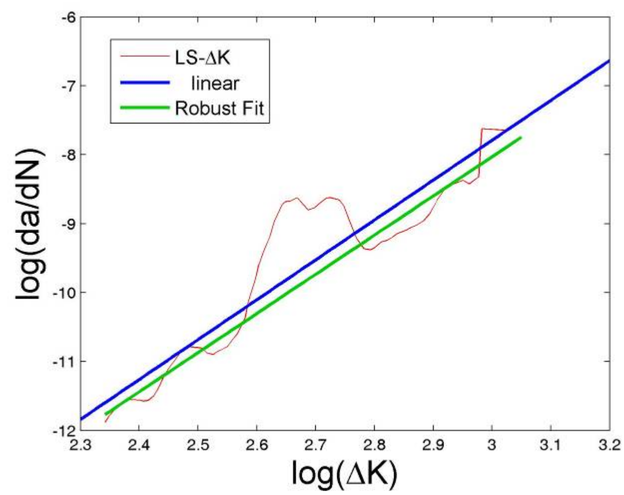

Fig. X.3 Linear regressions of crack growth data showed in Fig. X1

REFERENCES

1. Kevorkijan, V.M., *Aluminum Composites for Automotive Applications: A Global Perspective.* JOM, 1999. **51**(11): p. 54-58.
2. Suárez, O.M., *Mechanical Properties of a Novel Aluminum Matrix Composite Containing Boron.* Journal of the Mechanical Behaviour of Materials, 2001. **12**(4): p. 225-237.
3. Suárez, O.M., J. Yupa-Luna, and H.E. Calderón, *Precipitation Hardening in Novel Cast Aluminum Matrix Composites.* American Foundry Society Trans, 2003: p. 111.
4. Calderón, H.E., *Mechanical Deformation Effects on Heat Treated Aluminum Matrix Composites*, in *Mechanical Engineering*. 2004, University of Puerto Rico: Mayagüez. p. 111.
5. Melgarejo, Z.H., *Fabrication and Characterization of Functionally Graded Al/AlB$_2$ Matrix Composites for High Wear Aerospace Applications Using Centrifugal Casting* in *Mechanical Engineering*. 2006, University of Puerto Rico: Mayagüez.
6. Schutz, W., *A Histry of Fatigue* Engineering Fracture Mechanics, 1996. **54**.
7. Rankine, W.J.M. *On the Causes of the Unexpected Breakage of the Journals of Rail Way Axles, and on the Means of Preventing Such Accidents by Observing the Law of Continuity in their Construction*. in *Minutes of Proccedings*. 1842: Institution of Civil Engineers.
8. Sandor, B.I., *Fundamentals of cyclic stress and strain* University of Wisconsin Press, 1972: p. 167.
9. Weitzmann, R.H. and I. Finnie (1974) *Further Studies of Crack Propagation Using the Controlled Crack Propagation Approach* Fracture Toughness and Stable Cracking, ASTM STP 559, Am. Soc. for Testing and Materials **Volume**, 111-126
10. Dowling, N.E., *Mechanical Behavior of Materials*. 2nd ed. 1998, New Jersey: Prentice Hall.
11. Yu, J., P. Liaw, and M. Huang, *The impact-fatigue fracture of metallic materials.* JOM Journal of the Minerals, Metals and Materials Society, 1999. **51**(4): p. 15-18.
12. Tanaka, T., K.-i. Kinoshita, and H. Nakayama, *Crack opening behavior near crack tip in impact fatigue*. International Journal of Fracture, 1985. **29**(4): p. R39-R44.
13. Jones, N., *Structural Impact*. 1989: Cambridge University Press.
14. Saxena, A., *Nonlinear Fracture Mechanics for Engineers*. 1998, Boca Raton, Fl: CRC PRess.
15. Kobayashi, T., *Strength and Toughness of Materials*. 2004, Tokyo: Springer-Verlag.
16. Newman, J.A., *The Effects of Load Ratio on Threshold Fatigue Crack Growth of Aluminum Alloys*, in *Engineering Mechanics*. 2000, Virginia Polytechnic Institute and State University: Virginia.

17. Sinmazçelik, T., A. Arici, and V. Günay, *Impact fatigue behaviour of unidirectional carbon fibre reinforced polyetherimide (PEI) composites.* Journal of Materials Science, 2006. **41**: p. 6237-6244.
18. Roy, R., et al., *Impact Fatigue Behaviour of Carbon Fibre-Reinforced Vinylester Resin Composites.* Bulletin of Materials Science, 2001. **24**(1): p. 79-86.
19. Ouroua, Y., et al., *Some Insights into the Impact Fatigue Damage Behaviour in Laminated Composites.* WIT Transactions on The Built Environment, 2006. **87**.
20. Cohen, A. and S. Yalvac, *Development and Application of an Impact Fatigue Test.* Composites Engineering, 1993. **3**: p. 31-41.
21. Yang, P. and Y. Liu, *Low-Cycle Impact Fatigue of* SiC_w*/7475Al Composite.* Journal of Materials Engineering and Performance, 1998. **7**(5): p. 667-681.
22. Hancock, J.R. and G.G. Shaw, *The Fatigue and Impact Resistance of Dual-Matrix Boron-Aluminum Composites*. 1974, Midwest Research Inst.: Kansas City MO. p. 14.
23. Sebbani, M.J.E. and C. Allaire, *Mechanical impact fatigue of refractories.* British Ceramic Transactions, 2001. **100**: p. 193-196.
24. Hull, D., *Fractography: Observing, Measuring and interpreting Fracture Surface Topography*. 1999, New York: Cambridge University Press. 384.
25. Bonnet, R. and M. Loubradou, *Crystalline defects in a B.C.T. Al2Cu(θ) single crystal obtained by unidirectional solidification along [001]*. Physica status solidi. A. Applied research, 2002. **194**(1): p. 173-191.
26. Scott, T.G., *Handbook of Aluminum. Physical Metallurgy and Processes*, ed. M. Denkker. Vol. 1. 2003, New York.
27. Hirai, T., *Processing of Ceramics*. Vol. 17B. 1996, New York: Weinheim.
28. Meyers, M.A. and K.K. Chawla, *Mechanical Behavior of Materials*. 1999: Prentice Hall, Inc.
29. ASTM, *E23 2007ae1, Standard Test Methods for Notched Bar Impact Testing of Metallic Materials*. 2007, ASTM International: West Conshohocken, PA.
30. Chawla, N., et al., *Effect of matrix microstructure on the tensile and fatigue behavior of SiC particle-reinforced 2080 Al matrix composites.* Metallurgical and Materials Transactions A: Physical Metallurgy and Materials Science, 2000. **31A**(2): p. 531-540.
31. Chawla, N., et al., *Effect of SiC volume fraction and particle size on the fatigue resistance of a 2080 Al/SiC p composite.* Metallurgical and Materials Transactions A, 1998. **29**(11): p. 2843-2854.
32. Mutoh, Y. and I. Sakamoto, *On the Relation Between* J_{IC} *and Critical Equivalent Stress for High Strength Materilas.* Technical Report of the Technological University of Nagaoka, 1981. **3**: p. 1-7.
33. Vasudevan, A.K. and K. Sadananda, *Fatigue crack growth in metal matrix composites.* Scripta Metallurgica et Materialia, 1993. **28**(7): p. 837-842.
34. Sánchez, M.A., *Comportamiento Mecánico y Fractura de Mezclas de Poliestireno y Microesferas de Vidrio*, in *Ciéncies dels Materials I Enginyeria Metal.lurgica*. 2000, Universitat Politécnica de Catalunya: Barcelona, ES.
35. Milan, M.T. and P. Bowen, *Fatigue Crack Growth Resistance of* SiC_p *Reinforced Al Alloys: Effects of Particle Size, Particle Volume Fraction and Matrix Strength.* Journal of Materials Engineering and Performance, 2004. **13**(5): p. 612-618.

36. Kitaoka, S. and Y. Ono, *The Effect of Second Principal Stress on the Fatigue Propagation of Mode I Surface Crack in Al_2O_3/Al Alloy Composites.* International Journal of Fatigue, 2003. **25**(12): p. 1347-1355.
37. Lados, D.A., D. Apelian, and A.M. de Figueredo. *Fatigue Performance of High Integrity Cast Aluminum Components*. in *2nd International Aluminum Casting Technology Symposium*. 2002. Columbus, OH: ASM International.
38. Chen, Z., P. He, and L. Chen, *The Role of Particles in Fatigue Crack Propagation of Aluminum Matrix Composites and Casting Aluminum Alloys.* Journal of Materials Science and Technology, 2007. **23**(2): p. 213-216.
39. Xu, F.M., et al., *Comparison of the fatigue crack growth behavior of graded and homogeneous SiC particulate reinforced Al composite.* Journal of Materials Science Letters, 2003. **22**(12): p. 899-901.
40. Lados, D.A., *Fatigue Crack Growth Mechanism in Al-Si-Mg Alloys*, in *Materials Science and Engineering*. 2004, WPI: Worcester, MA. p. 179.
41. ASTM, *E399-08, Standard Test Method for Plane-Strain Fracture Toughness of Metallic Materials*. 2008, ASTM International: West Conshohocken, PA.
42. ASTM, *E1820 - 08a, Standard Test Method for Measurement of Fracture Toughness*. 2008, ASTM International: West Conshohocken, PA.
43. National Academy of Sciences (U.S.). Space Science Board. Man in Space Committe, B.A.F.B., *Impact Acceleration Stress*. 1962: National Academy of Sciences-National Research Council. 504.
44. Chehab, A.G. and M.H. El Naggar, *Response of block foundations to impact loads.* Journal of Sound and Vibration, 2004. **276**(1-2): p. 293-310.
45. ASTM, *E647-08, Standard Test Method for Meaurement of Fatigue Crack Growth Rates*. 2008, ASTM International: West Conshohocken, PA.
46. Paris, P., M.P. Gomez, and W.E. Anderson, *A Rational Analytic Theory of Fatigue.* The Trend in Engineering, 1961. **13**: p. 9-14.
47. Paris, P. and F. Erdogan, *A Crictical Anlysis of Crack Propagation Laws.* Journal of Basic Engineering, Transactions of the American Society of Mechanical Engineers, 1963: p. 528-534.
48. Kujawski, D., *A new ([Delta]K+Kmax)0.5 driving force parameter for crack growth in aluminum alloys.* International Journal of Fatigue, 2001. **23**(8): p. 733-740.
49. Elber, W., *The Significance of Fatigue Crack Closure*, in *Damage Tolerance in Aircraft Structures, ASTM STP 486*. 1971, American Society for Testing and Materials: Philadelphia, PA. p. 230-42.
50. Donald, J.K., *Introducing the compliance ratio concept for determining effective stress intensity.* International Journal of Fatigue, 1997. **19**(93): p. 191-195.
51. Donald, K. and P.C. Paris, *An Evaluation of ΔK_{eff} Estimation Procedures on 6060-T6 and 2024-T3 Aluminum Alloys.* International Journal of Fatigue, 1999. **21**(Supplement 1): p. 47-57.
52. Paris, P.C., H. Tada, and J.K. Donald, *Service load fatigue damage -- a historical perspective.* International Journal of Fatigue, 1999. **21**(Supplement 1): p. 35-46.
53. Walker, K., *The effect of stress ratio during crack propagation and fatigue for 2024-T3 and 7075-T6 aluminum*, in *Effects of Enviroment and Complex Loading History on Fatigue, ASTM STP 462*. 1970, American Society for Testing and Materials: Philadelphia, PA. p. 1-14.

54. Forman, R.G., V.E. Kearney, and R.M. Engle, *Numerical Analysis of Crack. Propagation in a Cyclic-Loaded Structure.* Journal Basic Engineering, ASME, 1967. **89**(Series D): p. 459-464.
55. Singh, N., R. Khelawan, and G.N. Mathur, *Effect of Stress Ratio and Frequency on Fatigue Crack Growth Rate of 2618 Aluminum Alloy Silicon Carbide Metal Matrix Composite.* Bulletin of Materials Science, 2001. **24**(2): p. 169-171.
56. Couper, M.J., A.E. Neeson, and J.R. Griffiths, *Casting defects and the fatigue behaviour of an aluminium casting alloy.* Fatigue and Fracture of Engineering Materials and Structures, 1990. **13**(3): p. 213-227.
57. Wang, Q.G., D. Apelian, and D.A. Lados, *Fatigue behavior of A356-T6 aluminum cast alloys. Part I. Effect of casting defects.* Journal of Light Metals, 2001. **1**(1): p. 73-84.
58. Murakami, Y., M. Takada, and T. Toriyama, *Super-long life tension-compression fatigue properties of quenched and tempered 0.46% carbon steel.* International Journal of Fatigue, 1998. **20**(9): p. 661-667.
59. Wong-Ng, W., et al., *Powder Diffraction File, NBS (USA).* ICDD Grant-in-Aid, 1988. **3**(2): p. 113.
60. Rai, A., et al., *Importance of Phase Change of Aluminum in Oxidation of Aluminum.* Journal of Physical Chemistry, 2004. **B**(108): p. 14793-95.
61. Guesnier, A.W.a.A., *Metallographic Preparation of Aluminum and Aluminum Alloys,* in *Struers Application Notes,* Struers, Editor. 2008.
62. ASTM, *D3552-96(2007), Standard Test Method for Tensile Properties of Fiber Reinforced Metal Matrix Composites*. 2007, ASTM International: West Conshohocken, PA.
63. ASTM, *E8/E8M-08, Standard Test Method for Tension Testing of Metalic Materials*. 2008, ASTM International: West Conshohocken, PA.
64. Quispitupa, A., *Fatigue Behavior of Ultra High Strength Structural Materials,* in *Civil Engineering* 2004, University of Puerto Rico: Mayagüez. p. 135.
65. Aniban, N., R.M. Pillai, and B.C. Pai, *An analysis of impeller parameters for aluminium metal matrix composites synthesis.* Materials & Design, 2002. **23**(6): p. 553-556.
66. Olaya-Luengas, L., *Characterization of Squeeze-Cast AlB_{12}/Al and AlB_2/Al Composites*, in *Mechanical Engineering*. 2009, University of Puerto Rico: Mayagüez. p. 87.
67. Panda, E., D. Mazumdar, and S.P. Mehrotra, *Mathematical Model of Particle Segregation During Centrifugal Casting of Metal Matrix Composites.* Metallurgical and Materials Transactions A, 2006. **37A**(5): p. 1675-1687.
68. Calderón, H.E., et al., *Effect of AlB2 – Mg Interaction on the Mechanical Properties of Al-Based Composites*. 2009, University of Puerto Rico: Mayaguez, PR. p. 13.
69. Milan, M.T. and P. Bowen, *Tensile and fracture toughness properties of SiCp reinforced Al alloys: Effects of particle size, particle volume fraction, and matrix strength.* Journal of Materials Engineering and Performance, 2004. **13**(6): p. 775-783.
70. Calderon, H.E., O.M. Suarez, and E. Barrios, *Thermomechanical Effects on Aluminum Matrix Composites Reinforced with AlB2 Particles.* Journal of Composite Materials, 2008. **42**(25): p. 2651-2672.
71. Adelakin, T.K., *An Experimental Study of Aluminum Boride Particles Distribution in Centrifugal Cast Al/AlB_x Composites*, in *Mechanical Engineering*. 2009, University of Puerto Rico: Mayagüez. p. 102.

72. Mudgel, M., et al., *Aluminium substitution induced superstructures in Mg1-xAlxB2 (x = 0.0 to 0.50): An X-ray diffraction study.* Physica C: Superconductivity, 2007. **467**(1-2): p. 31-37.
73. Margadonna, S., et al., *Crystal structure of the Mg1-xAlxB2 superconductors near x ~ 0.5.* Physical Review B, 2002. **66**(1): p. 014518.
74. Lubarda, V.A., *On the effective lattice parameter of binary alloys.* Mechanics of Materials. **35**(1-2): p. 53-68.
75. PDF#00-038-1369, *Powder Diffraction File.* JCPDS, 1988. **Set 38**: p. 509.
76. Zupanič, F., *Composition and Morphology of Diborides in Al-Ti-B Alloys after Anneling at 1873K.* RMZ - Materials and Geoenvironment, 2008. **55**(1): p. 7-18.
77. Lu, L., C.Y.H. Lim, and W.M. Yeong, *Effect of reinforcements on strength of Mg9%Al composites.* Composite Structures. **66**(1-4): p. 41-45.
78. Deppisch, C., et al., *Processing and mechanical properties of AlB2 flake reinforced Al-alloy composites.* Materials Science and Engineering A, 1997. **225**(1-2): p. 153-161.
79. Kujawski, D., *[Delta]Keff parameter under re-examination.* International Journal of Fatigue. **25**(9-11): p. 793-800.
80. Stoychev, S. and D. Kujawski, *Analysis of crack propagation using [Delta]K and Kmax.* International Journal of Fatigue. **27**(10-12): p. 1425-1431.
81. Buršák, M. and I. Mamuzić, *The Influence of the Loading Rate on the Mechanical Properties of Drawing Steel Sheet.* Metalurgija, 2006. **45**(1): p. 57-60.
82. James, M.N. *Examples of Aluminum Fractography*. 2009 [cited; Available from: http://www.tech.plym.ac.uk/sme/Interactive_Resources/tutorials/FailureAnalysis/Fractography/Fractography_Aluminium.ppt.
83. Suárez, O.M., *Precipitation hardening of a novel aluminum matrix composite.* Materials Characterization, 2002. **49**(2): p. 187-191.
84. Ripley, B.D., *Robust Statistics - how not to reject outliers. I. Basic Concepts.* Analyst, 1989. **114**: p. 1693-1697.
85. Ripley, B.D., *Robust Statistics II. Inter-laboratory trials.* Analyst, 1989. **114**: p. 1699-1702.